D^0-electron correlations in p–Pb collisions at $\sqrt{s_{NN}}$ = 5.02 TeV

Per-Ivar Lønne

Thesis for the degree of philosophiae doctor (PhD)

at the University of Bergen

2017

Date of defence: 21st of April, 2017

Year: 2017
Title: D^0-electron correlations in p–Pb collisions at $\sqrt{s_{\mathrm{NN}}} = 5.02\,\mathrm{TeV}$
Author: Per-Ivar Lønne
Print: AiT Bjerch AS / University of Bergen
ISBN: 978-82-308-3077-2

Abstract

In collisions of lead nuclei at the Large Hadron Collider (LHC) at CERN, a state of matter called Quark-Gluon Plasma (QGP) is formed, where quarks and gluons are no longer confined into hadrons. Heavy-flavour quarks, i.e., charm and beauty, are effective probes for studying the QGP, as their relatively large mass limits their production predominantly, if not exclusively, to hard scattering processes in the very first moments of the collisions, before the QGP formation. As the quarks propagate through the hot and dense medium created in the Pb–Pb collisions they interact with the medium and lose energy via elastic collisions and gluon radiation. The study of the modification of angular correlations between D mesons and electrons from heavy-flavour hadron decays in Pb–Pb collisions with respect to pp and p–Pb collisions can provide relevant information on the energy-loss mechanism. This applies in particular to the dependence of the correlation on the path length traversed by the charm quark in the medium, and to possible medium modifications of charm-quark fragmentation and hadronisation. In pp collisions, these measurements can be sensitive to the different production processes of heavy-flavour quarks, e.g., pair production vs. gluon splitting, and measurements in p–Pb collisions yields information on Cold Nuclear Matter (CNM) effects related to the structure of the initial state of the particle collisions, e.g., the additional effects caused by introducing a lead nucleus in p–Pb collisions compared to pp collisions.

In this thesis, the measurement of azimuthal correlations of D mesons and electrons from heavy-flavour hadron decays in p–Pb collisions at $\sqrt{s_{\mathrm{NN}}} = 5.02\,\mathrm{TeV}$ will be presented, in the $\mathrm{D}^0 \rightarrow \mathrm{K}^-\pi^+$ decay channel. The analysed data originate from collisions of protons with lead ions, facilitated by the LHC at CERN in the beginning of 2013, recorded by the ALICE experiment, a dedicated heavy-ion detector focusing on studies of the QGP. A compatibility within the statistical uncertainties was found while comparing correlation distributions in the pp and p–Pb collision systems, though indications of a discrepancy in the shape of the away side peak between the

two cases was observed, where the peak in p–Pb appears less pronounced. The statistical challenges of the limited data sample available in the p–Pb collisions result in large statistical uncertainties and fluctuations in the correlation distributions. A detailed study of the heavy-flavour electron (HFE) sample was performed in order to optimize the selection efficiency and HFE purity, leading to excellent utilization of the available data.

The presented results provide an important step on the path to studies of D^0-e correlations in Pb–Pb collisions, and displays great potential to further the understanding of the interactions of heavy quarks traversing the hot and dense medium created in ultra-relativistic heavy ion collisions.

As a concluding remark, the performance expected after the upgrade of the ALICE detector during the long shutdown in 2018 will be shown.

Acknowledgements

After several years of study at the University of Bergen, I have arrived at the end of my PhD. I have thoroughly enjoyed my time as a student, and I appreciate all the great people I have had the pleasure of getting to know during this journey.

I would first like to thank my main supervisor, Dieter Röhrich, for the support, advice and guidance during my years as a student, and for giving me the opportunity to take part in a very interesting field of physics. I would also like to thank my co-supervisor, Sedat Altınpınar, whose excellent knowledge in heavy-ion physics has been immensely helpful, and for providing advice and answers to everything from the most basic questions to more complex issues which I have encountered during my PhD. Thanks to my second co-supervisor, Joakim Nystrand, for the many inputs and suggestions you have provided.

I want to thank the heavy-flavour physics working group and the HFCJ analysis group at ALICE, in particular Andrea Rossi, Fabio F. Colamaria and Elena Bruna, for the valuable contributions to my work. I appreciate the interesting discussions and suggestions which helped driving the analysis forward.

I want to thank Hege A. Erdal and Matthias Richter, who have both played important roles in the development of the analysis. It has been a pleasure to work with both of you, and I have learned a lot from our collaboration. I would also like to thank Ionut Arsene for all the help and advice you have provided through our frequent meetings and discussions.

I want to thank Boris Wagner. I have enjoyed sharing an office with you for these past few years, and our many conversations covering a magnitude of topics. I have benefited greatly from your knowledge of computing. I spent the first half year of the work on my analysis at GSI, and would like to thank my office mate, Alexander P. Kalweit, for your friendliness and for sharing your knowledge of particle identification at ALICE.

Thank you, Kristian S. Ytre-Hauge, for your constructive comments when helping me proofread my thesis.

I finally want to thank my family. Your support and encouragement means a lot to me. A great thank you goes to my beloved girlfriend, Marte Ulltang, for your patience, support, kindness and motivation.

Per-Ivar Lønne

Bergen, January 2017

Contents

List of Figures

List of Tables

Chapter 1

Introduction

The story so far:
In the beginning the Universe
was created.
This has made a lot of people
very angry and been widely
regarded as a bad move.

The Restaurant at the
End of the Universe.
- Douglas Adams

Introduction

Some of the most fundamental questions asked by mankind are related to how the Universe came to be, what it consists of and how it can be explained down to the very basic properties, preferably by surprisingly simple equations. Answering such questions is a complicated task, but gradually understanding more of the nature around us and becoming more aware of patterns and processes that repeat themselves, and attempting to explain these, gave rise to the early scientific methods. More detailed theories of various processes have been developed, found to be inaccurate and tuned to agree better with more precise observations and improved experimental setups, leading us to understand more about how the Universe is built up. In attempts to understand the basic building blocks of nature, several ancient societies developed

theories of indivisible particles, such as the atom in Greek philosophy in the 5th century BCE. This approach, though heavily refined since the ancient times, is still relevant today. The term "atom" was again used in the beginning of the 19th century by John Dalton [1] to describe extremely small particles which he believed could not be subdivided, but could be combined in chemical reactions to form what was later called molecules. In the following two centuries the atom has been found to consist of a bound state of a positively charged nucleus and negatively charged electrons. The nucleus itself has been divided into protons and neutrons, which in turn can be split into quarks. With the development of particle collider experiments a large variety of subatomic particles have been discovered, and the interactions between them studied. The quest to understand nature has brought science gradually closer to understanding the very first moments of the Universe, in the extreme conditions of the Big Bang nearly 14 billion years ago. At CERN, using the Large Hadron Collider (LHC), heavy ions are collided at 5.02 TeV per nucleon-nucleon pair[1] in A Large Ion Collider Experiment (ALICE), allowing us to create and study a Quark-Gluon Plasma (QGP) at temperatures 100,000 times hotter than in the core of the sun. Studying this state of matter, which constituted the Universe about 1 microsecond after the Big Bang, takes us one step closer to understanding the very beginning of the Universe. In this thesis a method for obtaining more information about the QGP is discussed.

In this chapter the Standard Model of physics will be discussed briefly, with emphasis on the theory of Quantum Chromo Dynamics (QCD), which describes the strong interaction and predicts the QGP and thus provides a theoretical basis for this thesis. Further, the expectations of the QGP behavior will be mentioned, before concluding with a selection of relevant physical observables and recent results from the study of these.

1.1 The Standard Model

Along with the decomposition of the molecules into atoms, nuclei and nucleons, theories were developed to describe how these constituents were held together into larger systems, and to describe their behavior and interactions. Our current understanding of these theories, including the weak force, the electromagnetic force and the strong force, is well described by the Standard Model of particle physics. The Standard

[1] The design value is 5.5 TeV.

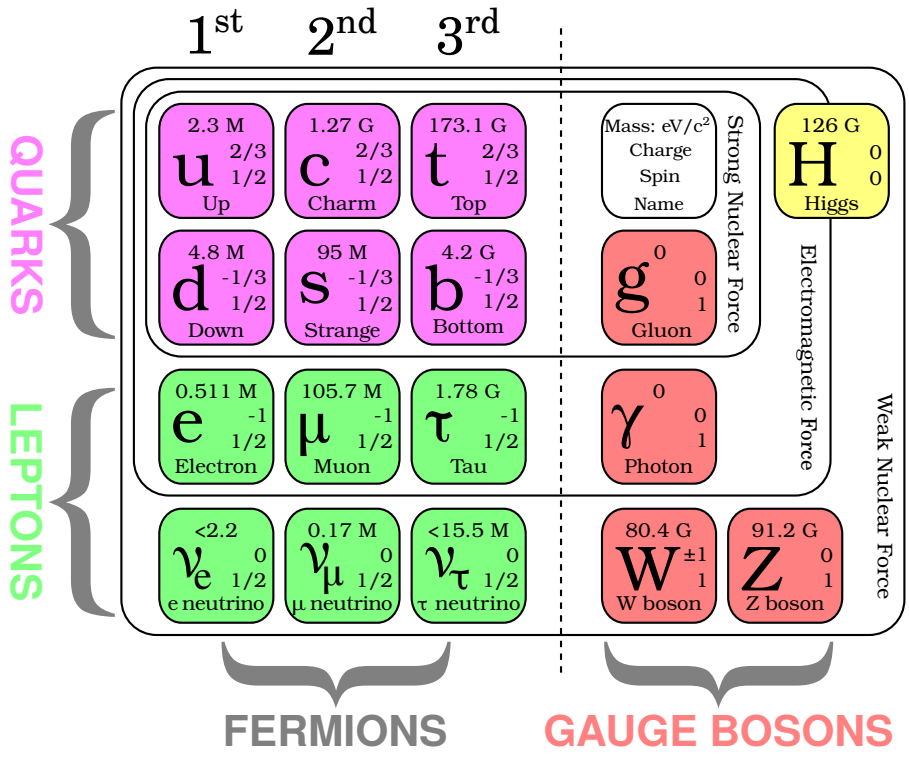

Figure 1.1: A summary of the Standard Model of Particle Physics, displaying the fermions (spin 1/2) to the left, and the bosons to the right. The bosons are divided into the gauge bosons (spin 1) and the Higgs boson (spin 0). The fermions are divided into quarks and leptons, and are sorted by their generations in columns. The quarks are also sorted by their charge in rows. The particles are associated to the forces responsible for their interactions. Figure modified from [2].

Model considers 6 types (flavours) of quarks, as listed with their mass and fractional electrical charge in Figure 1.1. The up (u), down (d) and strange (s) quarks were introduced in 1964 [3, 4], followed by the prediction of the charm (c) quark later the same year [5], and finally the bottom (b) and top (t) were suggested in 1973 [6][2]. These six quarks along with their antiquarks can be combined to build up all known hadrons. The hadrons are grouped into two categories; baryons consisting of three quarks, e.g., protons (uud) and neutrons (udd), and mesons consisting of a quark and an antiquark, e.g., the D^0 ($c\bar{u}$), kaon, K^-($s\bar{u}$), and pion, π^+ ($u\bar{d}$).

The Standard Model describes three of the four fundamental forces, omitting grav-

[2] The names top and bottom was first coined two years after they had been suggested, in 1975 [7].

ity, and can be summarized in a simplified manner by Figure 1.1. While gravity and the electromagnetic force have infinite ranges, and are thus more directly observable in our daily lives, the weak and strong nuclear force have very short ranges, and instead play important roles in the atomic and subatomic domains. The weak force is responsible for radioactive decays and transmutations from one quark flavour to another. The electromagnetic interaction is described theoretically by Quantum Electro Dynamics (QED). The strong force confines quarks into hadrons, and holds the nucleons, i.e., protons and neutrons, together in the nucleus. The strong interaction is described by Quantum Chromo Dynamics (QCD), a theory which also predicts the QGP we are interested in learning more about.

1.1.1 Quantum Chromodynamics

QCD is a relativistic gauge field theory describing the strong interaction, more specifically it is the SU(3) component of the unitary product group SU(3)xSU(2)xU(1) of the Standard Model. A defining feature of QCD is the introduction of colour (chromo) charge carried by the partons, i.e., the quarks and gluons, analogous to the electric charge of QED. Electric charge is either positive or negative, whereas colour charge appears in three varieties; red, green and blue, in addition to their anticharges. Combining all three colour states, or a colour with its anti-colour, results in a colour neutral charge. Quarks carry a single colour charge[3], and combine into colour neutral baryons, i.e., hadrons consisting of three quarks carrying equal amounts of the 3 different colour charges, or mesons consisting of a quark and antiquark carrying charge and anticharge of the same colour. The gluon can be considered bi-coloured, as it carries a charge and an anticharge of different colours, resulting in a non colour neutral state. The colour charge of the gluons allows them to connect to other colour charged objects, and the difference in colour between their charge and anticharge makes the interaction colour independent. The gluons are thus able to self-interact, a property closely related to the anti-screening of the colour charges in the vacuum, where the virtual quark-gluon cloud around a colour charge causes an increase of the effective charge as the distance increases, giving rise to the effect known as asymptotic freedom [8], introduced as a theory independently by David Gross and Frank Wilczek [9] and David Politzer [10] in 1973, for which they were awarded the Nobel Prize in Physics in 2004. The potential between a heavy quark and antiquark can be described

[3] Antiquarks carry colour anticharge.

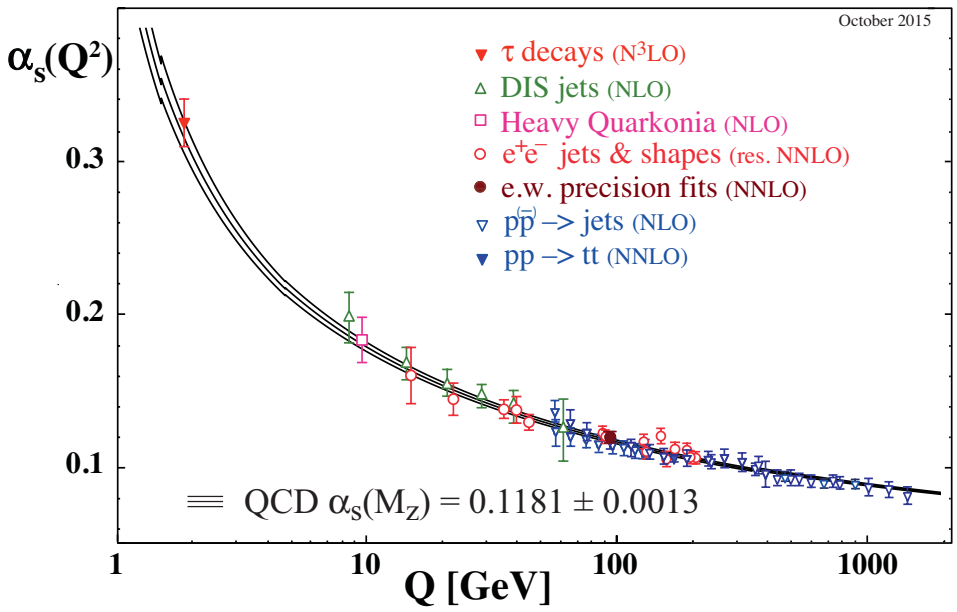

Figure 1.2: Summary of measurements of α_S as a function of the energy scale Q. The respective degree of QCD perturbation theory used in the extraction of α_S is indicated in brackets (NLO: next-to-leading order; NNLO: next-to-next-to leading order; res. NNLO: NNLO matched with resummed next-to-leading logs; N^{3}LO: next-to-NNLO). Figure and caption from [11].

phenomenologically in the form of the Cornell potential [12],

$$V = -\frac{4}{3}\frac{\alpha_S}{r} + kr, \tag{1.1}$$

where α_S is the coupling factor of the strong force, r the distance between the two objects and k ≈ 1 GeV/fm is the linear string strength [8,13]. The initial Coulombic term rises linearly with the distance r, while the second term dominates as the distance increases, and is responsible for the confinement of the quarks. As the distance between the two objects increase, the potential increases to the point where it is more energetically favorable to create a new, colour-neutral quark-anti quark pair from the vacuum instead of extending the distance further, causing the confinement of the quarks in colour neutral states, e.g., $q\bar{q}$ pairs. When the distance between the quarks decrease, however, the charges enter each others charge cloud, reducing the anti-screening effect and weakening the potential, leading to asymptotic freedom of the quarks. The

distance between the quarks also influences the coupling factor in terms of the momentum transfer, Q^2, by the relation of the momentum and position in Heisenbergs uncertainty principle, $\Delta r \Delta p \geq \frac{\hbar}{2}$. At small distances the momentum transfer is large, and vice versa, resulting in a *running coupling constant*, $\alpha_s(Q^2)$, which can be described by applying pertubative QCD (pQCD) to the mathemathical formulation of QCD, the QCD Lagrangian[4], as [10, 13]:

$$\alpha_S(Q^2) = \frac{\alpha_S(\mu^2)}{1 + \beta_0\, \alpha_S(\mu^2)\, ln(Q^2/\mu^2)} \quad \text{where} \quad \beta_0 = \frac{11N_c - 2n_f}{12\pi}, \tag{1.2}$$

with the variables being:

- $\alpha_S(\mu^2)$ Coupling factor at a given momentum transfer, μ^2.
- μ^2 Renormalization scale.
- β_0 β-function for the 1-loop approximation.
- N_c Number of colours.
- n_f Number of active flavours at the energy scale (i.e., flavours with mass $m_q < Q$).

From Equation 1.2 it can be seen that if the coupling factor is determined for a given scale $\alpha_S(\mu^2)$, the coupling factor can be predicted for any other energy scale Q^2. A common scale for quoting the value of $\alpha_S(\mu^2)$ is the mass of the Z boson, M_Z, with the current world average for $\alpha(M_Z^2)$ = 0.1181 $\pm$ 0.0013 [11]. A summary of $\alpha(Q^2)$ measurements from several experiments can be seen in Figure 1.2, displaying a good agreement with the expected behavior from Equation 1.2.

Pertubative calculations can only be performed at high energies, i.e., above ~ 1 GeV/c [8], where α_S stays below unity. As α_S increases, more complicated, non-pertubative, processes come into play, and in this energy region it is common to instead use lattice QCD (LQCD) [14] to calculate the properties of QCD. In LQCD the Euclidian space-time is discretized on a lattice with quark fields placed on the lattice sites and gluon fields on the links between sites [11]. LQCD allows us to obtain quantitative predictions through numerical calculations, such as predictions about the QCD

[4] For more information on the QCD Lagrangian, please refer to [11].

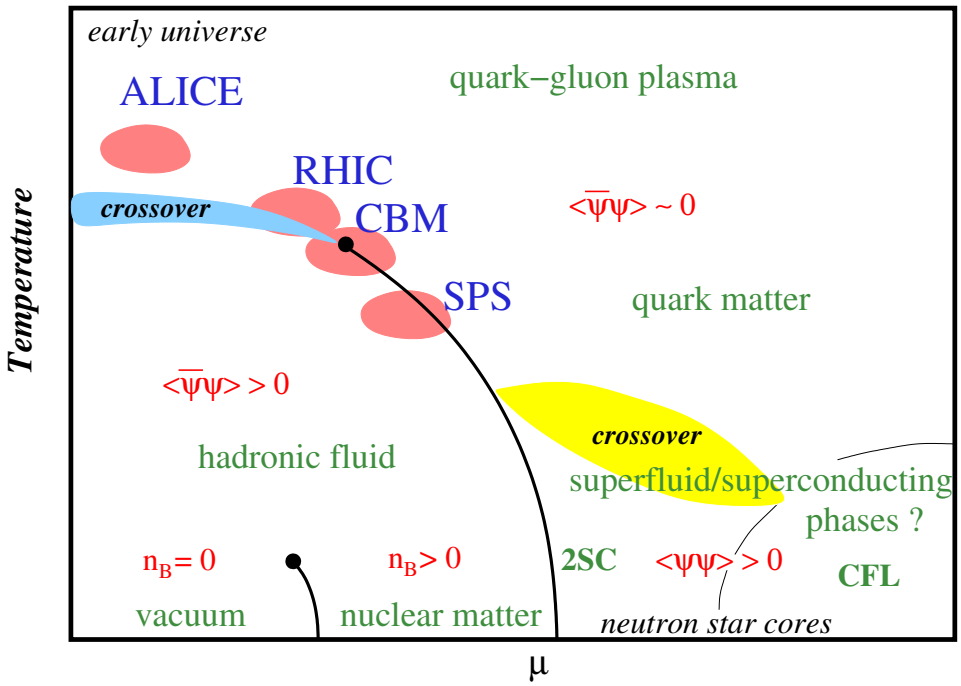

Figure 1.3: Schematic phase transition behavior of $N_f = 2+1$ flavour QCD in the (T, μ) plane [17]. As the temperature, T, and/or baryo-chemical potential, μ, increases, a transition into a Quark Gluon Plasma state takes place. The regions of study for various experiments have been indicated in the figure, including the planned CBM experiment at FAIR, GSI. The black markers, •, indicate critical points. Figure from [17].

phase diagram and the temperature at which the transition into a QGP state occurs, at approximately 170 MeV [15,16][5].

1.1.2 The Phase Diagram of QCD

Based on thermodynamical considerations and QCD calculations, strongly interacting matter is expected to exist in different states, depending on the temperature, T, and the baryo-chemical potential[6], μ, as seen in Figure 1.3. Ordinary matter is found

[5] The conversion from temperatures in K to eV is done by multiplying the temperature by the Boltzmann constant, $k = 8.617\text{x}10^{-5}$ eV K^{-1}.

[6] The baryo-chemical potential is defined as the energy, E, needed to increase the total number of baryons and anti-baryons, such as a proton or an antiproton, with one unit [18].

at low temperatures and with $\mu \simeq m_p \simeq 940$ MeV. As the energy density of the system increases by moving to larger μ (compression), or towards higher T (heating), a hadronic phase is reached and eventually, at even higher energy densities, matter enter into the deconfined Quark-Gluon Plasma (QGP) [19, 20] phase. The exact nature of the transition from the hadronic and deconfined states is a topic currently receiving considerable focus from both theorists and experimental physicists. The QGP can be reached in various ways, and as indicated in Figure 1.3, the QGP formed in the early Universe, 1 μs after the Big Bang, had a very high temperature and low μ, while the formation of neutron stars happens through a gravitational collapse, causing an increase in baryonic density at temperatures very close to zero [21, 22]. At the LHC the QGP has properties close to that of the early Universe, allowing a better understanding of the origin of the Universe, the properties of the QGP and how particles interact with it as they propagate through the medium.

1.2 The Quark Gluon Plasma

The first experimental indications of this 'new state of matter', the QGP, were presented in the beginning of year 2000 by SPS at CERN [23, 24], where lead nuclei were collided at a centre-of-mass energy per colliding nucleon pair, $\sqrt{s_{\mathrm{NN}}}$, of 17.2 GeV [25]. At the same time, the Relativistic Heavy Ion Collider (RHIC) at BNL delivered collisions of heavy nuclei, e.g., gold, at $\sqrt{s_{\mathrm{NN}}} = 200\,\mathrm{GeV}$ to the four experiments, BRAHMS, PHENIX, PHOBOS and STAR, allowing the study of a much larger and hotter QGP than previously available [25]. One of the surprising discoveries achieved by RHIC of the new, hot medium is that it is a nearly friction-less liquid, not the gas one was expecting [26–29] [18]. In 2010 and 2011, the LHC collided lead nuclei at $\sqrt{s_{\mathrm{NN}}} = 2.76\,\mathrm{TeV}$, followed up by collisions at $\sqrt{s_{\mathrm{NN}}} = 5.02\,\mathrm{TeV}$ in 2015, making it possible to study the QGP with even higher precision than before.

1.2.1 Evolution of the Quark Gluon Plasma

At RHIC and LHC nuclei are accelerated to ultra-relativistic energies in opposite directions, before they are focused onto each other in order to collide. Due to the relativistic velocities, the nuclei are strongly Lorentz contracted, making them appear as thin discs. A schematic representation of the space-time evolution of such a collision, as described by the Bjorken Model [31], is seen in Figure 1.4. The time dimension is represented at the y-axis, and the spatial dimension at the x-axis, with the collision

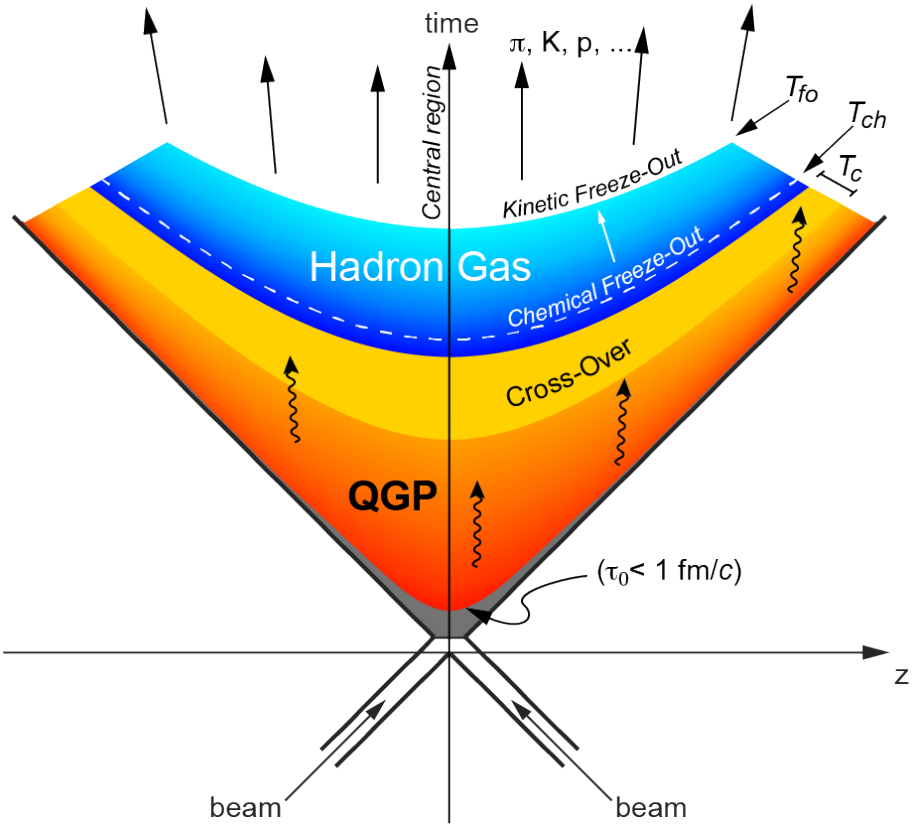

Figure 1.4: The space-time evolution of a heavy-ion collision, which undergoes a phase transition to a QGP, as described by the Bjorken model. Approximately 1 fm/c after the beams collide, a quark gluon plasma is formed which gradually expands and cools down. Figure from [30].

taking place at the origin. In the very first moments of the collision a pre-equilibrium state exists for about 1 fm/c[7], where both hard partonic scattering processes and soft interactions between the nuclei take place [18]. The very high energy density leads to the formation of the QGP, which at LHC has a lifetime of $\sim$ 10 fm/c (1.2x larger than at RHIC), reaching a volume of $R^3 \sim 300$ fm^3 (2x larger than at RHIC) [32]. After a further expansion of the system and reduction of the temperature, the quarks hadronize and the system transitions into the hadronic phase, and eventually reaches the *freeze-out*, where the structureless matter flow is converted into final hadron spectra [26], which can then be detected.

[7] 1 fm/c $\simeq$ 3.336 x 10^{-24} seconds.

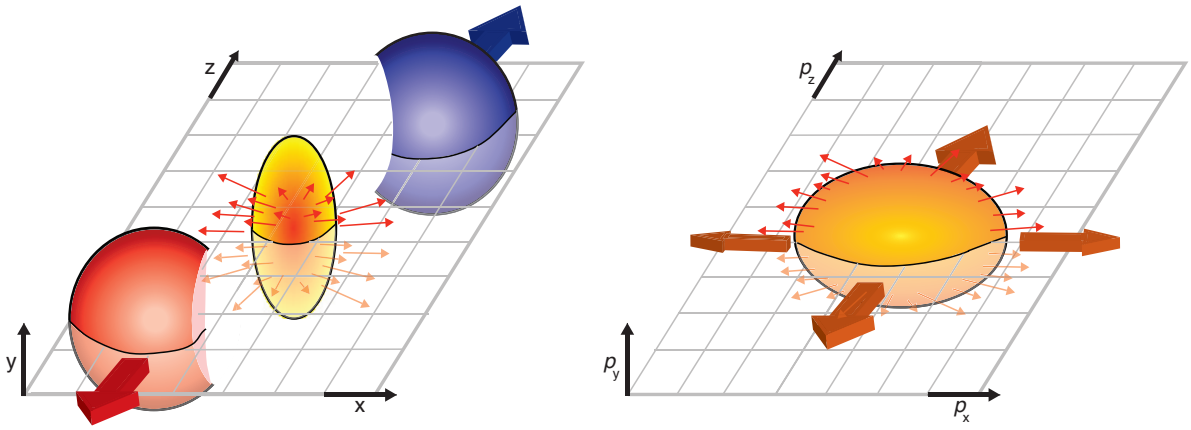

Figure 1.5: Schematic view of a non-central collision of two nuclei, in the collision plane spanned by the x-axis (impact parameter) and z-axis (beam direction). (Left): Immediately after the collision three objects can be seen in the figure, consisting of the *participants* in the centre, and the *spectators*, i.e., parts of the colliding nuclei not participating in the collision, moving away from the collision point. The participant volume is initially almond-shaped, but this spatial asymmetry is rapidly washed out due to the enhanced momentum component in the reaction plane, xz, with respect to the y direction. (Right): The initial spatial anisotropy is transferred into an anisotropic transverse momentum distribution. Figures from [33].

1.3 Observables of the Quark Gluon Plasma

After creating a QGP the next challenge is to study its properties and learn more about this exotic state of matter. A few useful observables being studied will be presented in this last section of the chapter, along with recent results from the study of these.

1.3.1 Anisotropic Flow

Anisotropic flow measures the momentum anisotropy of the final-state particles, and is sensitive to both the initial geometry of the overlap region of the colliding nuclei, and the transport properties and equation of state of the system [34]. The anisotropic flow develops from pressure gradients originating from the initial spatial geometry of a collision [35], and is commonly quantified by the harmonics, v_n, and corresponding symmetry planes, Ψ_n, of the Fourier series decomposition of the azimuthal, φ, dis-

tribution of product particles in the plane transverse to the beam direction [36, 37],

$$\frac{dN}{d\varphi} \propto 1 + 2\sum_{n=1}^{\infty} v_n cos[n(\varphi - \Psi_n)], \tag{1.3}$$

where N is the number of particles. Immediately after a non-central collisions between heavy nuclei takes place, the overlap region exhibits an ellipsoidal shape, as seen in the left panel of Figure 1.5. The exact shape is dependent on the *centrality* of the collision, a parameter related to the *impact parameter*, i.e., the distance between the centres of the two colliding nuclei[8]. As a result of multiple interactions in the reaction volume, the initial spatial anisotropy is transferred into an anisotropic transverse momentum distribution (right panel of Figure 1.5). As the spatial asymmetry rapidly decrease with time, anisotropic flow can only develop in the first fm/c [37], causing the flow to be sensitive to the properties of the created plasma due the plasma formation time being in the order of 1 fm/c [18]. Valuable information can thus be obtained about the QGP through observations of the flow.

A comparison of results for the *elliptic* (v_2), *triangular* (v_3) and *quadrangular* (v_4), flow for different transverse momenta, p_{T}, within the 30-40 % centrality range, measured at RHIC and LHC can be seen in Figure 1.6, showing excellent agreement of the various measurements between the three LHC experiments. The measurement from RHIC display a very similar shape for $v_2(p_{\mathrm{T}})$, with the peak being $\sim 10\%$ lower [34]. In collisions with an ellipsoidal reaction volume, the dominant flow coefficient is v_2, referred to as the elliptic flow coefficient, an effect clearly seen from the results. The high v_2 for $p_{\mathrm{T}} \lesssim$ 3-4 GeV/c indicates that the QGP behaves like a 'perfect fluid', as the large v_2 values require hydrodynamic models with a shear viscosity to entropy density ratio (η/s) that is close to the lower bound obtained in strong-coupling calculations, i.e., $1/4\pi$ [42]. At higher p_{T}, v_n is sensitive to the path-length dependence of the jet energy loss, and the measurements can thus be valuable for discriminating between jet-quenching models [42].

A comparison of centrality dependence of the anisotropic flow coefficients v_2, v_3 and v_4 for two- ($v_n\{2\}$) and multiparticle cumulants ($v_n\{n\}$) measured by ALICE at $\sqrt{s_{\mathrm{NN}}} = 2.76\,\mathrm{TeV}$ and $\sqrt{s_{\mathrm{NN}}} = 5.02\,\mathrm{TeV}$ is presented in Figure 1.7. The v_2 coefficient increases from central to peripheral collisions and reaches a maximum in the 40%-50% centrality class [34]. For the higher harmonics, i.e., v_3 and v_4, the values are smaller and the centrality dependence is much weaker [34]. The predictions from a hydrodynamical model [39], where previously measured values of flow harmonics

[8] The most central collisions have centralities of ∼0%, relating to an impact parameter close to zero.

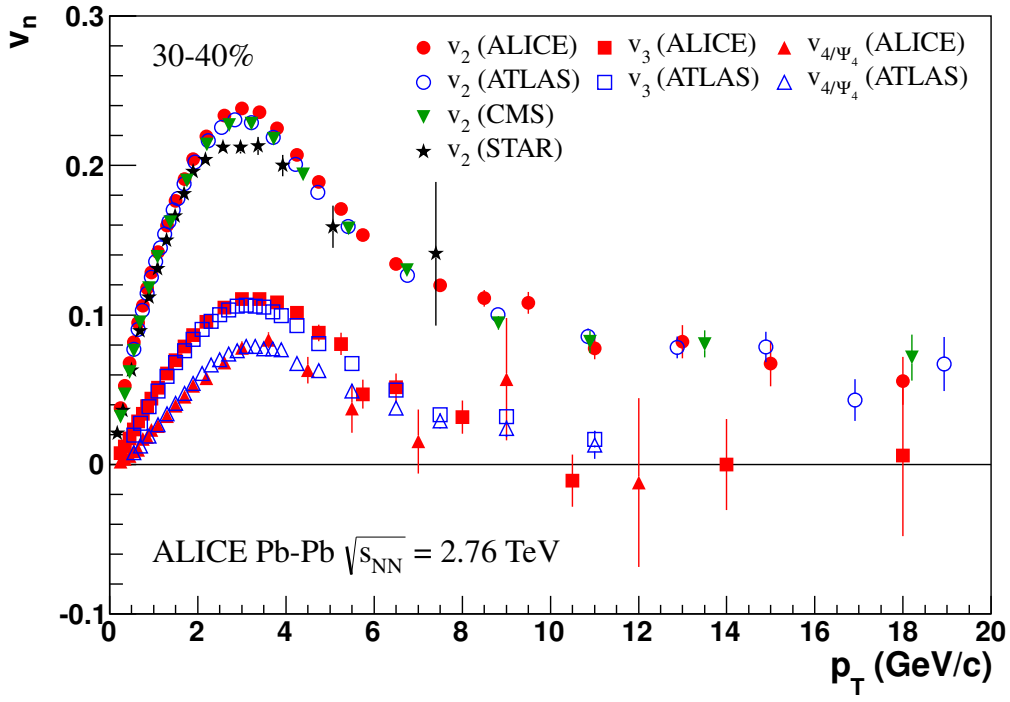

Figure 1.6: Comparison of the ALICE results on $v_n(p_{\mathrm{T}})$ obtained with the event plane method to the analogous measurements from ATLAS [26] and CMS [27] collaborations, as well as v_2 measurements by STAR [44]. Only statistical errors are shown. Figure and caption from [38].

at lower LHC energies are taken as a baseline, are compared to the measurements in the figure and found to be compatible. The increase of v_2, v_3 and v_4 was found to be (3.0 ± 0.6)%, (4.3 ± 1.4)% and (10.2 ± 3.8)% respectively, over the centrality range 0% - 50% when going from $\sqrt{s_{\mathrm{NN}}} = 2.76\,\mathrm{TeV}$ to $\sqrt{s_{\mathrm{NN}}} = 5.02\,\mathrm{TeV}$ TeV [34]. A further comparison between results of the elliptic flow at different collision energies in the 20% - 30% most central collisions is seen in Figure 1.8, where v_2 is plotted as a function of $\sqrt{s_{\mathrm{NN}}}$. An increase of (4.9 ± 1.9)% is observed when going from $\sqrt{s_{\mathrm{NN}}} = 2.76\,\mathrm{TeV}$ to $\sqrt{s_{\mathrm{NN}}} = 5.02\,\mathrm{TeV}$ [34], and an increase of 30% is observed when going from RHIC energies of $\sqrt{s_{\mathrm{NN}}} = 200\,\mathrm{GeV}$ to LHC energies of $\sqrt{s_{\mathrm{NN}}} = 2.76\,\mathrm{TeV}$ [41]. The increase in elliptic flow with increasing collision energies is caused by the increase in mean p_{T} [41].

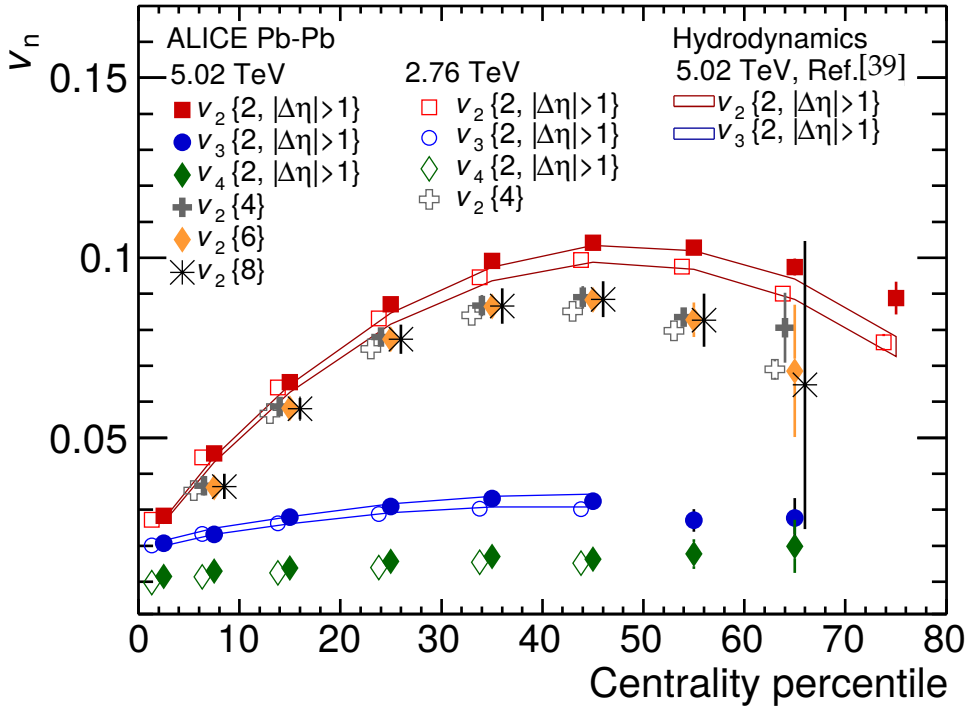

Figure 1.7: Anisotropic flow v_n integrated over the p_{T} range $0.2<p_{\mathrm{T}}<5.0$ GeV/c, as a function of event centrality, for the two-particle (with $|\Delta\eta|>1$) and multiparticle cumulant methods. Measurements for Pb–Pb collisions at $\sqrt{s_{\mathrm{NN}}} = 5.02\ (2.76)$ TeV are shown by solid (open) markers [40]. Hydrodynamical calculations are also presented [39]. The statistical and systematical uncertainties are summed in quadrature (the systematic uncertainty is smaller than the statistical uncertainty, which is typically within 5%). Data points are shifted for visibility. Modified caption and figure taken from [34].

1.3.2 Nuclear Modification

For hard processes, in the absence of nuclear and medium effects, a nucleus–nucleus (A–A) or proton–nucleus (p–A) collision would behave as a superposition of independent nucleon–nucleon collisions [45]. As a result, the differential yields, $\mathrm{d}N/\mathrm{d}_{p_{\mathrm{T}}}$, would scale from pp to p–A or A–A collisions proportionally to the number of inelastic NN collisions. Any changes in $\mathrm{d}N/\mathrm{d}_{p_{\mathrm{T}}}$ would thus provide information about additional effects taking place in the p–A and A–A collision systems, and these *nuclear modification* effects are quantified by the nuclear modification factors, R_{pA} and

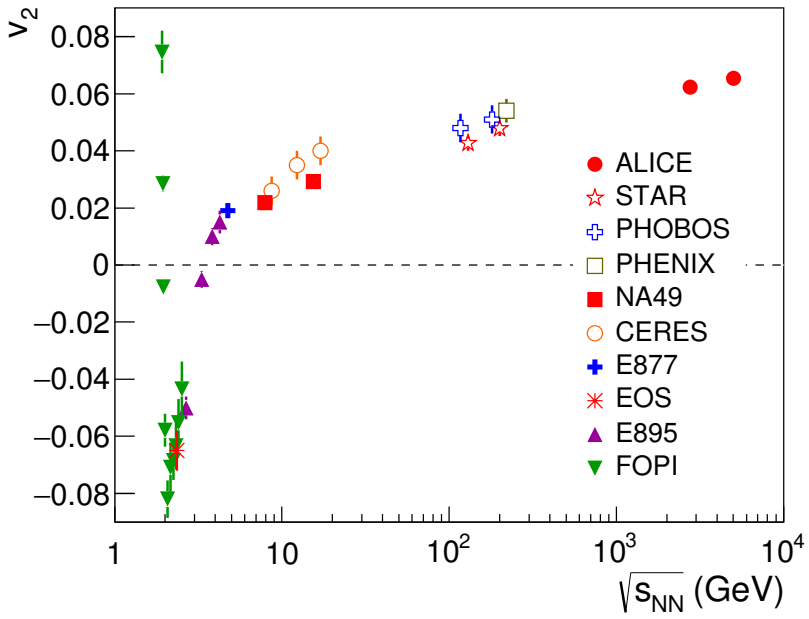

Figure 1.8: Integrated elliptic flow ($v_2\{4\}$) for the 20% - 30% most central Pb–Pb collisions at $\sqrt{s_{\mathrm{NN}}} = 5.02\,\mathrm{TeV}$ compared with v_2 measurements at lower energies with similar centralities (see Ref. [41] for references to all data points). Figure and caption from [34].

R_{AA}, defined as the ratio of the particle yield in p–A or A–A collisions to the yield in proton–proton collisions, as seen below for the R_{AA} [46]:

$$R_{\mathrm{AA}}(p_{\mathrm{T}}) = \frac{(\mathrm{d}N/\mathrm{d}_{p_{\mathrm{T}}})_{AA}}{\langle T_{\mathrm{AA}}\rangle\,(\mathrm{d}\sigma/\mathrm{d}_{p_{\mathrm{T}}})_{pp}}, \tag{1.4}$$

where $(\mathrm{d}N/\mathrm{d}_{p_{\mathrm{T}}})_{AA}$ is the differential particle yield in nucleus–nucleus collisions[9], $\langle T_{\mathrm{AA}}\rangle$ is the average nuclear overlap function evaluated by a Glauber Monte Carlo model [47], and $(\mathrm{d}\sigma/\mathrm{d}_{p_{\mathrm{T}}})_{pp}$ is the differential cross section in proton–proton collisions. With no nuclear and medium effects present, R_{AA} is expected to be equal to unity. A $R_{\mathrm{AA}}< 1$ indicates suppression in the medium, and $R_{\mathrm{AA}}> 1$ indicates enhancement.

[9] For the p–A case, the R_{pA} is defined in the same way, using $(\mathrm{d}N/\mathrm{d}_{p_{\mathrm{T}}})_{pA}$ instead of $(\mathrm{d}N/\mathrm{d}_{p_{\mathrm{T}}})_{AA}$.

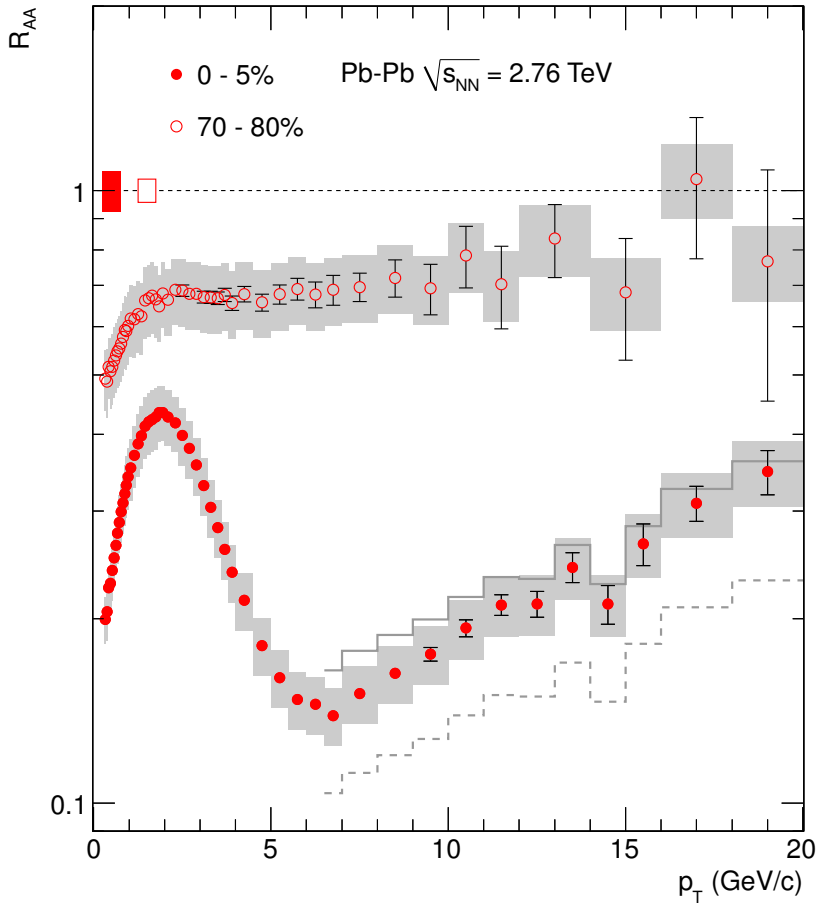

Figure 1.9: R_{AA} in central (0–5%) and peripheral (70–80%) Pb–Pb collisions at $\sqrt{s_{NN}} = 2.76$ TeV. Error bars indicate the statistical uncertainties. The boxes contain the systematic errors in the data and the p_T dependent systematic errors on the pp reference, added in quadrature. The histograms indicate, for central collisions only, the result for R_{AA} at $p_T > 6.5$ GeV/c using alternative pp references obtained by the use of the p$\bar{\text{p}}$ measurement at $\sqrt{s_{NN}} = 1.96$ TeV [43] in the interpolation procedure (solid) and by applying NLO scaling to the pp data at 0.9 TeV (dashed). The vertical bars around $R_{AA} = 1$ show the p_T independent uncertainty on $\langle N_{\text{coll}} \rangle$. Caption and Figure from [44].

The R_{AA} has been measured for central (0–5%) and peripheral (70–80%) Pb–Pb collisions at $\sqrt{s_{\mathrm{NN}}} = 2.76\,\mathrm{TeV}$ at the LHC by ALICE, as seen in Figure 1.9. A suppression is observed for both the central and peripheral collisions, though the shape deviates above $p_{\mathrm{T}} \simeq 2\ \mathrm{GeV}/c$. The R_{AA} for peripheral events show less suppression than for central events, and shows no pronounced p_{T} dependence for p_{T}>2 GeV/c [44]. For central collisions the R_{AA} reaches a maximum at $\sim 2\ \mathrm{GeV}/c$, followed by a decline towards a minimum at $\sim$ 6-7 GeV/c, followed by an increase towards higher p_{T}. A comparison of the results from ALICE with those of STAR and PHENIX is presented in Figure 1.10. At 1 GeV/c the R_{AA} measured at LHC and RHIC is similar. The shape of the distribution and the position of the maximum, at $\sim 2\ \mathrm{GeV}/c$ is similar for the results from all three experiments, but a larger suppression is seen at ALICE, indicating enhanced energy loss and a denser medium created at LHC. A quantitative description of the energy loss mechanisms require further investigation and theoretical modeling [44].

Particles which do not interact strongly are not expected to interact with the QCD medium, and thus should not be suppressed while propagating through it. Measurements of the R_{AA} have been made by CMS at LHC for electro-weak bosons (photons, W and Z particles), as seen in Figure 1.11, displaying a good agreement with the predictions. The figure also shows a comparison between the ALICE and CMS measurement of the R_{AA} for charged particles in Pb–Pb collisions at $\sqrt{s_{\mathrm{NN}}} = 2.76\,\mathrm{TeV}$ which are in excellent agreement. Finally the R_{pA} measured by ALICE is shown to be compatible with unity up to p_{T}=50 GeV/c, with indications of a small enhancement around 4 GeV/c, where the much stronger Cronin peak is seen [50, 51] at lower energies [52]. The measurements of R_{pA} provide important constraints to models of nuclear modification effects.

1.3.3 Jet Modification and Dihadron Correlations

In the hard scattering events in the very first moments of heavy ion collisions, high energy partons are created. As this process takes place even before the QGP is formed, these partons experience the full evolution of the hot, dense medium, and in that sense act as excellent probes of the medium properties. The hard scattered partons can produce collimated parton showers, or *jets*, via hadron fragmentation processes, and due to the partons being created back-to-back, the most common type of jet events are *dijets*, where two jets emerge in opposite directions. As jets propagate through the me-

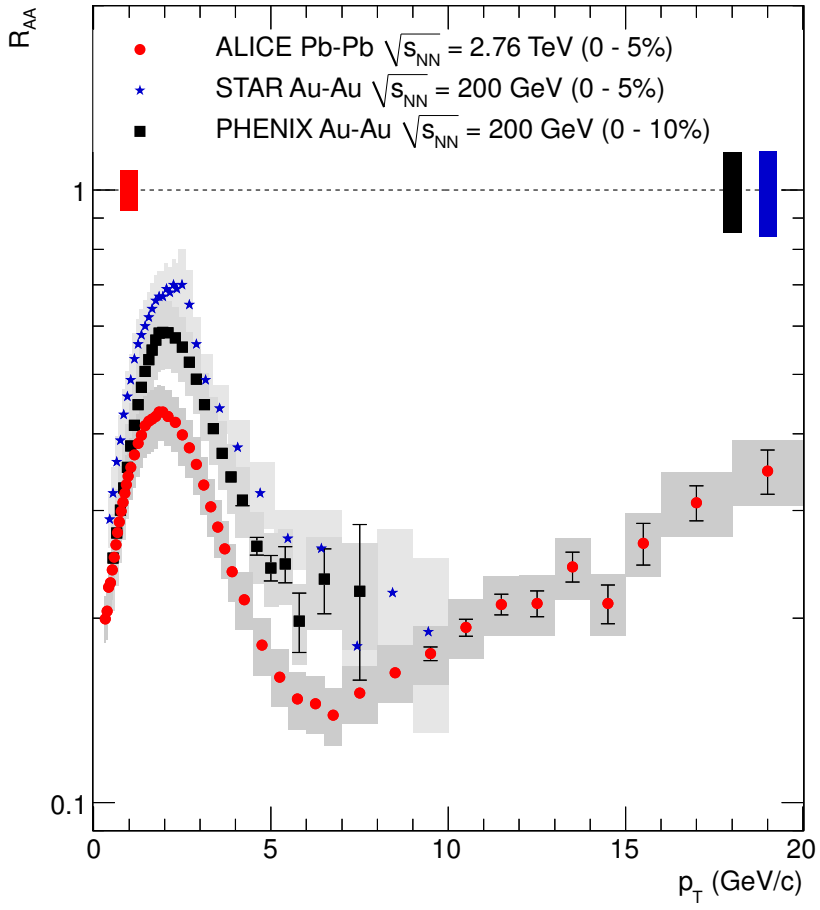

Figure 1.10: Comparison of R_{AA} in central Pb–Pb collisions at LHC to measurements at $\sqrt{s_{NN}} = 200$ GeV by the PHENIX [48] and STAR [49] experiments at RHIC. The error representation of the ALICE data is as in Fig. 1.9. The statistical and systematic errors of the PHENIX data are shown as error bars and boxes, respectively. The statistical and systematic errors of the STAR data are combined and shown as boxes. The vertical bars around $R_{AA} = 1$ indicate the p_T independent scaling errors on R_{AA}. Caption and Figure from [44].

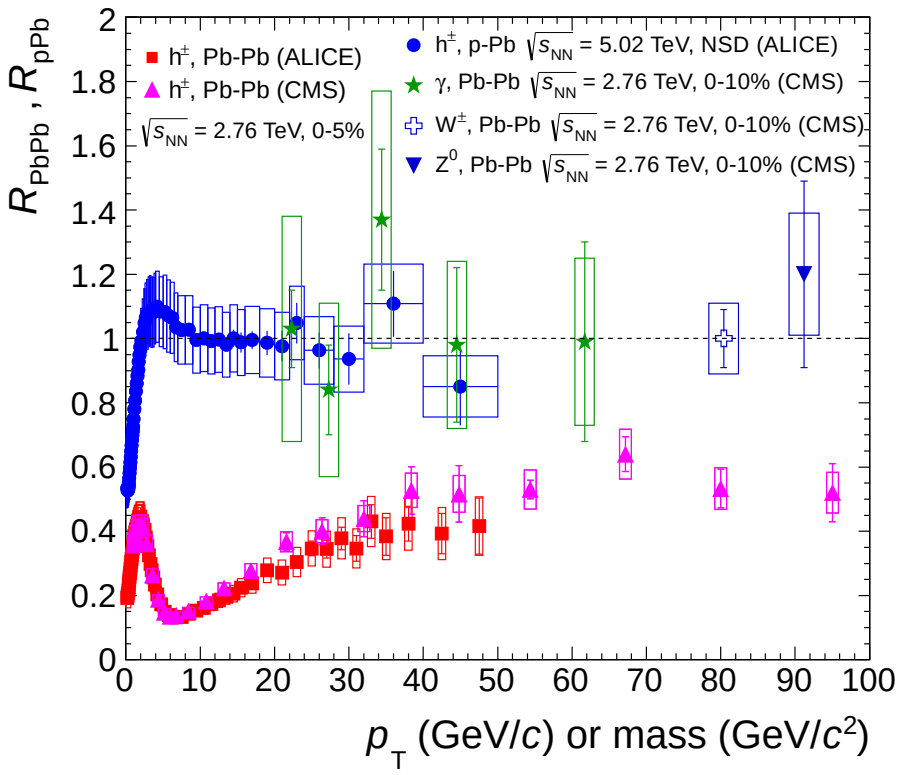

Figure 1.11: The R_{AA} for charged particles in the 5% most central Pb–Pb collisions at $\sqrt{s_{\mathrm{NN}}} = 2.76\,\mathrm{TeV}$ is compared for ALICE and CMS [53]. The results are also compared to those for W and Z bosons as well as isolated photons measured by CMS [54–56]. The R_{pA} for p–Pb collisions at $\sqrt{s_{\mathrm{NN}}} = 5.02\,\mathrm{TeV}$ measured by ALICE is also shown. Figure and caption from [57].

dium they interact with it through multiple interactions, causing them to lose energy. The suppression of such jets from their interactions with the colour-charged medium was suggested as an observable of the QGP by Bjorken [59], suggesting also the possibility of spectacular events where jets produced in the peripheral regions, i.e., near the 'edges', of the QGP, force one of the jets to traverse a large portion of the medium, losing most of its energy, while the other jet has a much smaller path to travel before it leaves the QGP, allowing it to escape the medium mostly unharmed. Such an event would be observed as a high p_{T} jet on one side of the detector, and a very small contribution at the opposite side in the azimuthal plane, φ, and is referred to as

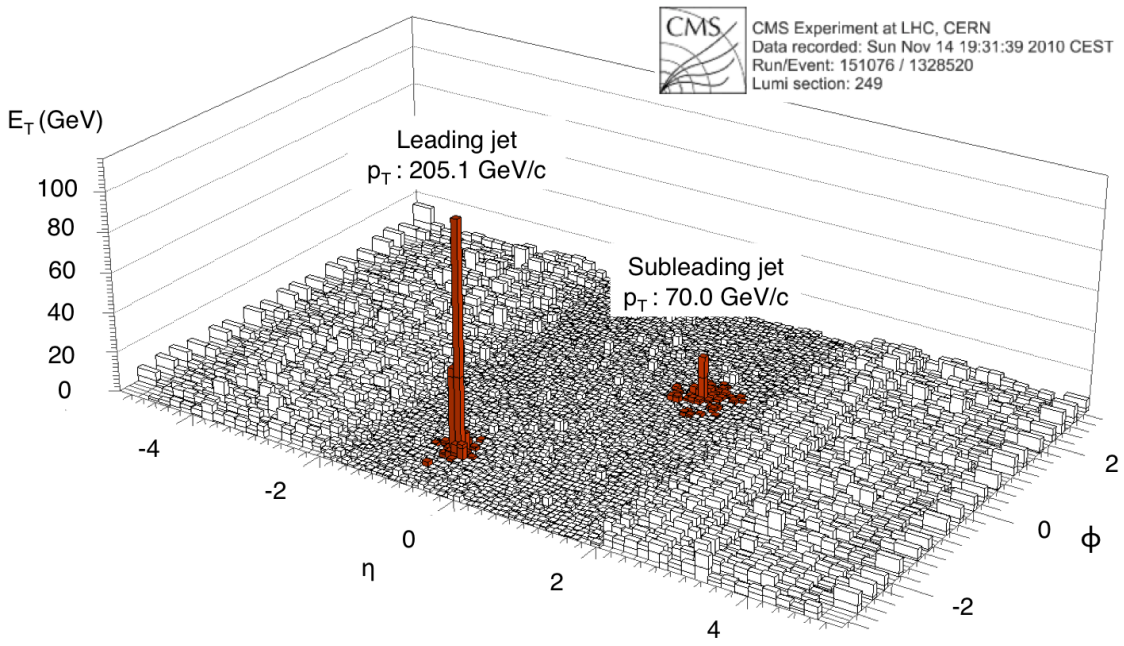

Figure 1.12: Example of an unbalanced dijet in a Pb–Pb collision event at $\sqrt{s_{\mathrm{NN}}} = 2.76\,\mathrm{TeV}$. Plotted is the summed transverse energy in the electromagnetic and hadron calorimeters vs. η and φ, with the identified jets highlighted in red, and labeled with the corrected jet transverse momentum. Figure and caption from [58].

a highly asymmetric dijet. This phenomena has been observed in Pb–Pb collisions at CMS [58] and ATLAS [60], where dijets are studied on an event-by-event basis, by selecting events where, in the case of CMS, a jet with $p_{\mathrm{T}} > 120\ \mathrm{GeV}/c$ (*leading jet*)[10] and a second (*subleading jet*) with $p_{\mathrm{T}} > 50\ \mathrm{GeV}/c$ is found[11]. The reasoning of the relatively low p_{T} limit on the subleading jets is the increasing difficulty as the p_{T} decreases of reliably detecting them above the underlying event, which becomes dominating below $p_{\mathrm{T}} <$ 35-50 GeV/c [58]. An example from CMS of a dijet observation where the subleading jet is strongly suppressed is seen in Figure 1.12. The jets are defined using cones with a given radius $\Delta R = \sqrt{\Delta\varphi^2 + \Delta\eta^2}$, spanned by the azimuthal angle, φ, and pseudorapidity η, where particles above a given p_{T} threshold are counted to

[10] The leading jet is the jet with the highest p_{T} in the event, while the subleading jet is the one with the second highest p_{T}.

[11] ATLAS requires the leading jet to have a transverse energy, $E_{T1} > 100\mathrm{GeV}/c$, and the subleading jet to have a transverse energy $E_{T2} > 25\ \mathrm{GeV}/c$.

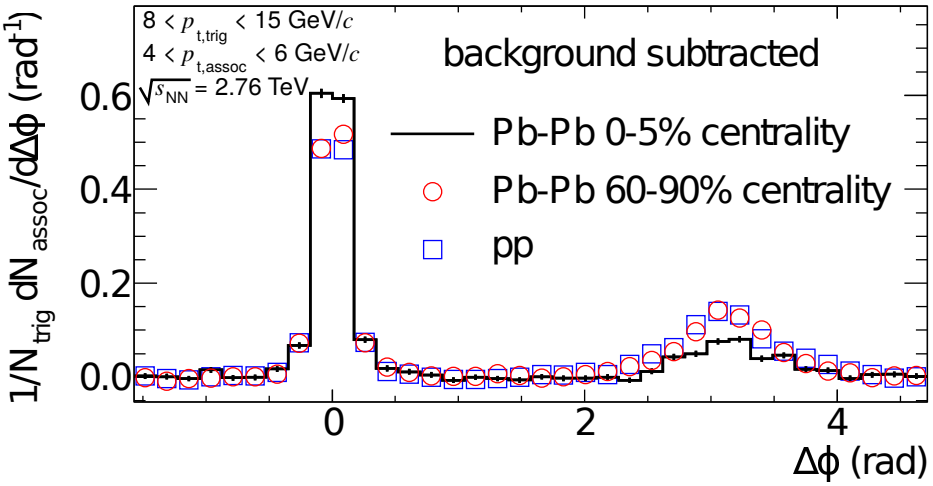

Figure 1.13: Per-trigger pair yield for central Pb-Pb events (histogram), peripheral Pb–Pb events (red circles) and pp events (blue squares), measured by ALICE at $\sqrt{s_{\rm NN}} = 2.76\,\text{TeV}$. The distributions are background subtracted using a flat pedestal calculation. Modified figure and caption from [58].

be within the jet. A strong dijet asymmetry has been reported for central heavy ion collisions, by CMS and ATLAS, with an increase in the momentum inbalance as a function of centrality [58, 60]. Further it was observed that the momentum balance was recovered if tracks at low $p_{\rm T}$ were included, as a large fraction of the balancing momentum was carried by tracks having $p_{\rm T}$< 2 GeV/c [58].

The previously mentioned difficulty of identifying jets above the underlying event at $p_{\rm T}$ lower than $\sim$ 35-50 GeV/c means that other methods, such as *dihadron correlations*, are required for studying the medium effects in these regions. In dihadron correlations, the difference between the azimuthal angle, $\Delta\varphi$ and pseudorapidity, $\Delta\eta$, between pairs of hadrons is measured, and a correlation function plotted against the associated per trigger yield is studied [18]:

$$\frac{\mathrm{d}^2N}{\mathrm{d}\Delta\varphi\,\mathrm{d}\Delta\eta}(\Delta\varphi,\Delta\eta) = \frac{1}{N_{trig}}\frac{\mathrm{d}^{\mathrm{N}}_{\mathrm{assoc}}}{\mathrm{d}\Delta\varphi\mathrm{d}\,\Delta\eta}. \tag{1.5}$$

A projection of the $\Delta\varphi$ distribution is commonly presented, and is referred to as the azimuthal angular correlation distribution. The particles are generally defined as the *trigger* and *associated* particles, selected according to a given set of criteria for the analysis. The trigger particle is defined to be located at $\Delta\varphi$=0 (near-side), and

for a trigger and associated particle emerging back-to-back from a common origin, the associated particle is expected to be located at $\Delta\varphi$=π (away-side). An azimuthal angular dihadron correlation distribution measured at $\sqrt{s_{\mathrm{NN}}} = 2.76\,\mathrm{TeV}$ Pb–Pb collisions at ALICE is seen in Figure 1.13, displaying the expected near- and away-side structures. An enhancement in the Pb–Pb distribution in central collisions can be seen compared to peripheral Pb–Pb collisions and pp collisions. In addition a suppression of the away-side peak is seen for central Pb–Pb collisions compared to the two other scenarios. The yields per trigger particle, Y, of the near- and away-side peaks are quantified by calculating the integral of the distributions in the region where the signal is significantly above the background, i.e., within $\Delta\varphi \pm 0.7$ and $\pi \pm 0.7$ in the near- and away-side peaks respectively, for the distributions of Figure 1.13 [61]. The calculated yields for Pb–Pb collisions, Y_{Pb-Pb}, and pp collisions, Y_{pp}, were used to compute the ratio between the Pb–Pb and pp yields, $I_{AA} = Y_{Pb-Pb}/Y_{pp}$, where the subscripts denote the collision systems. In addition the ratio between central (0-5%) and peripheral (60-90%) were calculated, $I_{CP} = Y_{0-5\%}/Y_{60-90\%}$. The calculated I_{AA} and I_{CP} can be seen in Figure 1.14. The I_{AA} (Fig 1.14 (upper)) displays an away-side suppression in central collisions, a sign of in-medium energy loss, in agreement with measurements at lower energies at STAR [62]. The 20-30% enhancement above unity observed at the near-side, however, has not been observed at lower energies [61]. For peripheral collisions there is no significant deviation from unity in either the near- or away-side, as expected in the absence of in-medium effects. The I_{CP} (Fig. 1.14 (lower)) is in good agreement with the I_{AA} in central collisions with respect to the near-side enhancement and away-side suppression [61]. Combining the knowledge gained from I_{AA} and R_{AA} measurements can provide useful information about the energy-loss mechanisms in the QGP, and help constrain the parameters of jet quenching models.

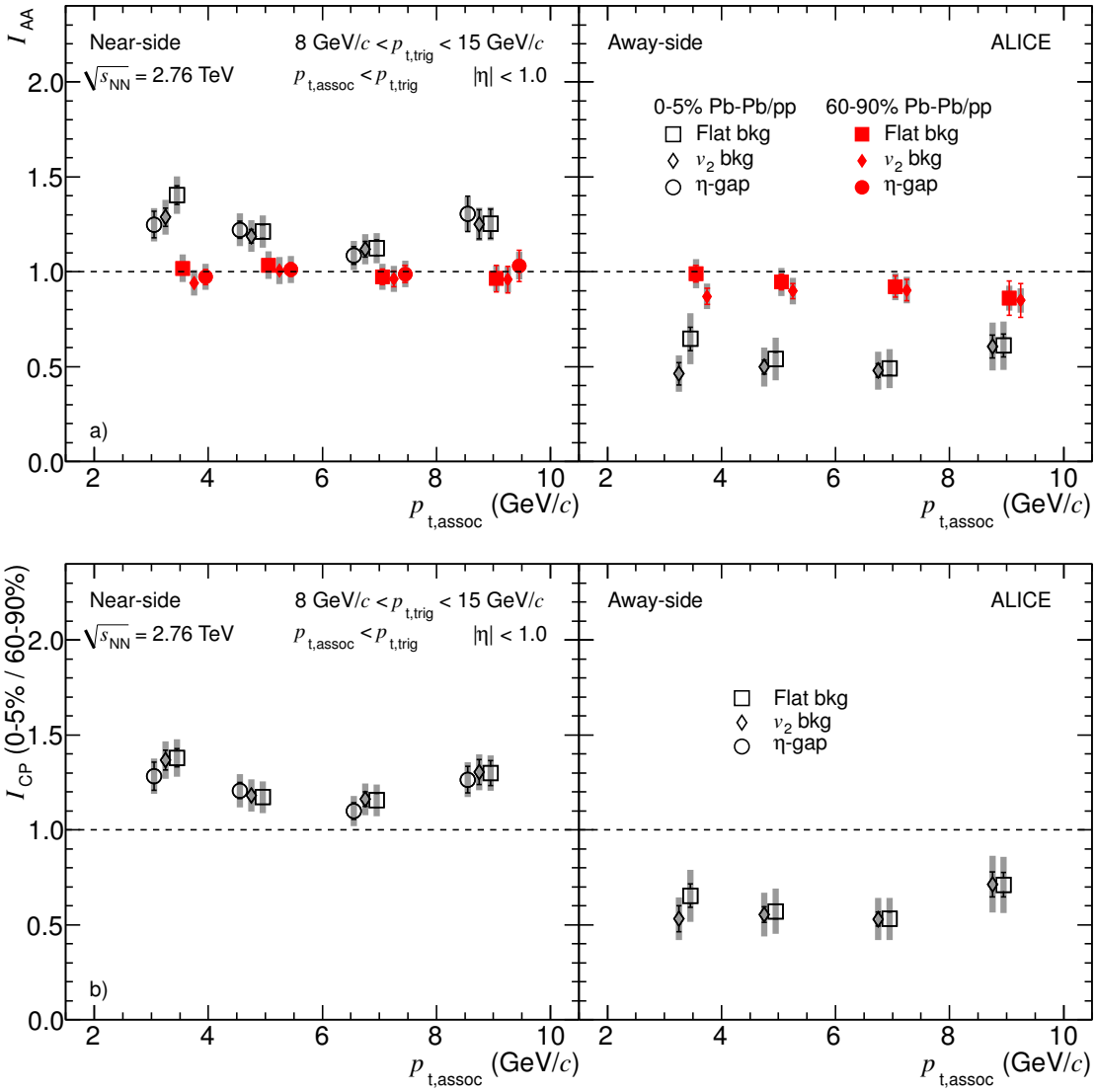

Figure 1.14: (a) I_{AA} for central (0%-5% Pb–Pb/pp, open black symbols) and peripheral (60%-90% Pb–Pb/pp, filled red symbols) collisions and (b) I_{CP}. The different marker shapes represent results using different background subtraction schemes (for details see [61]). For clarity, the data points are slightly displaced on the $p_{t,assoc}$ axis. The shaded bands denote systematic uncertainties. Figures and modified caption from [61].

Chapter 2

Heavy Flavour

Heavy-flavour quarks (charm and beauty[1]) are ideal probes for studying the QGP. Due to their relatively high masses, heavy-flavour quarks can only be produced in the initial hard (large momentum transfer) scattering processes of the collision. Having a shorter formation time ($\sim$0.1 fm/c for charm and $\sim$0.01 fm/c for beauty) than the QGP ($\sim$ 0.3 fm/c) at LHC energies [63, 64], heavy-flavour quarks will experience the full evolution of the QGP, and can be studied to obtain information about the medium.

This chapter will begin with a brief introduction to partonic energy loss, in order to provide a basic insight in how partons of various types interact as they propagate through different mediums. Section 2.2 presents recent results of D meson production in pp collisions, along with comparisons to results from the p–Pb and Pb–Pb systems. Finally, heavy-flavour correlations, which is the focus of this thesis, will be introduced in Section 2.3.

2.1 Partonic Energy Loss

Partons are subject to energy loss through interactions with the QGP, due to *collisional energy loss* from elastic collisions with the medium constituents, and gluon radiation caused by inelastic scattering (*radiative energy loss*). The energy loss of a particle depends both on the properties of the particle, e.g., its colour charge and mass, and the properties of the medium, e.g., the medium density, thickness and temperature. The radiative component of the energy loss is expected to be the main contributor

[1] The top quark is also a heavy-flavour quark, but is not considered in this thesis.

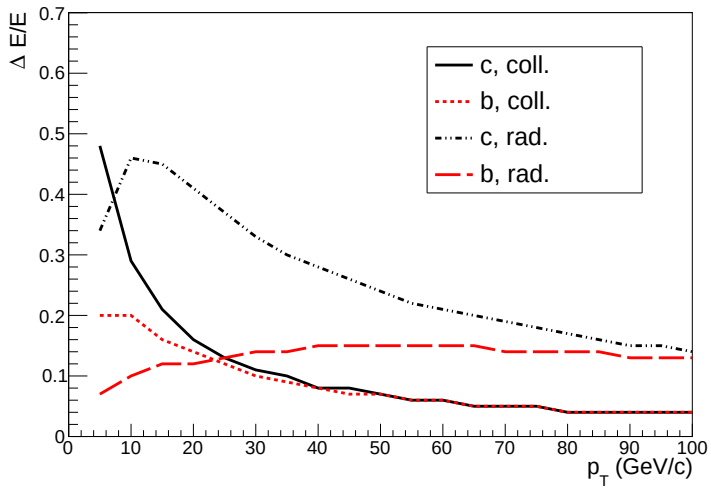

Figure 2.1: Fractional energy loss evaluated for collisional and radiative processes, for charm and beauty quarks traversing a QGP at a constant temperature of T = 304 MeV, with a path length, $L = 5\mathrm{fm}$, using the energy loss formalism by Djordjevic *et al.*. Figure from [65].

to parton energy loss, but for a wide kinematical region the collisional energy loss is comparable in magnitude [66], in particular for heavy-flavour partons [67]. A comparison of the fractional energy loss, $\frac{\Delta E}{E}$, for collisional and radiative processes of charm and beauty quarks traversing a finite size QGP, as described by the dynamical energy loss formalism by Djordjevic *et al.* [68–70] is seen in Figure 2.1. While several different models are available[2], the Djordjevic model has been chosen for the narrative in this section, as it considers both radiative [68,69] and collisional [70] energy loss processes, of both light and heavy partons, in a medium of moving (dynamical) particles [65]. In the figure, the energy loss of the charm and beauty is calculated while traversing a path length, L = 5 fm, through a QGP with temperature, T = 304 MeV, by the given expression [65]:

$$\frac{\Delta E_{\mathrm{dyn}}}{E} = \int \mathrm{d}x\mathrm{d}^2k\, x\frac{\mathrm{d}^3N^g}{\mathrm{d}x\mathrm{d}^2k} \tag{2.1}$$

with the radiation spectrum [65]:

$$\frac{\mathrm{d}^3N^g}{\mathrm{d}x\mathrm{d}^2k} = \frac{C_R\alpha_s}{\pi}\frac{L}{\lambda_{\mathrm{dyn}}}\int\frac{\mathrm{d}^2q}{x\pi^2}\,v_{\mathrm{dyn}}(\vec{q})\left(1-\frac{\sin\left(\frac{(\vec{k}+\vec{q})^2+\chi}{xE^+}L\right)}{\frac{(\vec{k}+\vec{q})^2+\chi}{xE^+}L}\right)\frac{2(\vec{k}+\vec{q})}{(\vec{k}+\vec{q})^2+\chi}\left(\frac{(\vec{k}+\vec{q})}{(\vec{k}+\vec{q})^2+\chi}-\frac{\vec{k}}{\vec{k}^2+\chi}\right), \tag{2.2}$$

[2] Several of the results in Section 2.2 are compared to various models.

where the variables are as follows:

- $\vec{q}$ and $\vec{k}$: the momentum of the radiated gluon and the momentum of the exchanged virtual gluon with a parton in the medium, with both $\vec{q}$ and $\vec{k}$ transverse to the jet direction.
- $\lambda_{\mathrm{dyn}}^{-1} \equiv C_2(G)\alpha_s T$: the *dynamical mean free path* [68].
- $C_2(G) = 3$: the gluon quadratic Casimir invariant.
- α_s: the strong coupling constant.
- T: Temperature of the medium.
- C_R: the Casimir factor, with a value of $4/3$ for quarks and 3 for gluons.
- $v_{\mathrm{dyn}}(\vec{q}) = \frac{\mu_E^2}{\vec{q}^2(\vec{q}^2+\mu_E^2)}$: the effective potential.
- χ: defined as $m_Q^2 x^2 + m_g^2$, where m_Q is the heavy-quark mass, x is the longitudinal momentum fraction of the heavy quark carried away by the emitted gluon and $m_g = \frac{\mu_E}{\sqrt{2}}$ is the effective mass for gluons with hard momenta ($k \gtrsim T$).
- μ_E: the Debye mass.

The model takes into account several interesting aspects regarding the dependencies of the energy loss. From Figure 2.1 it is seen that the radiative energy loss starts to dominate for p_{T} >10 GeV/c in the case of charm quarks, while for beauty quarks the transition happens at p_{T} >25 GeV/c, illustrating a significant quark mass dependence, which disappears when $p_{\mathrm{T}} \gg m_Q$. This quark mass dependence is generally attributed to the *dead cone effect* [71], i.e., the suppression of radiation at angles smaller than the ratio of the quark mass and its energy, resulting in less radiative energy loss for heavier partons. This mass dependence is encoded in the χ term of Equation 2.2, which is reduced for increasing values of $m_Q/(\vec{k}+\vec{q})$.

A colour charge dependence of the energy loss is encoded in the Casimir coupling factor, C_R, which takes on the value of $4/3$ for quarks and 3 for gluons. Gluons will thus have a higher probability of radiating a gluon compared to that of quarks, resulting in a higher energy loss for gluons compared to quarks. As light-flavour hadrons originate mostly from gluon or light-quark jets, a higher suppression of light-flavour quarks compared to heavy-flavour quarks is expected for p_{T} up to about 10 GeV/c [67]. Thus, both the colour-charge dependence and the dead cone effect favor higher energy loss for lighter partons compared to the heavier ones.

2.2 Heavy-Flavour Measurements

Heavy-flavour production and modification is measured at ALICE in the three available collision systems provided by the LHC, namely pp, p–Pb and Pb–Pb. Measurements in pp collisions acts as a sensitive test of pQCD calculations, which at ALICE can be studied down to low p_{T}, where pQCD calculations have substantial uncertainties and thus benefit greatly from constraints from experiments. Additionally, measurements in pp and p–Pb collisions provide important references for results in heavy-ion collisions.

In Section 1.3.2, the concept of nuclear modification was introduced, i.e., the deviation from a scaling by the number of binary collisions of the p–Pb or Pb–Pb particle yields from the yields in pp collisions. The deviation is generally divided into two classes, *initial state effects*, caused mainly by differences in the parton distribution functions in collisions of bound nucleons compared to those of free nucleons, and *final state effects*, caused by modifications of heavy-flavour observables as they interact with the hot and dense medium created in heavy-ion collisions. In order to obtain a complete understanding of the results in Pb–Pb collisions, the pp and p–Pb systems have to be understood, and thus measurements in pp and p–Pb collisions play an important role to disentangle the initial and final state effects. In p–Pb collisions the various effects related to the presence of nuclei in the colliding system, referred to as CNM effects, are evaluated, and can thus be distinguished from the effects of the hot, dense QGP medium formed in Pb–Pb collisions. While the total heavy-flavour yield is sensitive to modifications of the initial parton densities, it is not expected to be changed significantly via final state effects. Various final state effects are, however, expected to affect the phase-space distribution of the heavy-flavour hadrons [67]. Partons traversing and interacting with the medium is subject to partonic energy loss (see Section 2.1), resulting in a softening of the p_{T} distributions of heavy-flavour hadrons or their decay products with respect to p–p collisions.

Recent measurements of heavy-flavour at the LHC will be discussed for the various collision systems in the following.

2.2.1 Heavy-Flavour Measurements in p–p Collisions

Heavy-flavour production at ALICE is commonly studied via the reconstruction of the prompt charmed mesons, D^0, D^+ and D^{*+}through their hadronic decay chan-

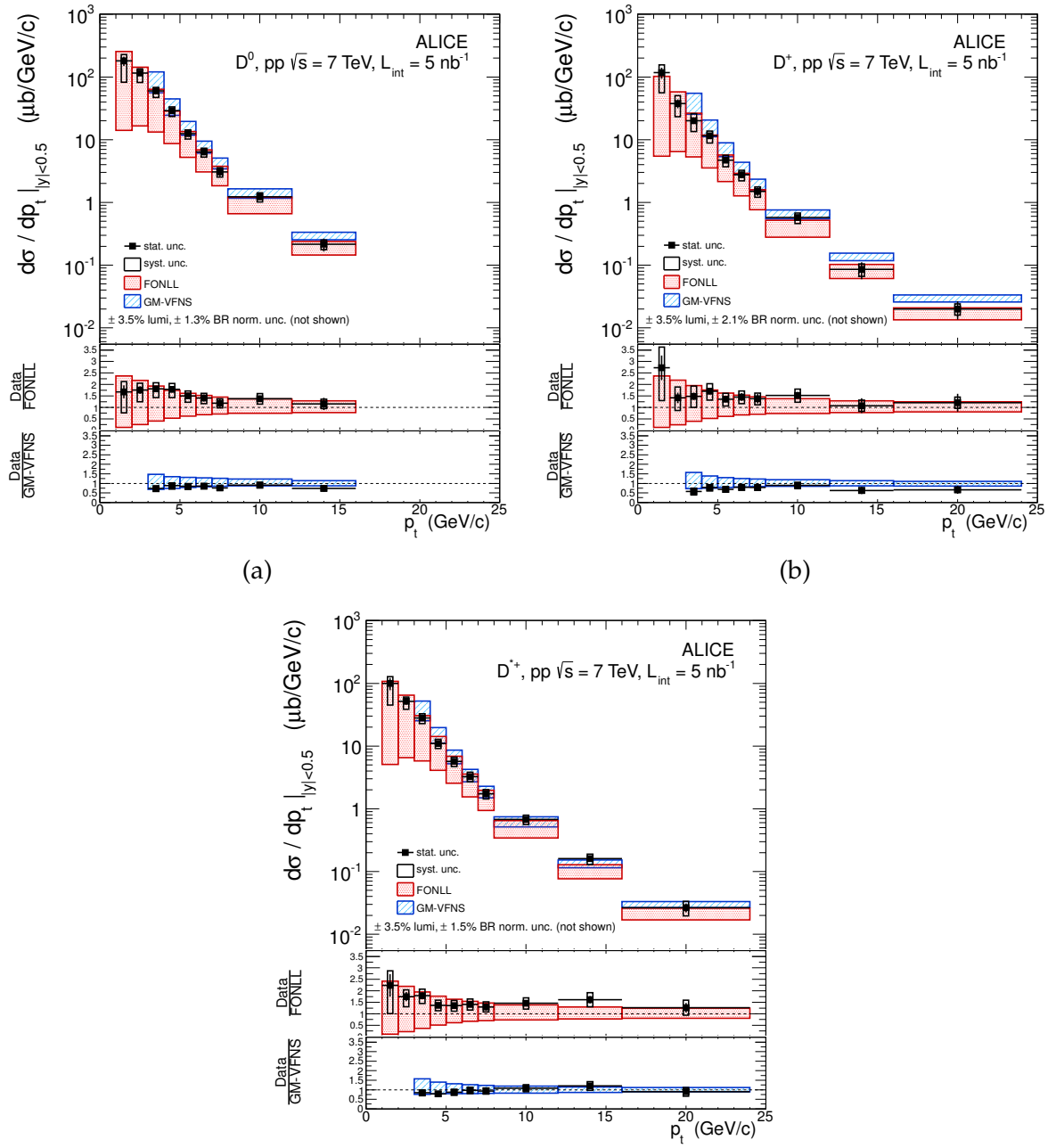

Figure 2.2: p_{T} differential inclusive cross section for prompt (a) D^0, (b) D^+ and (c) D^{*+} mesons in pp collisions at $\sqrt{s} = 7\,\mathrm{TeV}$, compared with FONLL and GM-VFNS theoretical predictions [72]. The results are compatible within uncertainties to both of the theoretical calculations. Figure from [72].

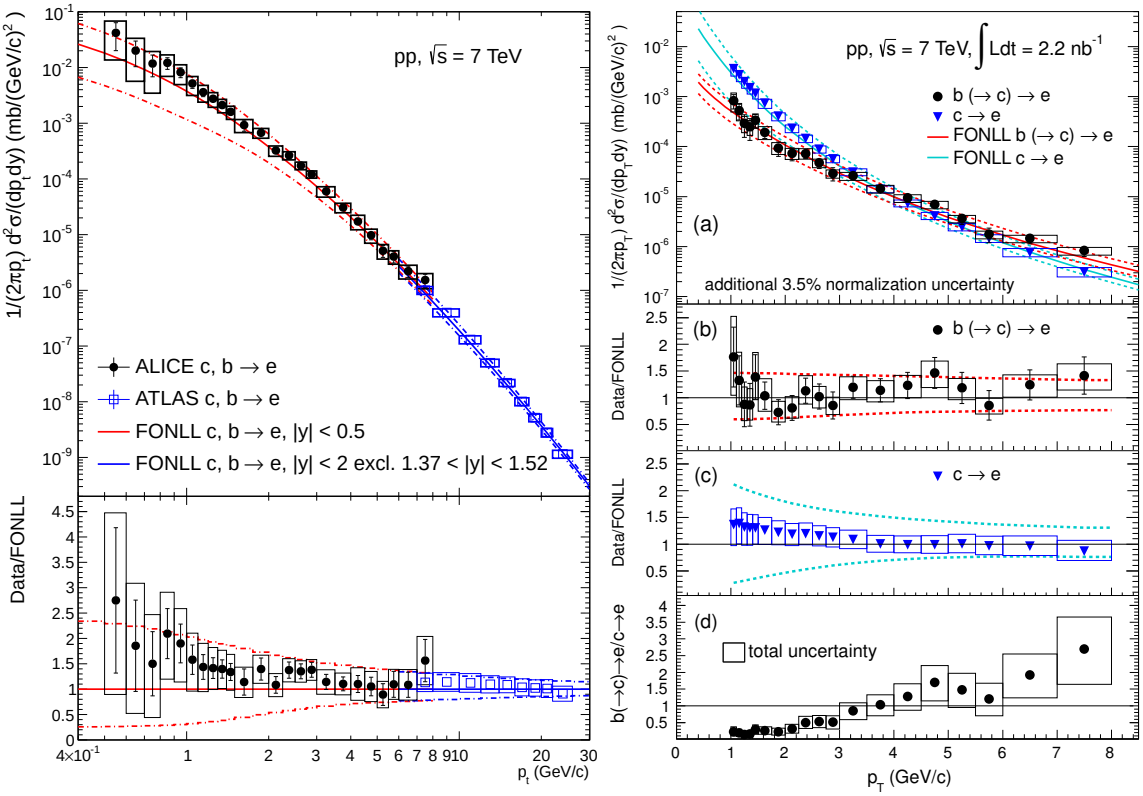

Figure 2.3: (Left) Invariant differential production cross sections of electrons from heavy-flavour decays, measured by ALICE and ATLAS in pp collisions at $\sqrt{s} = 7\,\mathrm{TeV}$, compared to fixed order with next-to-leading-log resummation (FONLL) pQCD calculations with the same rapidity selection [73]. The results from ALICE and ATLAS are complementary, and the results show an agreement to theoretical predictions within theoretical and experimental uncertainties. (Right) (a) p_{T} invariant cross sections of electrons from beauty (black circles) and charm (blue triangles) measured by ALICE in pp collisions at $\sqrt{s} = 7\,\mathrm{TeV}$. The ratio between data and FONLL predictions has been computed for (b) beauty decays and (c) charm decays, where the dashed lines indicate the FONLL uncertainties. A good agreement between the data and theoretical predictions is observed. (d) The ratio of electrons from beauty and charm hadron decays illustrates that charm dominates for low p_{T}, while beauty hadron decays dominate above $p_{\mathrm{T}} \sim 4\,\mathrm{GeV}/c$ [74].

nels[3]. The p_{T}-differential production cross sections of these decay channels were measured by ALICE in pp collisions at $\sqrt{s} = 7\,\mathrm{TeV}$, as shown in Figure 2.2. The results were compared to two variations of pQCD predictions, at next-to-leading order (NLO) accuracy in the general-mass variable-flavour-number scheme (GM-VFNS) [75,76], and at FONLL [77,78] precision, and was found to be compatible within uncertainties to both calculations [72]. The central value of the GM-VFNS predictions was found to lie systematically above the data, while that of the FONLL predictions lies below the data [72].

The heavy-flavour production has also been studied by measuring the inclusive differential cross section of electrons from semileptonic heavy-flavour hadron decays, referred to as HFE in this thesis, by the ALICE [73] and ATLAS [79] experiments, as seen in Figure 2.3 (left). The measurements from ALICE includes most of the total cross section, while ATLAS extends the measurement to higher p_{T}. The measurements were compared to FONLL calculations, and an agreement was found within the experimental and theoretical uncertainties [73]. Electrons from semileptonic hadron decays can be separated in ALICE by exploiting the excellent vertexing capabilities of the Inner Tracking System (ITS) detector [67,74]. In Figure 2.3 (right), differential cross sections of electrons from beauty and charm hadron decays are compared separately to FONLL predictions, and found to be in good agreement [74]. From Figure 2.3 (right, d) it can be seen that at low electron p_{T} electrons from heavy-flavour hadron decays originate predominantly from charm hadrons, while beauty hadron decays dominates above $p_{\mathrm{T}} \sim 4\ \mathrm{GeV}/c$ [74].

2.2.2 Heavy-Flavour Measurements in p–Pb and Pb–Pb collisions

Common observables for studying the QGP were mentioned in Section 1.3, such as elliptic flow, the nuclear modification factor and azimuthal angular correlations. Measurements of these observables are also performed for heavy-flavour particles to better understand the effects from interactions of different particle types with the medium, and due to the aforementioned benefits of using the heavy-flavour quarks to probe the QGP. Recent results from these observables will be discussed in the following.

[3] The following hadronic decay channels, along with their charge conjugates, are studied:
$\mathrm{D}^0 \to \mathrm{K}^-\pi^+$, $\mathrm{D}^+ \to \mathrm{K}^-\pi^+\pi^+$, $\mathrm{D}^{*+} \to \mathrm{D}^0\pi^+ \to \mathrm{K}^-\pi^+\pi^+$.

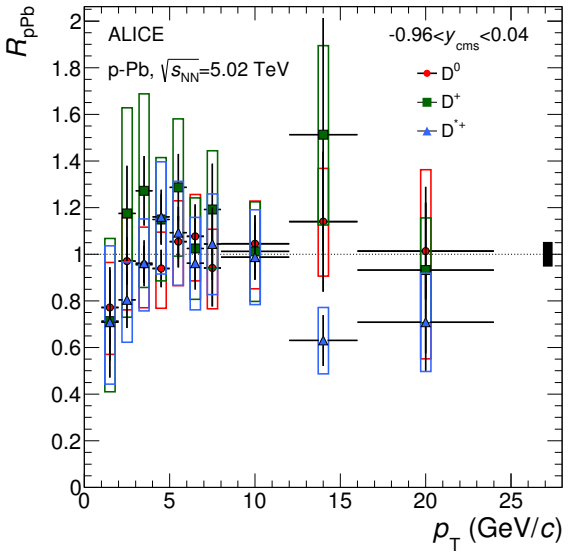

Figure 2.4: The nuclear modification factor, R_{pA}, of prompt D mesons measured by ALICE in p–Pb collisions at $\sqrt{s_{\mathrm{NN}}} = 5.02\,\mathrm{TeV}$, found to be compatible with unity within experimental uncertainties over the full p_{T} interval. Figure from [80].

Nuclear Modification of Heavy-Flavour Mesons

The production cross section of the prompt charmed mesons, D^0, D^+ and D^{*+}, has been measured by ALICE in p–Pb collisions at $\sqrt{s_{\mathrm{NN}}} = 5.02\,\mathrm{TeV}$, by reconstructing their hadronic decays [80]. The measurements were used to calculate the nuclear modification factor, R_{pA}, of these mesons, as seen in Figure 2.4. The R_{pA} was found to be compatible with unity within experimental uncertainties over the full p_{T} interval covered by the measurements [80]. The weighted averaged R_{pA} of the three mesons, as well as the R_{pA} of only the D^0 meson were compared with various theoretical calculations. In Figure 2.5 (left), a comparison with models including only CNM effects are displayed, where three of the four calculations were found to describe the data for the full p_{T} range, while the last one (Kang et al.) has a different trend than the others, and deviates from the data at p_{T} < 3-4 GeV/c. The CNM effects are expected to be largest at low p_{T} where the predictions of the models also differ [80]. The data was also compared to two transport model calculations, as seen in Figure 2.5 (right), which both assume that a small size QGP is formed in p–Pb collisions, and are based on the Langevin approach for the transport of heavy quarks through an ex-

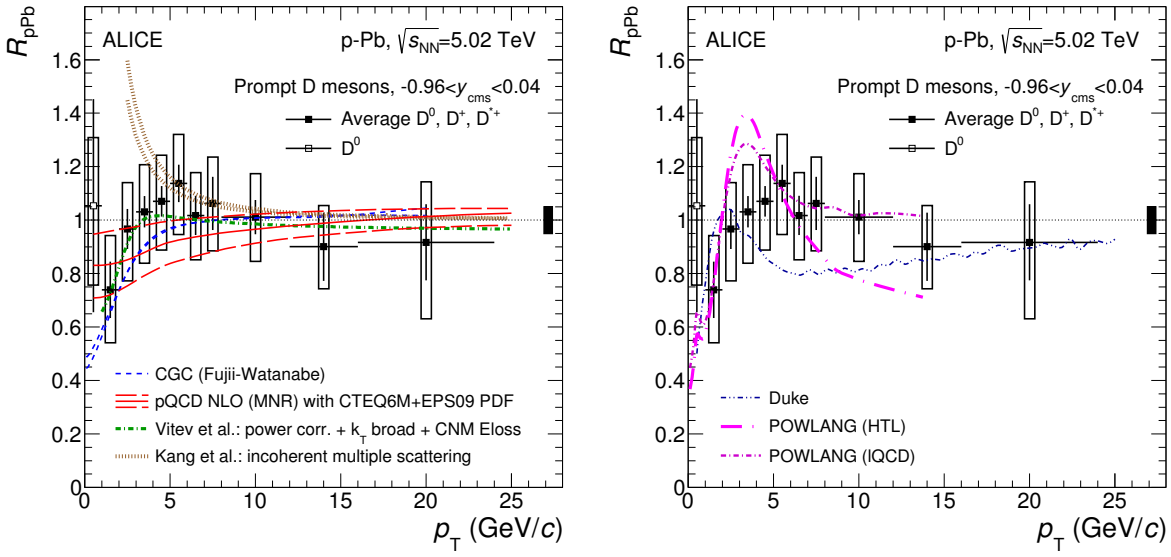

Figure 2.5: The prompt D meson R_{pA} (average of D^0, $\mathrm{D}^+$and D^{*+}) in p–Pb collisions at $\sqrt{s_{\mathrm{NN}}} = 5.02\,\mathrm{TeV}$ measured by ALICE, compared to theoretical models including (left) only Cold Nuclear Matter (CNM) effects, and (right) transport model calculations. Regarding the transport model calculations, the Duke model considers both collisional and radiative energy loss, while POWLANG only considers collisional processes, evaluating two choices for the transport coefficient. Figure from [80].

panding deconfined medium described by relativistic viscous hydrodynamics [80]. The R_{pA} was found to display a structure with a maximum at $p_{\mathrm{T}} \simeq 2.5\mathrm{GeV}/c$ in both approaches, followed by indications of a moderate (< 20-30%) suppression at higher p_{T}, resulting from the interplay of CNM effects and interactions of charm quarks with the radially expanding medium. Due to the large uncertainty of the measured R_{pA}, a discrimination between the models considering only CNM effects and those who also consider hot medium effects, can not be made, even though the data seem to disfavor a suppression larger than 15-20% in the interval $5 < p_{\mathrm{T}} < 10\ \mathrm{GeV}/c$ [80].

In Pb–Pb collisions at $\sqrt{s_{\mathrm{NN}}} = 2.76\,\mathrm{TeV}$, the R_{AA} was calculated for the prompt charmed heavy-flavour mesons, D^0, D^+ and D^{*+}, by measuring the production yields and comparing these to results from pp collisions [64]. The results of these calculations are seen in Figure 2.6 for the centrality classes 0-10% and 30-50%. A maximum suppression of a factor 5-6 compared to the binary-scaled pp yields was observed for the most central collisions at $p_{\mathrm{T}} \sim 10\ \mathrm{GeV}/c$, followed by a persistent suppres-

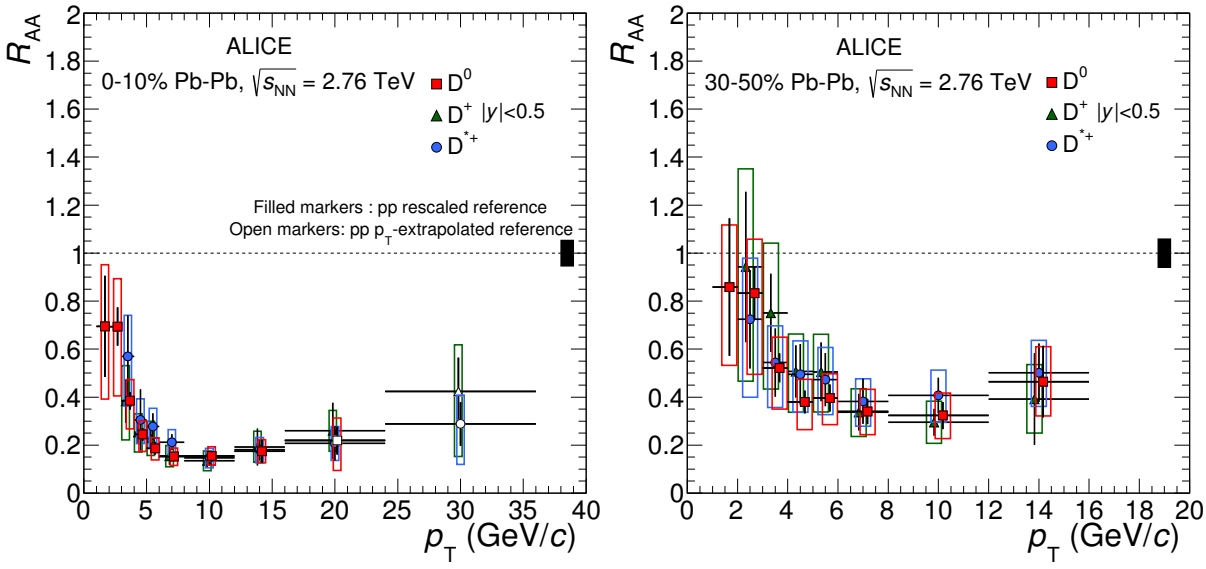

Figure 2.6: Nuclear modification, R_{AA}, of prompt D mesons measured by ALICE in Pb–Pb collisions at $\sqrt{s_{\mathrm{NN}}} = 2.76\,\mathrm{TeV}$ in (left) central and (right) semi-central collisions. A stronger suppression is observed in the more central collisions. Figure from [64].

sion factor of 2-3 at the highest p_{T} covered by the measurements [64]. A consistently lower suppression (higher R_{AA}) is observed for the centrality class 30-50%. For both centrality classes, the weighted average of the D meson R_{AA} were compared to a wide selection of model predictions[4], as seen in Figure 2.7. The models *Djordjevic* [83], *WHDG* [84–86], *CUJET3.0* [87, 88], *MC@sHQ+EPOS* [89], *BAMPS* [90–92], and *Cao, Qin, Bass* [93] considers both radiative and collisional energy loss, while only collisional energy loss is considered for *POWLANG* [94, 95], *TAMU elastic* [96] and *PHSD* [97] [64]. *Vitev* [98] considers two scenarios, one including only radiative energy loss (*Vitev rad*) and the other also including dissociation of heavy-flavour hadrons (*Vitev rad+dissoc*). The medium is described using an underlying hydrodynamical model in *CUJET3.0*, *Cao, Qin, Bass*, *MC@sHQ+EPOS*, *BAMPS*, *POWLANG*, *TAMU elastic* and *PHSD*, while *Djordjevic*, *WHDG* and *Vitev* use a Glauber model nuclear overlap without radial expansion. The initial heavy-quark p_{T} distributions are based on NLO or FONLL pQCD calculations in all model calculations, except for *Cao, Qin, Bass*, which uses the PYTHIA event generator [64]. Several models describe the meas-

[4] For concise summary of the models, please refer to [64], or the more elaborate description in the recent review of the models found at [65].

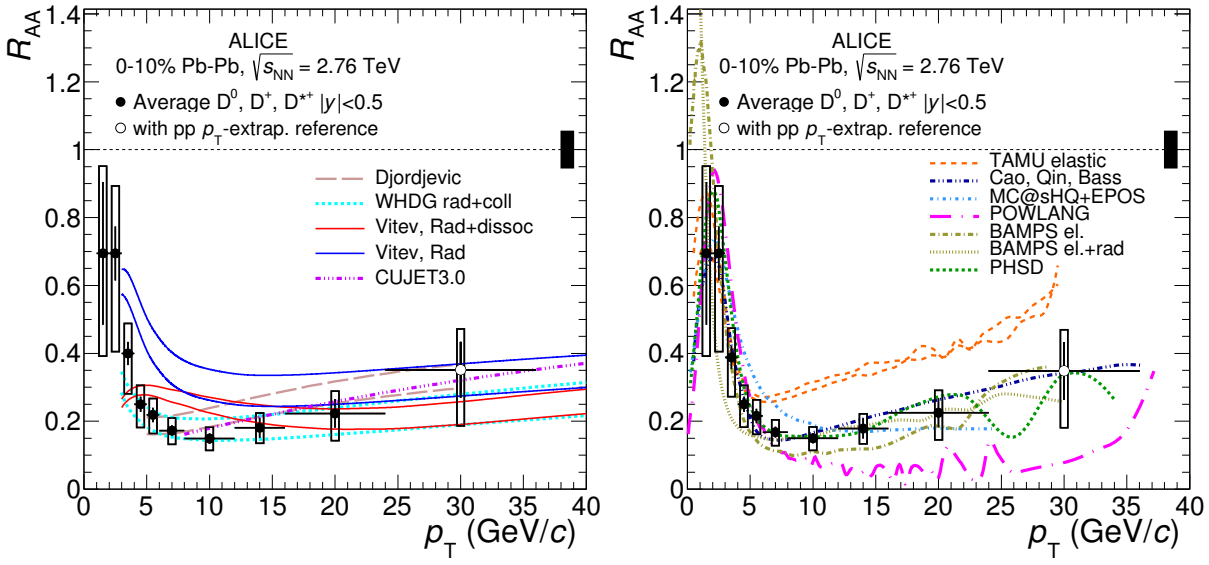

Figure 2.7: Comparison of the prompt D-meson R_{AA} (average of D^0, $\mathrm{D}^+$and D^{*+}) in Pb–Pb collisions at $\sqrt{s_{\mathrm{NN}}} = 2.76\,\mathrm{TeV}$ in the 0-10% centrality class, compared to theoretical predictions. Several of the models describe the measurements well. Some models are shown by two lines to represent their uncertainties. Figure from [64].

urements well. The *TAMU elastic* model was found to overestimate the R_{AA} in central collisions for $6 < p_{\mathrm{T}} < 30$ GeV/c, and *POWLANG* underestimates the R_{AA} in the interval $5 < p_{\mathrm{T}} < 36$ GeV/c for central collisions, despite these models providing a fair description of the D-meson v_2 measured at LHC [99], as seen in the following section, and of the D-meson R_{AA} measured at RHIC [100] [64].

As mentioned in Section 2.1, the colour-charge and quark-mass dependence of the energy loss can be tested by a comparison of the D-meson and pion R_{AA}. A comparison of the D-meson weighted average R_{AA} with the pion R_{AA} at $p_{\mathrm{T}} < 20$ GeV/c and charged particles at $16 < p_{\mathrm{T}} < 40$ GeV/c is seen in Figure 2.8 (left). The R_{AA} of D-mesons was observed to be higher (less suppressed) than that of the pions in the interval $1 < p_{\mathrm{T}} < 6$ GeV/c, although consistent within uncertainties [64]. The R_{AA} of D-mesons, pions and hadrons was found to be compatible in the interval $8 < p_{\mathrm{T}} < 36$ GeV/c [64]. A comparison of the pion and charged particle R_{AA} with models prediction is seen in Figure 2.8 (right), where the *CUJET 3.0*, *Djordjevic* and *Vitev rad* models provide reasonable descriptions of the measurements, while *WHDG* generally underestimates the R_{AA} values compared to data [64].

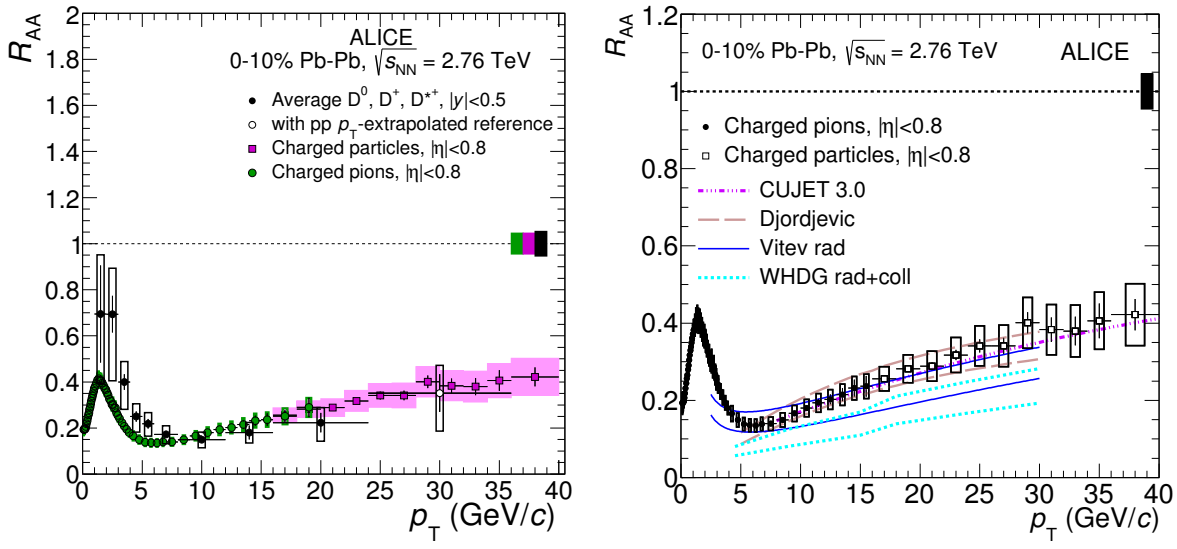

Figure 2.8: Nuclear modification factors, R_{AA}, of pions [81] and charged particles [82] as a function of p_{T}, in the 0-10% centrality class, measured in Pb–Pb collisions at $\sqrt{s_{\mathrm{NN}}} = 2.76\,\mathrm{TeV}$ by the ALICE detector [64]. The measurements are compared to (left) the prompt D-meson R_{AA} (average of D^0, D^+ and D^{*+}), and (right) model predictions which also predict the D-meson R_{AA} (see Figure 2.7). Statistical (bars), systematic (empty boxes), and normalization (shaded box at R_{AA} = 1) uncertainties are shown. Figure from [64].

Finally, a comparison of the D-meson weighted average R_{AA} for p–Pb collisions with that of Pb–Pb collisions in the 0-10% and 30-50% centrality classes is presented in Figure 2.9. The production of heavy-flavour in p–Pb collisions at ALICE is compatible with unity within the uncertainties for the full p_{T} range, suggesting that production scales with the binary number of collisions. This indicates that the suppression of heavy-flavour production observed in Pb–Pb collisions is of different origin than cold nuclear matter effects [80].

Elliptic Flow of Heavy-Flavour Mesons

The measurement of elliptic flow for heavy-flavour mesons provides information on the transport properties of the medium. At low p_{T} the elliptic flow of charmed hadrons allows to investigate if heavy-flavour quarks participate in the collective expan-

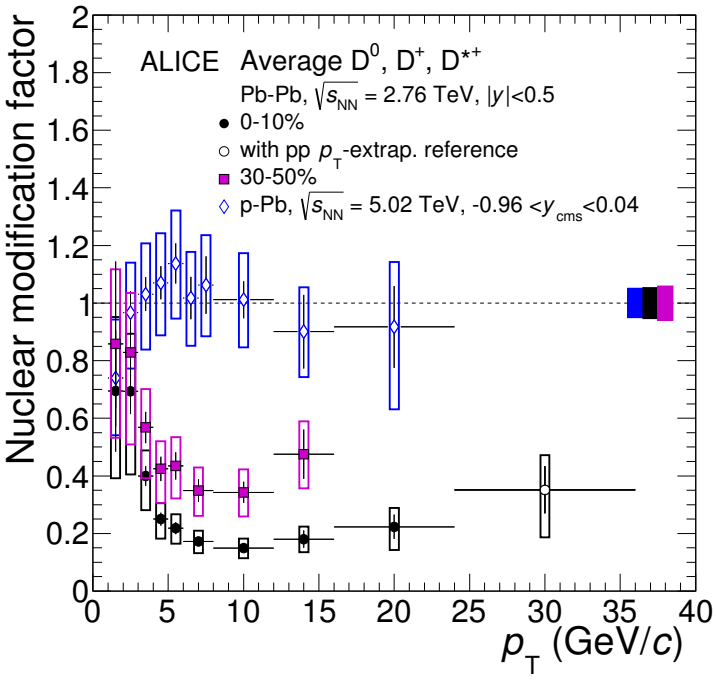

Figure 2.9: Comparison of the prompt D-meson $R_{\rm AA}$(average of $\rm D^0$, $\rm D^+$and $\rm D^{*+}$) as a function of $p_{\rm T}$ in Pb–Pb collisions at $\sqrt{s_{\rm NN}} = 2.76\,\rm TeV$ in the 0-10% and 30-50% centrality classes, compared to the $R_{\rm pA}$ measured in p–Pb collisions at $\sqrt{s_{\rm NN}} = 5.02\,\rm TeV$ [101] [64]. The $R_{\rm pA}$ is compatible with unity within uncertainties, indicating that the suppression seen in $R_{\rm AA}$ is of different origin than Cold Nuclear Matter (CNM) effects.

sion of the QGP, and if they are subject to thermalization in the medium [103, 104] [102]. Heavy-flavour quarks should not thermalize in the medium at high momentum, and thus should not acquire the large elliptic flow induced by collective pressure effects [105]. Instead, their azimuthal anisotropy in non-central collisions are expected to mainly be determined by the path length dependence of parton energy loss in the geometrically-asymmetric dense medium [105]. The restraints to the path-length dependence of the parton energy loss set by v_2 measurements at high $p_{\rm T}$ complements the measurement of the $R_{\rm AA}$ [102].

The elliptic flow, v_2, of heavy-flavour mesons has been measured by ALICE in Pb–Pb collisions at $\sqrt{s_{\rm NN}} = 5.02\,\rm TeV$ [99,102]. The results for the weighted average of $\rm D^0$, $\rm D^+$ and $\rm D^{*+}$, in addition to the v_2 of charged particles (dominated by light-flavour

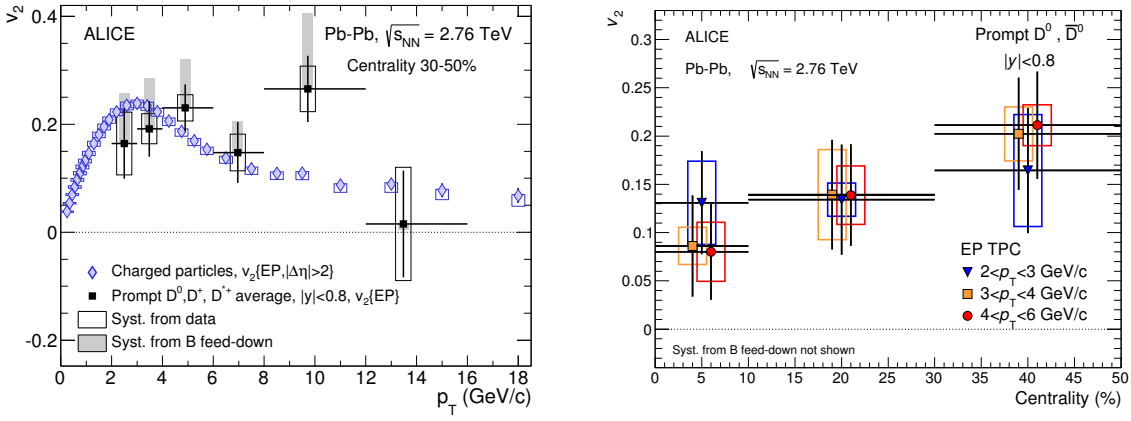

Figure 2.10: (Left) Prompt D-meson v_2 (average of D^0, $\mathrm{D}^+$and D^{*+}) as a function of p_T, compared to the charged particle v_2, in Pb–Pb collisions at $\sqrt{s_\mathrm{NN}} = 5.02\,\mathrm{TeV}$ in the 30-50% centrality class, measured with the event plane (EP) method [102]. (Right) D^0 v_2 measured in three p_T regions as a function of centrality [99]. The points for two of the p_T intervals are displaced horizontally for increased visibility.

hadrons), is seen in Figure 2.10 (left) for the 30-50% centrality class [102]. The results of the two measurements were found to be compatible in magnitude, and the average D-meson v_2 value in the interval $2 < p_\mathrm{T} < 6\ \mathrm{GeV}/c$ was found to be larger than zero with a significance of 5.7 σ, indicating that the low momentum charm quarks take part in the collective motion of the system [102]. Though the uncertainties are too large to draw a conclusion, positive values of v_2 are also observed for $p_\mathrm{T} > 6\ \mathrm{GeV}/c$, likely to be caused by the path-length dependence of the partonic energy loss [102]. As expected from the decreasing initial geometric anisotropy towards more central collisions, the v_2 of D^0 mesons in Figure 2.10 (right) is seen to increase towards less central collisions (higher centralities) [99]. A comparison of the weighted average of the prompt charmed D-meson v_2 to theoretical predictions is displayed in Figure 2.11. The anisotropy was found to be qualitatively described by the models that include both charm quark energy loss in a geometrically anisotropic medium and mechanisms that transfer to charm quarks the elliptic flow induced during the system expansion [99]. These mechanisms include collisional processes (*MC@sHQ+EPOS*, *Coll+Rad(LPM)*, *BAMPS*) and resonance scattering with hadronization via recombination (*TAMU elastic*, *UrQMD*) in a hydrodynamically expanding QGP [99].

Reviewing the results from comparisons of measurements and theoretical predic-

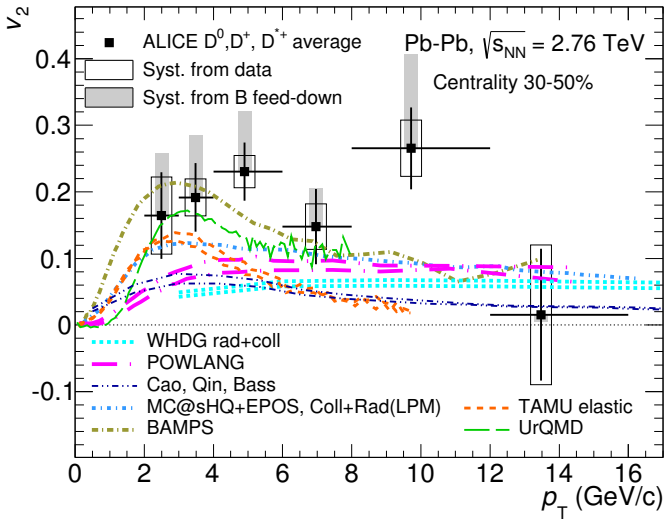

Figure 2.11: Comparison of the prompt D-meson v_2 (average of D^0, D^+ and D^{*+}) in Pb–Pb collisions at $\sqrt{s_{\mathrm{NN}}} = 2.76\,\mathrm{TeV}$ in the 30-50% centrality class, compared to various models. A qualitative description of the data is seen from the models *MC@sHQ+EPOS*, *Coll+Rad(LPM)*, *BAMPS*, *TAMU elastic* and *UrQMD* [99]. The models *WHDG rad+coll*, *POWLANG* and *Cao, Qin, Bass*, which either do not include collective expansion of the medium, or lack a contribution to the hadronization via recombination with light quarks from the medium, in general predict a smaller anisotropy than observed in data [99]. A more descriptive summary of the models can be found in [99].

tions in R_{AA} and v_2, shown in Figure 2.7 and Figure 2.11, respectively, shows that it is challenging to describe both observables at the same time. In general, the models with accurate descriptions of R_{AA} tend to underestimate v_2, and the models which describe v_2 well tend to underestimate the measured R_{AA} at high p_{T} [99].

As the heavy-flavour quarks are produced in the very first moments of the collision, before the azimuthal anisotropy is reduced by expansion of the medium, partons emitted in the direction of the reaction plane [5] (in-plane) have a shorter in-medium path length than partons emitted orthogonally (out-of-plane), leading to a stronger high-p_{T} suppression in the out-of-plane case [102]. The anisotropy was measured

[5] The reaction plane is spanned by the z-axis (beam direction) and x-axis (direction of impact parameter), see Figure 1.5.

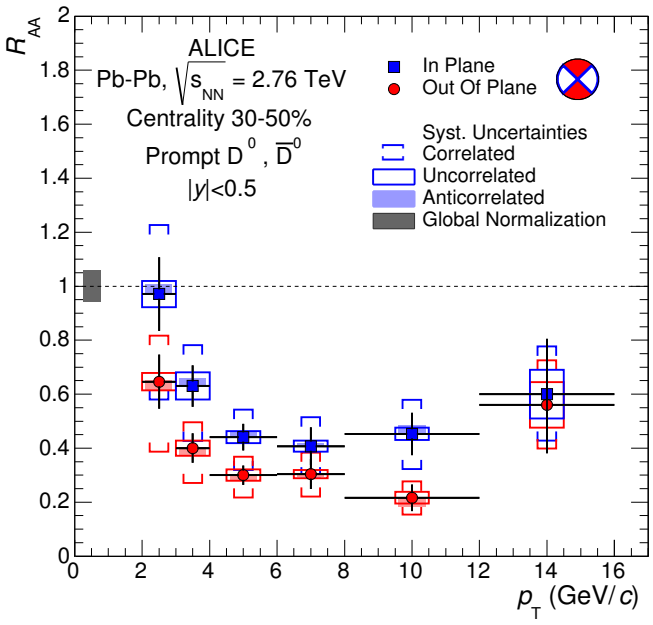

Figure 2.12: Nuclear modification factor, R_{AA}, of D^0 mesons measured in Pb–Pb collisions at $\sqrt{s_{\mathrm{NN}}} = 2.76\,\mathrm{TeV}$ by ALICE in the 30-50% centrality class in two 90°-wide intervals centred on the in-plane and on the out-of-plane directions with respect to the event plane [99]. A large suppression is observed in both directions for p_{T} >4GeV/c. Overall, a stronger suppression is observed in the out-of-plane direction. Figure from [99].

for the D^0 meson R_{AA} in the in-plane and out-of-plane directions of the event plane, as seen in Figure 2.12. A large suppression is observed in both scenarios for $p_{\mathrm{T}} > 4\mathrm{GeV}/c$, with an overall larger suppression in the out-of-plane direction, where the average path length of heavy quarks through the medium is larger [99], indicating a path length dependence on the heavy-quark energy loss.

2.3 Heavy-Flavour Correlations

The measurement of the heavy-flavour R_{AA}, v_2 and differential production cross section provide important information of the production of heavy quarks and how they are modified in a QCD medium, but they do not provide any information on the indi-

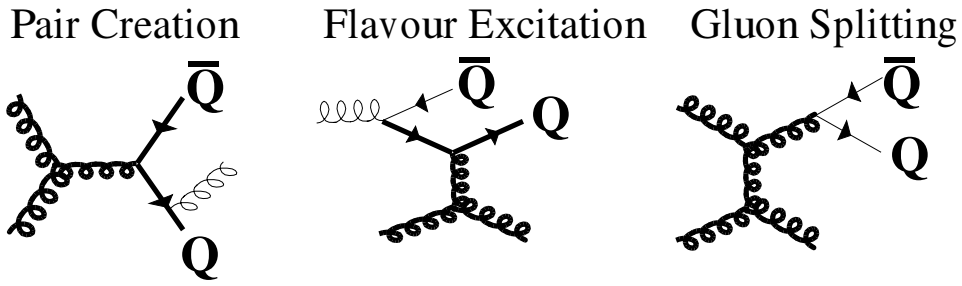

Figure 2.13: Examples of pair creation, flavour excitation and gluon splitting. The thick lines correspond to the hard process, the thin ones to the parton shower. Figure and caption from [106].

vidual production processes of the heavy quarks and the interplay between them [18]. Measuring azimuthal angular correlations in addition to the R_{AA} and v_2, makes it possible to discriminate between collisional and radiative energy loss, and to learn more about the production mechanisms of heavy-flavour quarks. Heavy-flavour quarks are produced through several QCD mechanisms involving quarks and gluons, which, for leading-order processes, are divided into the three categories *pair production*, *flavour excitation* and *gluon splitting*, illustrated by the diagrams in Figure 2.13. The contributions of the various production mechanisms is expected to vary with the centre-of-mass energy of the collision [107], and the resulting kinematical spectra of the quark emission varies significantly, especially in $\Delta\varphi$. Pair production is a leading order (LO) mechanism, illustrated in Figure 2.13 (left), which takes place through gluon fusing ($gg \rightarrow Q\bar{Q}$). The quark-antiquark pair is predominantly emitted back-to-back in azimuth, resulting in an azimuthal angular correlation with a peak at $\Delta\varphi = \pi$ (away-side), as the trigger particle is by definition at $\Delta\varphi = 0$ (near-side). In the case of flavour excitation, a NLO process seen in Figure 2.13 (middle), an incoming quark from one beam particle[6] is scattered against a parton of the other beam, i.e., $Qq \rightarrow Qq$ or $Qg \rightarrow Qg$ [107], characterized by having only one heavy quark in the final state [106]. Gluon splitting, a NLO process illustrated in Figure 2.13 (right), involves no heavy quark in the hard scattering, but a $Q\bar{Q}$ pair is produced in the initial or final-state showers from a $g \rightarrow Q\bar{Q}$ branching [106].

A Monte Carlo simulation has been performed [106] where the PYTHIA event generator parameters have been tuned to reproduce NLO pQCD predictions for $\mathrm{c\bar{c}}$ and $\mathrm{b\bar{b}}$ quark pair kinematics in Pb–Pb collisions at $\sqrt{s_{\mathrm{NN}}} = 5.02\,\mathrm{TeV}$, resulting from the pro-

[6] In the case where Q is not a valence flavour, it comes from a $q \rightarrow Q\bar{Q}$ process [107].

duction mechanisms already mentioned. The predicted transverse momentum, p_{T}, and the difference in azimuthal angle between the two quarks, $\Delta\varphi$, are presented in Figure 2.14 for $\mathrm{c\bar{c}}$ pairs (upper row) and $\mathrm{b\bar{b}}$ pairs (lower row). The different production mechanism contributions are seen in both the p_{T} distribution and azimuthal angular distributions. Pair production shows a distinct away side peak in $\Delta\varphi$, while the two NLO processes are more evenly distributed, and show little preference for specific $\Delta\varphi$ regions. The spectra obtained from correlation studies in pp collisions can be fitted in order to learn more about the interplay of the various production mechanisms, and thus provide constraints to pQCD models [18] (see Section 2.3.1). The PYTHIA simulation has also been compared to NLO predictions from MNR [108] calculations, seen as triangles in Figure 2.14. A reasonable agreement is found for the predictions of the p_{T} distributions and for $\Delta\varphi_{\mathrm{b\bar{b}}}$, despite a difference in the magnitude of the away side $\Delta\varphi$ peak, while significant discrepancies are seen for the $\Delta\varphi_{\mathrm{c\bar{c}}}$ distribution [106] .

As the quarks are bound in hadronic states, their kinematics can not be directly accessed, but have to be studied through observables involving their hadronic states [109]. Heavy-flavour correlations are performed by selecting a trigger particle and an associated particle following certain selection criteria, and correlate these, as discussed briefly in Section 1.3.3. D mesons are the lightest charmed hadrons, have a close relation to the initial $q\bar{q}$ pair and high hadronization branching ratios (BR) from charm and beauty, ($c \rightarrow \mathrm{D}^0 + X$, BR = 56.5 $\pm$ 3.2 %) and ($b \rightarrow \mathrm{B}^-/\overline{\mathrm{B}}^0/\overline{\mathrm{B}}_{\mathrm{S}}^0 \rightarrow \mathrm{D}^0 + X$, BR = 59.6 $\pm$ 2.9 % [11]), respectively, making them suitable for correlation studies. D-D correlations have thus been suggested as a method to discriminate the different contributions to energy loss, e.g., radiative and collisional [110, 111]. Though correlations between two D mesons is ideal in order to study the energy loss in the QGP, it is statistically challenging due to the low production cross section and small branching ratio to decay channels suitable for reconstruction, combined with challenges related to the reconstruction of D mesons in the experiment. An alternative strategy is to select associated particles further down the decay chain, and correlate these with the D meson trigger, increasing the statistics by using less stringent selection procedures. Examples of $\mathrm{c\bar{c}}$ and $\mathrm{b\bar{b}}$ fragmentation processes can be seen in Figure 2.15, displaying some of the options for particles close to the original back-to-back partons, which can be studied.

The focus of this thesis is D^0- HFE correlations, i.e., correlations where the trigger particle is required to be a D^0 meson, and the associated particle is an electron originating from a heavy-flavour decay (HF electron (HFE)). The decay $\overline{D}^0 \rightarrow K^+ + e^- + \bar{\nu}_e$ is seen in Figure 2.15 (left), yielding a HF electron in the direction of the recoiling

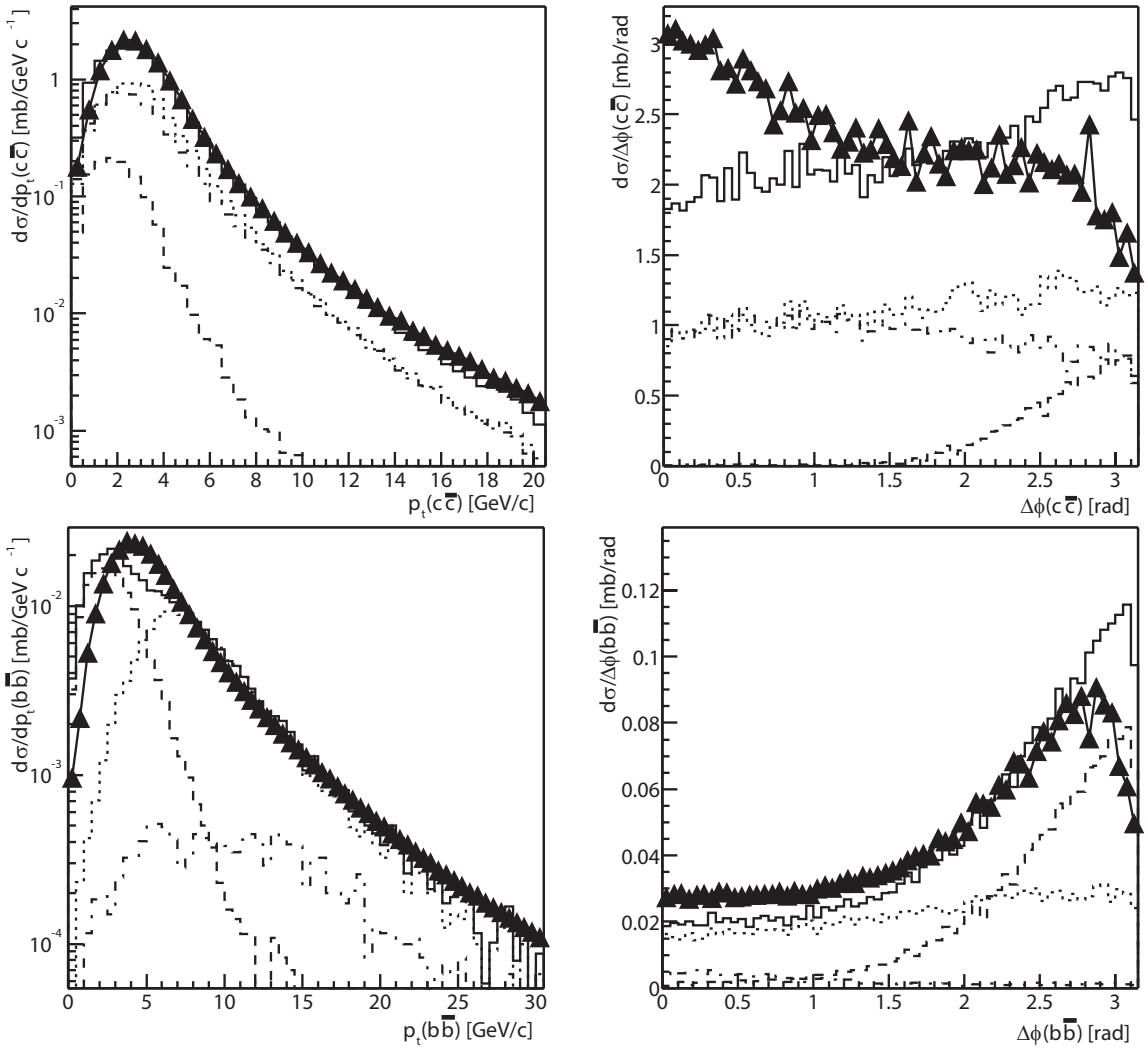

Figure 2.14: Comparison between charm (upper) and beauty (lower) production as a function of p_{T} (left) and $\Delta\varphi$ (right) in NLO calculations by Mangano, Nason and Ridolfi (MNR) and in PYTHIA with parameters tuned to reproduce NLO pQCD predictions for Pb–Pb collisions at $\sqrt{s_{\mathrm{NN}}} = 5.5\,\mathrm{TeV}$. The triangles represent MNR, while the solid line corresponds to PYTHIA. The individual PYTHIA contributions are pair productions (dashed), flavour excitation (dotted) and gluon splitting (dot-dashed). Figure and modified caption from [106].

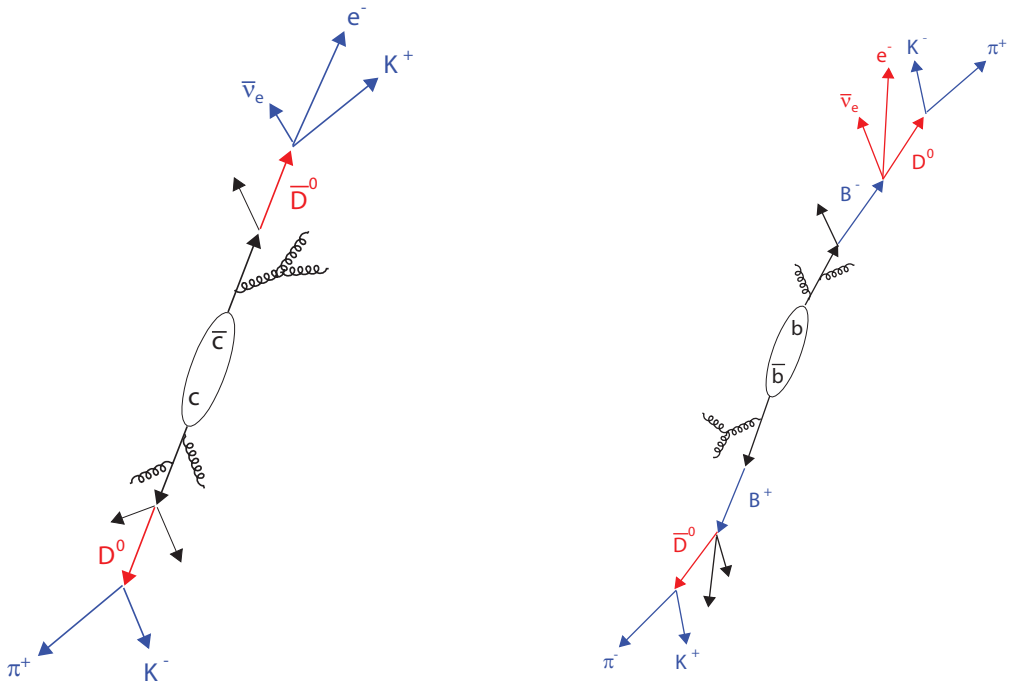

Figure 2.15: Schematic representation of decay topology of a $c\bar{c}$ quark pair (left) and a $b\bar{b}$ pair (right), branching into D^0 mesons. Figure from [112].

$\overline{D^0}$. The away side peak from the electron will be somewhat blurred from the decay kinematics, but still preserves much of the information of the original back-to-back $c\bar{c}$ pair. D^0 mesons can also originate from B meson decays (these are referred to as *feed-down* D^0 mesons), as seen in Figure 2.15. One of the aims of the D-e correlation analysis is to separate the contributions from b and c. The HFE sample in the D-e correlation analysis needs to have a high purity, and contaminations from hadrons and non-HF electrons must be removed in order to get precise results. A high purity comes at the price of a reduced selection efficiency, and a large amount of data is required to perform the analysis with significant results. The correlations of D^0 mesons with electrons will be discussed in detail in Chapter 5. The selection of D^0 mesons is presented in Section 4.2, while the electron selection is discussed in Section 4.3.

A less strict selection is used in D-h correlations, where the trigger particle is required to be a D meson, and the associated particle is any charged hadron, increasing the statistics substantially. A near-side peak at $(\Delta\eta, \Delta\varphi) = (0, 0)$, originates from the jet containing the trigger D meson, and an away-side peak extending over a wide

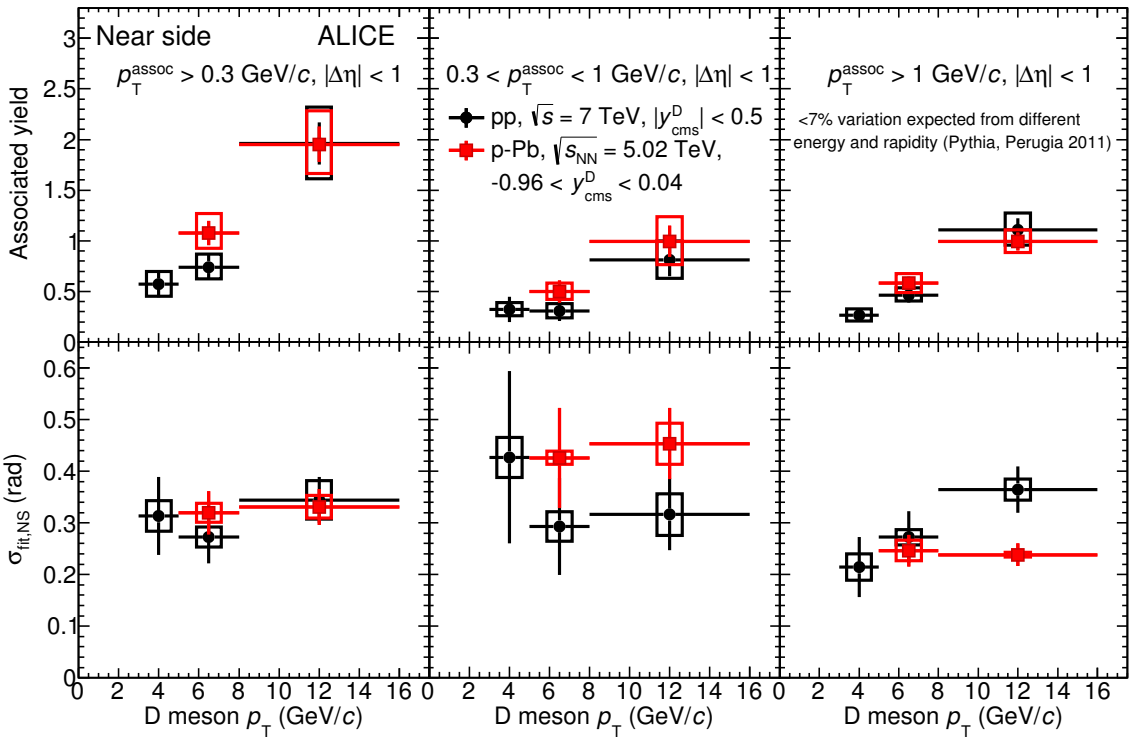

Figure 2.16: Comparison of the near-side peak associated yield (top row) and peak width (bottom row) of D-h correlations in pp and p–Pb collisions as a function of $p_{\mathrm{T}}^{\mathrm{D}^0}$, for $p_{\mathrm{T}}^{\mathrm{assoc}} > 0.3\ \mathrm{GeV}/c$ (left column), $0.3 < p_{\mathrm{T}}^{\mathrm{assoc}} < 1\ \mathrm{GeV}/c$ (middle column), and $p_{\mathrm{T}}^{\mathrm{assoc}} > 1\ \mathrm{GeV}/c$ (right column). Statistical and systematic uncertainties are shown as error bars and boxes, respectively. Figure and caption from [113]

range in $\Delta\eta$ is generated by the recoiling jet [113]. Measurements of D-h correlations were performed recently at ALICE in pp collisions at $\sqrt{s} = 7\,\mathrm{TeV}$ and p–Pb collisions at $\sqrt{s_{\mathrm{NN}}} = 5.02\,\mathrm{TeV}$, laying an important foundation for measurements of possible modifications of D-h correlations in Pb–Pb collisions, which can provide information on charm-quark energy-loss mechanisms in the QGP [113]. A quantitative comparison of the results in the pp and p–Pb collision systems was performed by fitting the azimuthal angular correlation distributions by a double Gaussian distribution, in addition to a constant baseline term describing the physical minimum of the $\Delta\varphi$ distribution[7]. The extracted values of the baseline subtracted integrals (associated yield)

[7] The fitting function and extraction procedure of the associated yield and sigma is discussed in Section 5.1.5.

and widths (sigma) of the near side peak are seen in Figure 2.16 for various p_{T} intervals of the trigger and associated particle. The near-side peak associated yield, seen in the upper panels of the figure, was observed to have an increasing trend with increasing D meson p_{T}, and to have similar values, within uncertainties, for the softer (0.3 < $p_{\mathrm{T}}^{\mathrm{assoc}}$ < 1 GeV/c) and harder ($p_{\mathrm{T}}^{\mathrm{assoc}}$ > 1 GeV/c) sub-ranges of the associated particle p_{T} [113]. A compatibility within uncertainties between the results from pp collisions at $\sqrt{s} = 7\,\mathrm{TeV}$ and p–Pb collisions at $\sqrt{s_{\mathrm{NN}}} = 5.02\,\mathrm{TeV}$ was also observed, indicating that no modifications of the near-side peak due to cold nuclear matter effects were present with the current level of statistics [114]. The width of the near-side Gaussian term ($\sigma_{\mathrm{fit,NS}}$), seen in the lower panels of Figure 2.16, was not found to not have a strong dependence on the D-meson p_{T} in the range of the measurements in the full p_{T} range of the associated particle ($p_{\mathrm{T}}^{\mathrm{assoc}}$ > 0.3 GeV/c), while no quantification of the dependence of $\sigma_{\mathrm{fit,NS}}$ on D meson and associated particle p_{T}, as well as a possible difference between the values measured for pp and p–Pb collisions could be made, due to the current level of uncertainty in the measurements [113].

Correlation distributions using electrons from semi-leptonic heavy-flavour decays as trigger particles, and charged hadrons as associated particles (e-h), have been studied at RHIC [115] and ALICE [116]. The results can be used to discriminate between beauty and charm production, based on the differences in the near-side peak width resulting from the different decay kinematics of charm and beauty quarks.

2.3.1 Separation of Charm and Beauty Contributions

The production of $\mathrm{c\bar{c}}$ and $\mathrm{b\bar{b}}$ pairs result in different kinematical distributions, as already discussed, and seen in Figure 2.14, and thus it is necessary to separate the contributions from charm and beauty to fully understand the production and energy loss mechanisms. Charm quarks hadronize predominately directly to D^0 mesons ($c \rightarrow \mathrm{D}^0 + X$, BR = 56.5 $\pm$ 3.2 %) [11], while beauty quarks produce D^0 via an intermediate B meson ($b \rightarrow \mathrm{B}^-/\overline{\mathrm{B}}^0/\overline{\mathrm{B}}_{\mathrm{S}}^0 \rightarrow \mathrm{D}^0 + X$, BR = 59.6 $\pm$ 2.9 %) [11], and the branching ratio from charm and beauty to electrons is 9.6% and 10.68%, respectively [112]. The relatively high branching ratios for for both charm and beauty into D^0, and for D^0 into electrons, makes D^0-e correlations suitable for studies aiming to separate the contributions by means of azimuthal angular correlations.

In the following, the well established method for separating the charm and beauty contribution by shape fitting the near-side $\Delta\varphi$ peak will be discussed, in addition to a separation method exploiting the charge-sign of the D^0 meson decay daughters. Both of these methods separate the contributions on a statistical basis.

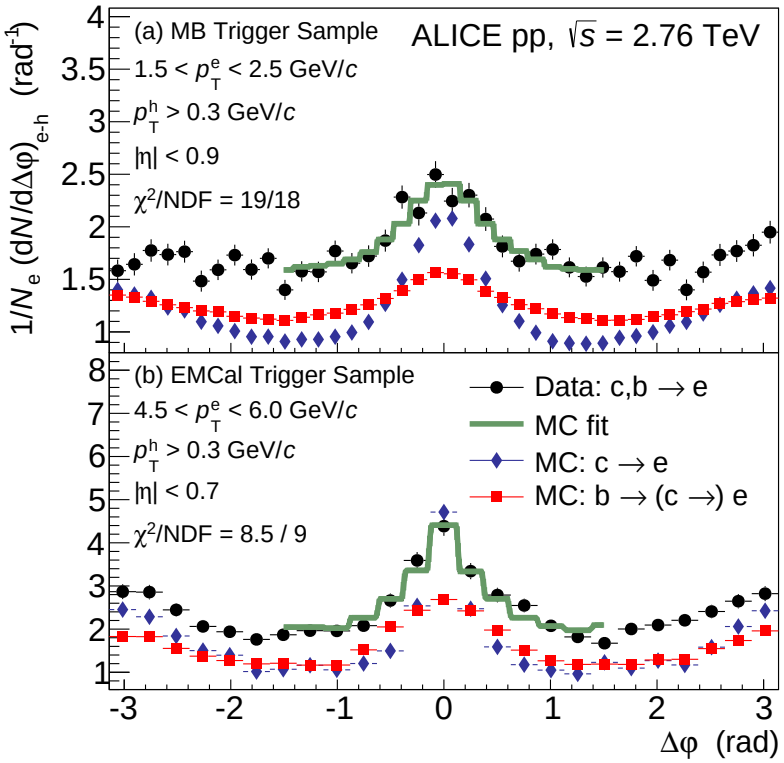

Figure 2.17: Azimuthal angular correlation distribution of electron-hadron correlations measured in pp collisions at $\sqrt{s} = 2.76\,\mathrm{TeV}$ by ALICE, in the trigger (electron) p_{T} interval (top panel) 1.5 < p_{T} < 2.5 GeV/c and (bottom panel) 4.5 < p_{T} < 6.0 GeV/c, for associated (hadron) p_{T} > 0.3 GeV/c. The distribution is fitted to PYTHIA templates describing the separate contributions of charm (red squares) and beauty (blue diamonds) origin, in addition to the combined contribution (green line). The width of the peaks can be utilized for separating the charm and beauty contributions by the shape-fitting method. Figure from [116].

The shape fitting method is a method for discrimination between the charm and beauty contribution, based on the differences in the width of the near side peak in $\Delta\varphi$ caused by different kinematics in the production and decay of $\mathrm{c\bar{c}}$ and $\mathrm{b\bar{b}}$ pairs. The width of the near side peak is wider for feed-down D-e correlations (originating from $\mathrm{b\bar{b}}$), compared to prompt D-e correlations (originating from $\mathrm{c\bar{c}}$), caused in part

by the larger energy release (Q value) of semi-leptonic B meson decays, which lead to a broad angular correlation between daughter hadrons and electrons [117]. Another contribution adding to the width of correlations of the feed-down contribution is that there are more steps from the initial $\mathrm{b\bar{b}}$ pair to the correlated particles, compared to the $\mathrm{c\bar{c}}$ scenario, as seen in Figure 2.15. The separation of the contributions is performed by fitting the correlation distribution by a template from PYTHIA Monte Carlo simulations, computed for the separate charm and beauty contributions, which combined should match the measured distribution. The shape fitting method in e-h correlations has been employed by the STAR [115] and ALICE [116] experiments. The correlation distribution of e-h pairs in pp collisions at $\sqrt{s} = 7\,\mathrm{TeV}$ measured by ALICE is seen in Figure 2.17, for associated particles in the interval 1.5 <p_{T} <2.5 GeV/c. A wider peak is seen for the distribution originating from beauty quarks. A drawback of this technique is the essential model dependence, as the separation is performed based on a Monte Carlo template [118], and as previously discussed, and shown in Figure 2.14, there are discrepancies between different model predictions, e.g., the calculations by the MNR and PYTHIA models, both shown in the figure.

The charge-sign method relies on the charge sign of the D^0 meson decay daughters, kaons, pions and electrons, for separating the charm and beauty contributions, and was first introduced at the STAR experiment at RHIC [112, 119]. A HFE is defined as the trigger (upper part of Figure 2.15), and is correlated with a D^0 meson in the opposite direction, identified by reconstruction from its kaon and pion daughters (the decays in the lower part of Figure 2.15). In the decays from both charm and beauty, an electron-kaon pair is found in the trigger direction, where the sign of the kaon and electron are opposite (unlike-sign) in the decay originating from charm (left side in the figure), whereas a like-sign pair is seen in the decay from beauty. A PYTHIA simulation predicting the azimuthal angular e-D^0 correlation distributions of $\mathrm{c\bar{c}}$ and $\mathrm{b\bar{b}}$ pairs is seen in Figure 2.18, for like-sign (left) and unlike-sign (right) e-K pairs. By selecting only unlike-sign e-K pairs, B decays can be identified at the away-side, while requiring only like-sign pairs leads to a selection of beauty decays at the near-side and charm decays with a small contribution ($\sim 15\%$) from beauty at the away-side [112].

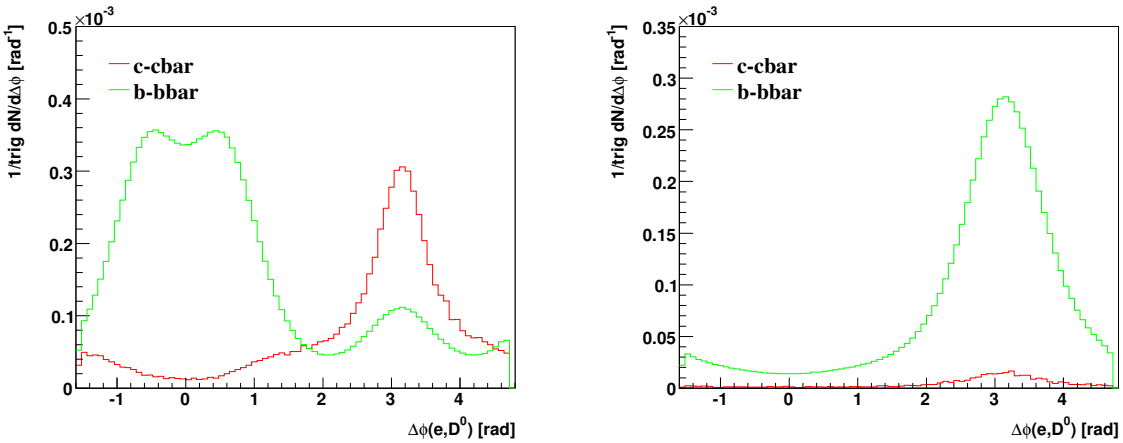

Figure 2.18: Azimuthal angular correlation distributions from PYTHIA Monte Carlo simulations for charm and bottom pairs, for like charge-sign and unlike charge-sign kaon-electron pairs. In the like-sign scenario (left) the near-side peak is dominated by the $\mathrm{b\bar{b}}$ contribution, and the away-side is dominated by the $\mathrm{c\bar{c}}$ contribution. In the unlike-sign (right) case the $\mathrm{b\bar{b}}$ contribution dominates the away-side. Figure from [119].

Chapter 3

Experimental Setup

In this chapter, the experimental setup used for the analysis presented in the thesis will be discussed. The particle beams are accelerated by the Large Hadron Collider (LHC), and are collided at different interaction points along the LHC beamline. One of these collision points is located at the centre of the ALICE detector, which has collected the data studied in this analysis.

3.1 The Large Hadron Collider (LHC)

The Large Hadron Collider is currently the largest and most powerful particle accelerator in the world, situated at the CERN laboratory, at the Franco-Swiss border. The accelerator is located between 45-100 m underground and has a circumference of 26,7 km. It consists of two separate[1] beam pipes with opposite magnetic fields, within a twin-bore magnet design, allowing to accelerate either protons in both directions (pp collisions), lead ions in both directions (Pb–Pb collisions) or protons in one direction and lead ions in the other (p–Pb collisions). The accelerator is designed to deliver collisions at a centre-of-mass energy of $\sqrt{s} = 14\,\mathrm{TeV}$ in pp collisions, and $\sqrt{s_{\mathrm{NN}}} = 5.5\,\mathrm{TeV}$ in Pb–Pb collisions [121]. During the first operational period (Run1) of the LHC, lasting from November 2009 to February 2013, data was collected at centre-of-mass energies of up to $\sqrt{s} = 8\,\mathrm{TeV}$, $\sqrt{s_{\mathrm{NN}}} = 5.02\,\mathrm{TeV}$ and $\sqrt{s_{\mathrm{NN}}} = 2.76\,\mathrm{TeV}$ in the pp, p–Pb, and Pb–Pb collision systems, respectively. After a long, planned shutdown period lasting until the beginning of 2015, the LHC entered into the current run period (Run2),

[1] The beam pipes intersect at the four interaction points where the collisions occur. At these points, the beams share an approximately 130 m long common beampipe [120].

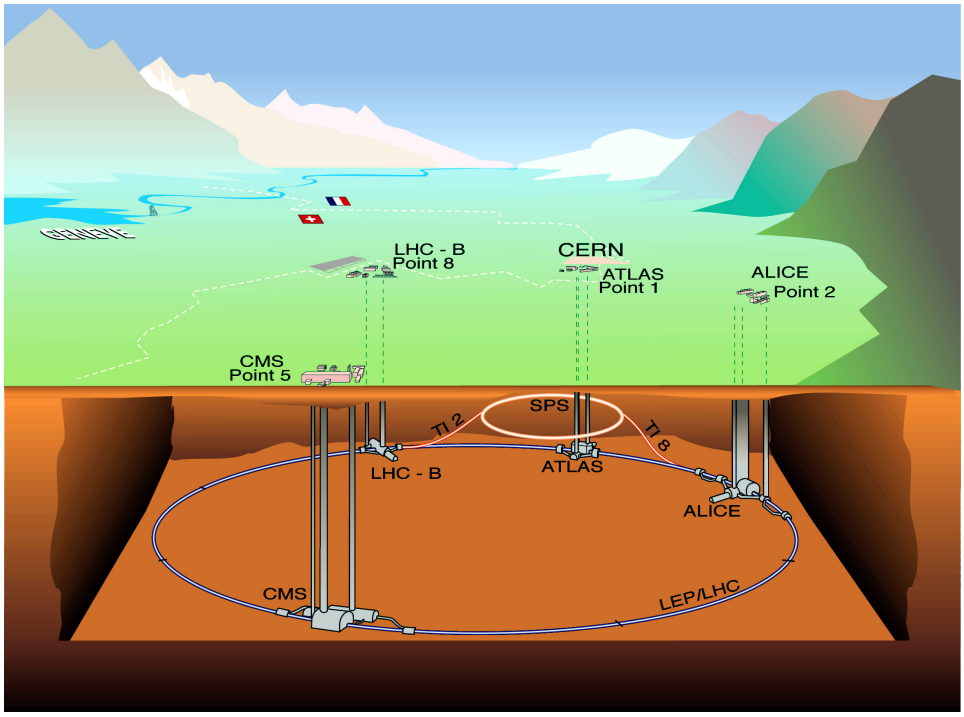

Figure 3.1: Schematic view of the LHC and the four main experiments situated along the accelerator. The dashed white line indicates the boarder between France and Switzerland. Figure from [122].

in which pp collisions up to $\sqrt{s} = 13\,\mathrm{TeV}$, Pb–Pb collisions at $\sqrt{s_{\mathrm{NN}}} = 5.02\,\mathrm{TeV}$, and p–Pb collisions at energies up to $\sqrt{s_{\mathrm{NN}}} = 8.16\,\mathrm{TeV}$ have been performed so far.

Four large experiments are situated along the LHC, namely ALICE, ATLAS, CMS and LHCb, as seen in Figure 3.1. In the figure, the SPS accelerator can also be seen, which is the step preceeding the LHC in the accelerator chain. The ATLAS and CMS are high luminosity, general purpose experiments designed to study a wide variety of physics, with one of the most discussed result so far being that of the Higgs boson discovery, announced in July 2014 [123, 124]. LHCb is a low luminosity experiment designed for precision measurements of CP-violation and rare decays of B hadrons. The last experiment, ALICE, has been used for collecting the data analyzed in this thesis, and will be discussed in more detail in the following section.

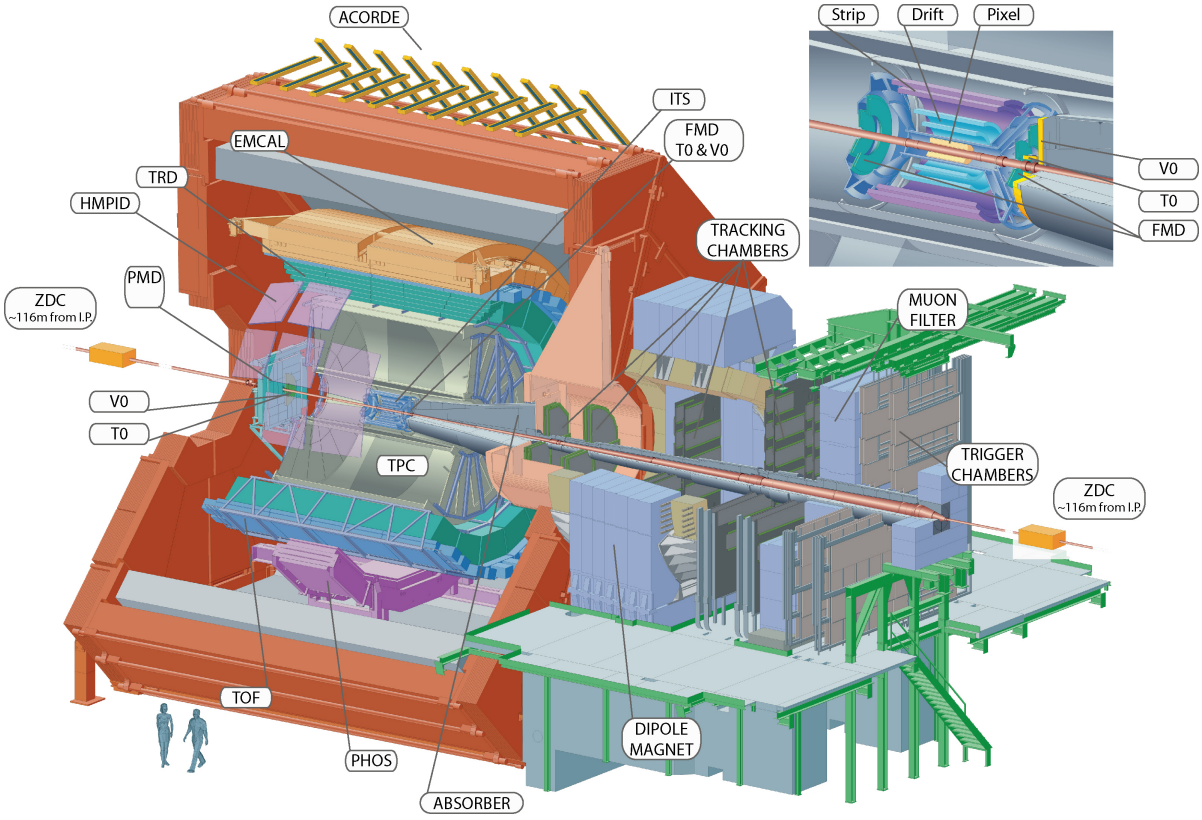

Figure 3.2: Schematic view of the ALICE experiment, showing the various subsystems installed during LHC Run 1. The inlay in the upper right corner provides a closer view of the ITS layer structure.

3.2 A Large Ion Collider Experiment (ALICE)

ALICE is a general-purpose, heavy-ion detector which focuses on QCD studies, designed to address the physics of strongly interacting matter and the Quark-Gluon Plasma (QGP) at extreme values of energy density and temperature in nucleus-nucleus[2] collisions [125]. The experiment has been designed to cope with the extreme particle multiplicity anticipated in Pb–Pb collisions, and its subsystems have been optimized to provide high-momentum resolution as well as excellent PID over

[2] While studies of Pb–Pb collisions is the main purpose of the experiment, ALICE also studies physics in pp and p–Pb collisions. As mentioned previously, measurements in pp and p–Pb provide an essential reference necessary to gain a full understanding of the results from Pb–Pb collisions.

a broad momentum range [125]. As a result, the experiment is able to study a wide range of physic with a p_{T} threshold down to 0.15 GeV/c and good PID capabilities up to 20 GeV/c [126].

A schematic cross-sectional representation of ALICE is seen in Figure 3.2, displaying the various subdetector systems. The subsystems are divided into three categories: central barrel detectors, forward detectors and the muon spectrometer. The central barrel contains the main detectors used for tracking and PID and covers polar angles from 45° to 135° (corresponding to a pseudorapidity, $|\eta| < 0.9$). These detectors are encased in a large solenoid with a magnetic field of 0.5 T, seen as the large, red structure in Figure 3.2. Collisions take place in the centre of the innermost layer (Silicon Pixel Detector (SPD)) of the Inner Tracking System (ITS) detector, and the emerging particles will then pass through the Time Projection Chamber (TPC), Transition Radiation Detector (TRD) and Time Of Flight (TOF) detectors, which cover the complete central barrel in azimuth. The next layer if detectors in the central barrel do not have a full coverage in azimuth, but rather consists of the ElectroMagnetic Calorimeter (EMCal), PHOton Spectrometer (PHOS) and High Momentum Particle Identification Detector (HMPID), covering non-overlapping sections in azimuth. The ALICE COsmic Ray DEtector (ACORDE) detector is mounted on top of the solenoid magnet, and triggers on cosmic rays for calibration and alignment purposes, in addition to cosmic ray physics. Several smaller detector systems (ZDC, PMD, FMD, T0 and V0)[3] are placed in the forward direction at small angles, for global event characterization and triggering purposes [125]. The forward muon arm placed at polar angles from 2 ° - 9 °, is dedicated to the detection of muons, and designed to measure the production of heavy-quark resonances. Various information of the detectors, e.g., their position and acceptance, is listed in Appendix B.

The most relevant detector subsystems for the analysis presented in this thesis will be discussed further in the following sections.

3.2.1 Inner Tracking System (ITS)

The Inner Tracking System (ITS) is the innermost detector of the central barrel, situated immediately outside the beam pipe. The main purposes of ITS is to localize the primary vertex with a resolution better than 100 μm, to reconstruct the secondary vertices from the decays of hyperons, D mesons and B mesons, to track and identify

[3] Zero Degree Calorimeter (ZDC), Photon Multiplicity Detector (PMD), Forward Multiplicity Detector (FMD), Time-Zero (T0) and Veto-Zero (V0).

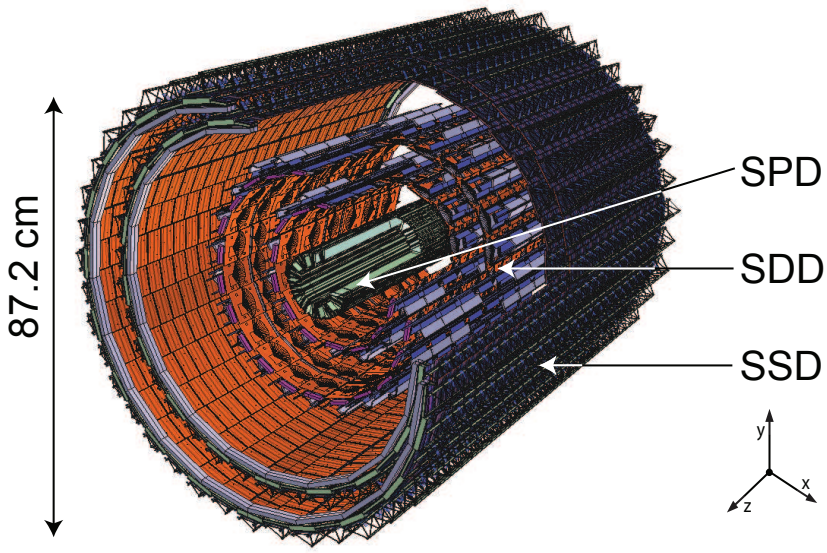

Figure 3.3: Schematic view of the Inner Tracking System (ITS). The three subsystems, i.e., the Silicon Pixel Detector (SPD), Silicon Drift Detector (SDD) and Silicon Strip Detector (SSD) are indicated. Figure from [127].

particles with momentum below 200 MeV/c, to improve the momentum and angle resolution for particles reconstructed by the TPC and to reconstruct particles traversing dead regions of the TPC [125]. The ITS provides excellent resolution, especially at low p_{T}, and as an example the relative momentum resolution achievable is better than 2% for pions in the interval 100 $\mathrm{MeV}/c < p_{\mathrm{T}} < 3$ GeV/c [125]. A spatial resolution of 12 μm in the plane perpendicular to the beam axis is achieved for the two innermost layers, designed to cope with the high track density close to the primary vertex of interactions [125]. ITS consists of six cylindrical layers of silicon detectors, divided into three subsystems with two layers each, the innermost being Silicon Pixel Detector (SPD), followed by Silicon Drift Detector (SDD) and Silicon Strip Detector (SSD). A schematic representation of the ITS, displaying the three subsystems, is seen in Figure 3.3. The main parameters for each detector layer is summarized in Table 3.1.

The ITS was designed with a very low material budget in order to limit the effects of Coulomb scattering for particles traversing the detector, causing unwanted background contributions, e.g., electrons from photon conversions. The total material budget for the full ITS, including sensors, electronics, cabling, support structures and cooling, amounts to 7.66 % of the radiation length, X_0, perpendicular to the de-

tector surfaces [4].

The Silicon Pixel Detector (SPD) constitutes the two innermost layers of the ITS, meaning it is the detector which will see the highest particle track density of the experiment. The silicon pixel technology was chosen to cope with track densities up to 50 tracks/cm^2, while withstanding the relatively high expected radiation doses [125]. The technology is based on hybrid silicon pixels, consisting of a two-dimensional matrix of reverse-biased silicon detector diodes bump-bonded to readout chips [125]. The readout of each pixel is binary, providing information of the position, but not energy loss of the passing particle. The main purpose of the SPD is tracking and vertex reconstruction, and it plays an important role in the determination of both the primary and secondary vertices. In contrast to the SPD, both the SDD and SSD use analog readout, allowing them to provide information of the differential particle energy loss, $\mathrm{d}E/\mathrm{d}x$, and thus be used for particle identification. The SDD is produced from very homogeneous high-resisitivity (3 kΩcm) neutron transmutation doped (NTD) silicon, with the sensitive area split into two drift regions by a central cathode strip [125]. Particles crossing the active area of the detector will generate electron-hole pairs, and information of the passing particle is obtained by measuring the drift time of generated electrons as they traverse the active region. The final two layers of the ITS, the SSD, is composed of double sided silicon microstrip sensors. The detector modules of the SSD consists of the strip itself, read out by two two hybrid circuits. The main tasks of both the SDD and SSD is tracking and PID, but a fundamental additional requirement for the technology in the two outer layers was the ability of accurate prolongation of tracks between the ITS and the TPC.

3.2.2 Time Projection Chamber (TPC)

The Time Projection Chamber (TPC), situated around the ITS, is the main tracking detector of ALICE, and it also plays an important role in the charged particle identification capabilities of the experiment. The TPC provides a good momentum resolution for a wide interval in p_{T}, ranging from 0.1 GeV/c up to 100 GeV/c. The detector was designed to operate under extreme particle multiplicity densities, expected at the time of the design to result in up to 20000 tracks in the detector volume per event [125]. The active volume of the TPC cylinder has an inner radius of about 85 cm, an outer radius

[4] The sum of the contributions to X_0 from Table 3.1 is 6.36% of the X_0, while the last 1.3 % of the radiation length is due to the thermal shields and supports installed between the SPD and SDD barrels, and between the SDD and SSD barrels [127].

Table 3.1: Parameters of the ITS detector layers [127].

Layer	Silicon detector type	r [cm]	±z [cm]	Number of modules	Active area per module $r\varphi$ x z [mm^2]	Resolution $r\varphi$ x z [μm^2]	Material budget X/X_0 [%]
1	pixel	3.9	14.1	80	12.8 x 70.7	12 x 100	1.14
2	pixel	7.6	14.1	160	12.8 x 70.7	12 x 100	1.14
3	drift	15.0	22.2	84	70.17 x 75.26	35 x 25	1.13
4	drift	23.9	29.7	176	70.17 x 75.26	35 x 25	1.26
5	strip	38.0	43.1	748	73 x 40	20 x 830	0.83
6	strip	43.0	48.9	950	73 x 40	20 x 830	0.86

of about 250 cm, and an overall length along the beam direction of 500 cm. A schematic view of the detector can be seen in Figure 3.4 [125]. The barrel is divided into two parts by a 30 μm thick central 100 kV electrode, required to generate the drift field of 400 V/m [125]. At both ends of the barrel, multi-wire proportional chambers with cathode pad readouts are mounted into 18 trapezoidal sectors [125]. The 90 m^3 drift volume is filled with a Ne-Co_2 (90%/10%) [128] gas mixture at atmospheric pressure, which results in relatively low coulomb scattering, while having good diffusion characteristics and a high positive ion mobility, allowing a fast removal of positive ions from the drift volume [129]. As charged particles traverse the detector, they ionize the gas, and ionized electrons drift in the electric field towards the end plates where the readout is performed.

Combining the tracking capabilities of the ITS and TPC yields a p_{T} resolution, $\Delta p_{\mathrm{T}}/p_{\mathrm{T}}$, of 1.5% for tracks with p_{T}=10 GeV/c, and 2.5% for tracks with p_{T}=30 GeV/c [126]. A $\mathrm{d}E/\mathrm{d}x$ resolution of 5.2% is achieved in pp collisions, and 6.5% in Pb–Pb [126].

3.2.3 Transition Radiation Detector (TRD)

The Transition Radiation Detector (TRD) surrounds the TPC, and is designed to provide electron identification and pion rejection for momenta above 1 GeV/c, by exploiting the transition radiation from electrons traversing the radiator, and measuring their specific energy loss [125]. The detector modules consist of a radiator followed by a drift chamber filled by a Xe/CO_2 (85%/15%) gas mixture [125]. Ionizing radiation is produced in the counting gas by traversing particles, but for particles exceeding the threshold for transition radiation ($\gamma \approx 1000$), X-ray photons in the energy range of

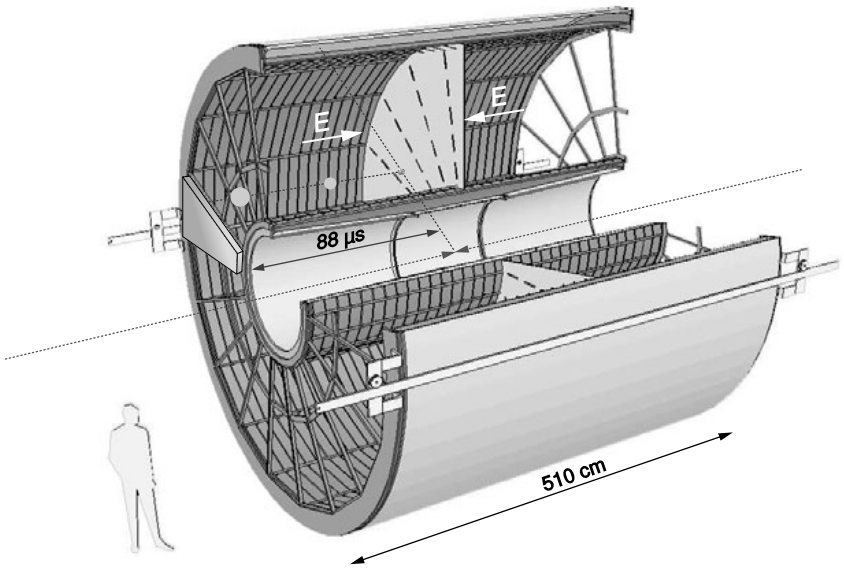

Figure 3.4: Schematic view of the ALICE TPC. At the left side of the figure, one of the 18 readout pads can be seen at the end of the barrel. The central electrode, along with the direction of the drift fields can also be seen. Figure from [130].

1-30 keV are produced in the radiator material. These photons are efficiently converted to electron-positron pairs by the high-Z counting gas at the very beginning of the drift region, leading to a peak in the average pulse height at larger drift times. The likelihood of a particle being an electron is calculated based on the total accumulated charge, refined by a sampling in time bins [131]. The rejection power for pions in the TRD is generally specified for a given electron efficiency, with the aim being a 1% pion efficiency at an electron efficiency of 90% [125]. In addition to its electron identification and tracking capabilities, the TRD can also be used as a level-1 trigger, assisting analyses which rely on rare probes in (semi-)electronic decay channels [132].

The TRD consists of 540 individual modules, arranged into 18 super-modules around the barrel, each of which is divided into 5 stacks in the beam direction, separated further into 6 layers of modules in the radial direction [125]. A cross-sectional view of the TRD is seen in Figure 3.5, displaying the 13 (of the total 18) super-modules installed at the time of the p–Pb data taking in 2013. During LHC Run 2[5], all 18 TRD modules were installed.

[5] LHC Run 2 started in mid-2015, after the Long Shutdown (LS1) starting in 2013, after the end of Run 1.

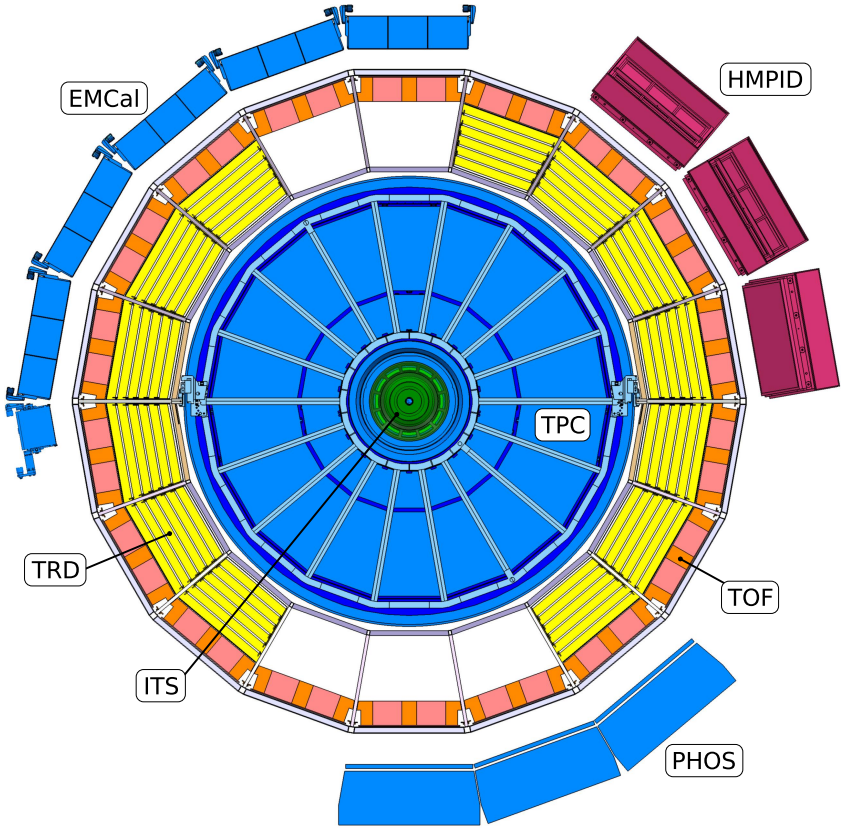

Figure 3.5: Cross-sectional view of the ALICE central barrel detectors, as of 2013. 13 of the planned 18 TRD modules, and 3 of the 5 planned PHOS modules, were installed at the given time.

3.2.4 Time of Flight (TOF)

The outermost of the central barrel detectors with full azimuthal acceptance is the Time Of Flight (TOF) detector, situated outside the TRD. The TOF detector is designed to provide PID by measuring the flight time of particles from the collisions, with a resolution of $\sim$ 80 ps[6] [126]. The time of flight is calculated from the arrival time measured by TOF, and the event time estimated on an event-by-event basis, performed by the T0 detector [133]. Occasionally, no signal may be observed by the T0

[6] For pions with a momentum around 1 GeV/c, in the centrality range 0-70% in Pb–Pb collisions. The value includes the intrinsic detector resolution, the contribution from electronics and calibration, the uncertainty on the start time of the event, and the tracking and momentum resolution [126,133].

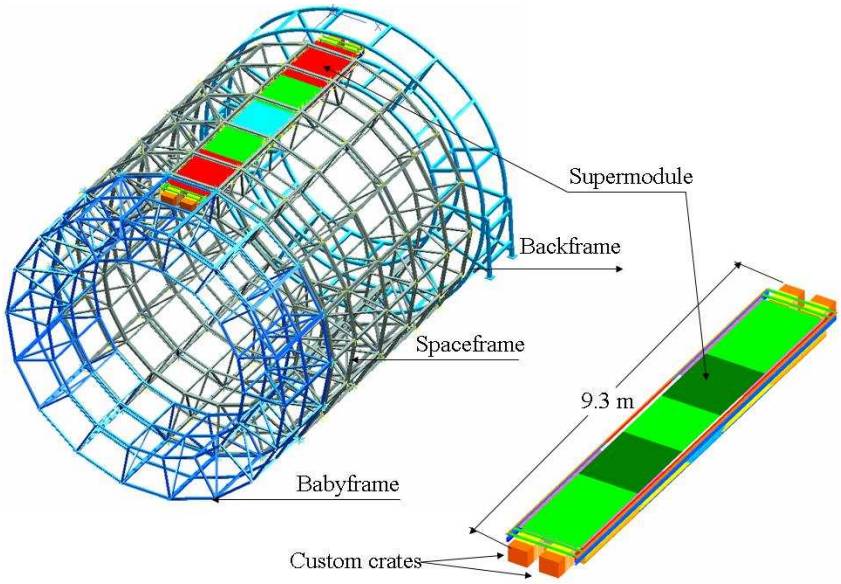

Figure 3.6: Schematic representation of the TOF detector, with one of the 18 super-modules in place. Each super-module contains 5 segments, with lengths of 117 cm, 137 cm and 177 cm for the central, intermediate and external modules respectively. Figure from [125].

due to the detector acceptance, in which case the TOF estimates the event time by a combinatorial algorithm comparing the measured TOF times to the expected times of the tracks, assuming a common event time [133].

TOF consists of a large array of multigap resistive plate chambers (MRPC), which have a high and uniform electric field over the full sensitive gaseous volume of the detector [125]. There is no drift time associated with the movement of the electrons to a region of high electric field, as for other types of gaseous detectors, and thus the only time jitter in the device is caused by fluctuations in the growth of the avalanche started by the traversing charged particle. The detector consists of 90 modules, divided into 18 super-modules in azimuth, where each sector consists of 5 segments in the beam direction. Every module of the TOF consists of a group of MRPC strips (15 in the central segments, and 19 in the intermediate and external modules), enclosed in a box which defines and seals the gas volume, totaling at 1638[7] MRPC strips [125]. A

[7] Three central modules in front of the PHOS have not been installed, in order to reduce the material budget in front of this high resolution electromagnetic calorimeter, in the three installed (of its five planned) modules [125]. Due to this exclusion, a total of 1593 MRPC strips are installed.

schematic representation of the TOF frame with one super-module installed is seen if Figure 3.6.

The TOF can also be used as a level-0 trigger, and has, for example, been used to select resonance decays in ultra-peripheral collisions during the Pb–Pb collisions in 2010 and 2011, and for p–Pb collisions in 2013 [133].

3.2.5 Electromagnetic Calorimeter (EMCal)

The electromagnetic calorimeter (EMCal) is situated outside the TOF detector, covering a pseudorapidity range of $|\eta| < 0.7$, and $80\,^{\circ} < \varphi < 187\,^{\circ}$ in azimuth. The detector is designed to explore the physics of jet quenching over the large kinematical range accessible in heavy-ion collisions at the LHC [130], and increases the electromagnetic calorimeter coverage of ALICE by nearly an order of magnitude, while also providing a fast and efficient trigger for hard jets, photons and electrons [125]. The energy resolution of EMCal was determined to be $1.7 \bigoplus 11.1/\sqrt{E/(\mathrm{GeV})} \bigoplus 5.1\ E(\mathrm{GeV})\%$ [134] from electron test beam data, where E is the measured energy. The first (constant) term of the resolution originates from systematic effects, the second term is attributed to stochastic fluctuations due to intrinsic detector effects and the third term is due to electronic noise summed over the clusters used to reconstruct the electromagnetic showers [134]. In addition to its functionality as a calorimeter, EMCal is also used to identify electrons, by measuring the energy over momentum ratio, E/p.

The EMCal detector is a large Pb-scintillator sampling calorimeter, constrained in size by the available free space and the maximum weight which can be supported by the surrounding magnet [125]. As seen in Figure 3.5, all the planned 5+⅓ detector modules were in place during the data taking in 2013.

Di-jet Calorimeter (DCal)

A Di-jet Calorimeter (DCal) [135] was installed during the Long Shutdown (LS1) between LHC Run 1 and Run 2. The DCal consists of 8 modules of the EMCal design with reduced length in η, placed around the PHOS detector, opposite in azimuth of EMCal, with an acceptance of 67° in azimuth, and $|\eta| < 0.7$ in pseudorapidity. The combined EMCal an DCal allows to study back-to-back correlations and di-jets.

3.2.6 PHOS

The PHOton Spectrometer (PHOS) is a high-resolution electromagnetic spectrometer,

seen in the lower part of Figure 3.5. The detector consists of a highly segmented electromagnetic calorimeter (PHOS) and a Charged-Particle Veto (CPV) detector [125]. PHOS is subdivided into 5 independent PHOS+CPV units [125], 3 of which were installed during the data taking in 2013. A 4^{th} module was installed before LHC Run 2 started in 2015.

3.2.7 V0

The V0 system consists of two scintillator arrays at asymmetric positions, on either side of the interaction point, called the V0A and V0C detectors. The main purpose of the V0 system is to provide a level-0 minimum bias trigger in all collision types, in addition to centrality based triggers in Pb–Pb collisions. The trigger requirements have varied for different trigger modes and collision types, but is generally dependent on information from the V0 itself, the LHC bunch crossing signals and other detectors triggering on specific event topologies, e.g., the muon spectrometer or EMCal. In addition to the trigger functionality, V0 is also used to monitor LHC beam conditions, to reject beam-induced backgrounds and to measure basic physics quantities such as luminosity, particle multiplicity, centrality and event plane direction in nucleus-nucleus collisions [136].

V0A is located 329 cm from the nominal vertex (z = 0) on the opposite side of the muon spectrometer (see Figure 3.2) and covers pseudorapidity ranges of $2.8 < \eta < 5.1$, while V0C is located 89 cm from the nominal vertex, on the face of the hadronic absorber in front of the muon spectrometer, and covers a range of $-3.7 < \eta < -1.7$ [136].

3.2.8 Other Detectors

In addition to the already mentioned detector systems, several others are also installed in ALICE. The T0 detector is designed to generate a start time (T0) for the TOF detector, corresponding to the real time of the collision, in addition to measuring the vertex position for each interaction and using this information to provide a level-0 trigger. The Zero Degree Calorimeter (ZDC) consists of two hadronic calorimeters placed 116 m[8] from the interaction point (IP) on either side, as seen in Figure 3.2, in addition to two small electromagnetic calorimeters placed about 7 m from the IP, on both sides of the LHC beam pipe, in opposite direction of the muon arm [125]. ZDC

[8] The ZDCs were moved to $|z| \approx 112.5$ m during the LHC winter shutdown 2011/2012 [126].

is used to determine the event centrality and for triggering purposes. The Photon Multiplicity Detector (PMD) measures the multiplicity and spatial (η, φ) distribution of photons, while the Forward Multiplicity Detector (FMD) provides charged-particle multiplicity information. The High-Momentum Particle Identification Detector (HMPID), seen in Figure 3.5, is dedicated to PID of charged hadrons outside the momentum interval attainable through energy loss (TPC and ITS) and time-of-flight measurements (TOF). The muon spectrometer is designed for muon detection.

3.3 Particle Identification (PID)

In order to facilitate the study of a large number of observables, ALICE utilizes a wide variety of particle identification (PID) techniques, and several of the detectors possess PID capabilities. The detectors identify particles by different methods, and the performance for each method is dependent on the momentum and species of the particle being identified. Combining the information from more detectors allows to accurately distinguish between particle species in a wide momentum range. Of particular interest to the analysis presented in this thesis are the daughters of the D^0 meson from the decay-channels discussed in Section 2.3, i.e., kaons (K), pions (π) and heavy-flavour electrons (HFE). In the results presented in this thesis, the PID has been performed by the TPC over the full p_{T} range, in addition to TOF at lower p_{T}. Both of these detectors have a full coverage in the azimuthal angle in the pseudorapidity interval $|\eta| < 0.9$.

The TPC detector performs PID by simultaneously measuring the specific energy loss ($\mathrm{d}E/\mathrm{d}x$), charge and momentum of each particle traversing the detector. The $\mathrm{d}E/\mathrm{d}x$ plotted against momentum is seen in Figure 3.7. The solid curves in the figure correspond to fits of the ALEPH parametrization [138] of the Bethe-Bloch formula for various particle species. A selection based on the deviation of a track from the expected value can then be performed. As seen from the figure, the solid lines of different particle species overlap in some regions of momentum, meaning that a discrimination between the different particle species can not be made. In these situations, particle identification of the tracks rely on information from other detectors.

The TOF PID procedure is performed by calculating the velocity, β, by measuring the flight time of particles reaching the detector. The momentum of the track is obtained from the TPC by matching tracks between the two detectors. In Figure 3.8, the velocity of tracks have been plotted against the momentum, showing distinct lines for each particle species. A 3σ separation is achieved up to 2.5 GeV/c for K/π, and up to

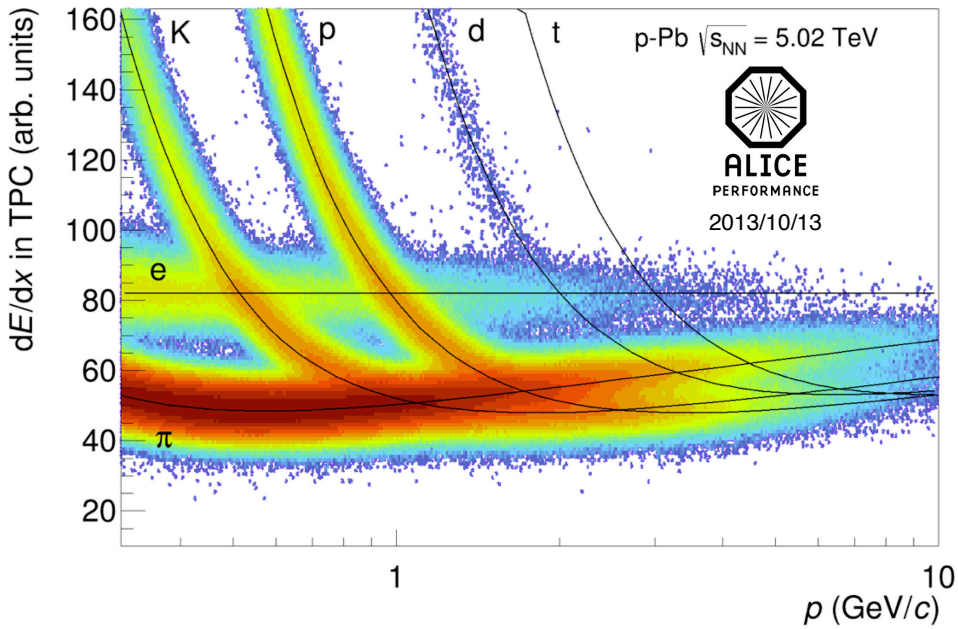

Figure 3.7: dE/dx of charged particles vs their momentum measured by the TPC in pPb collisions. The solid lines are parametrizations of the detector response based on the Bethe-Bloch formula for various particle species.

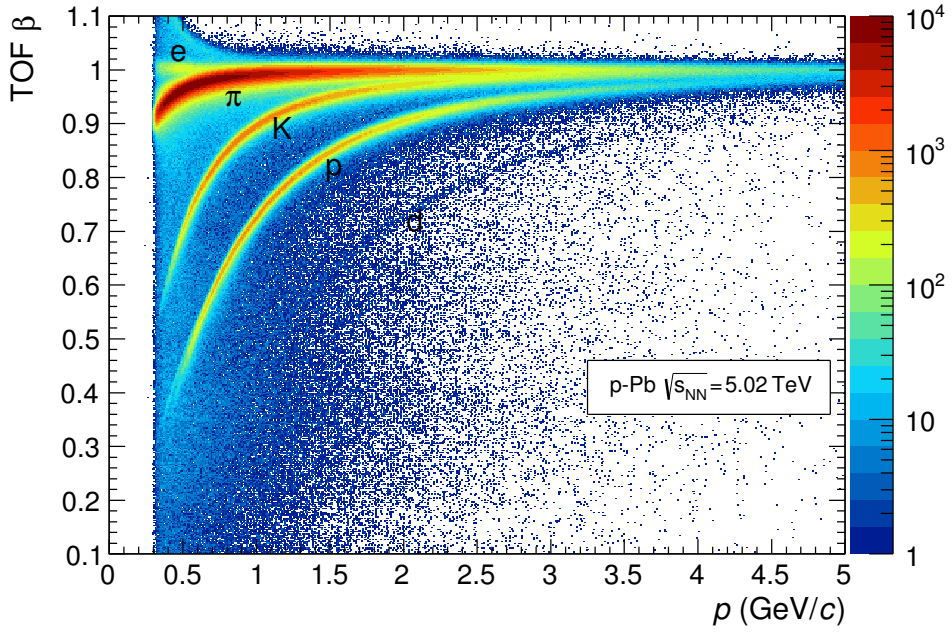

Figure 3.8: $\beta = v/c$ of charged particles as a function of their momentum, for particles reaching the TOF detector in p–Pb collisions. Electrons, pions, kaons, protons and deuterons are marked by their respective letters in the figure. Figure from [126].

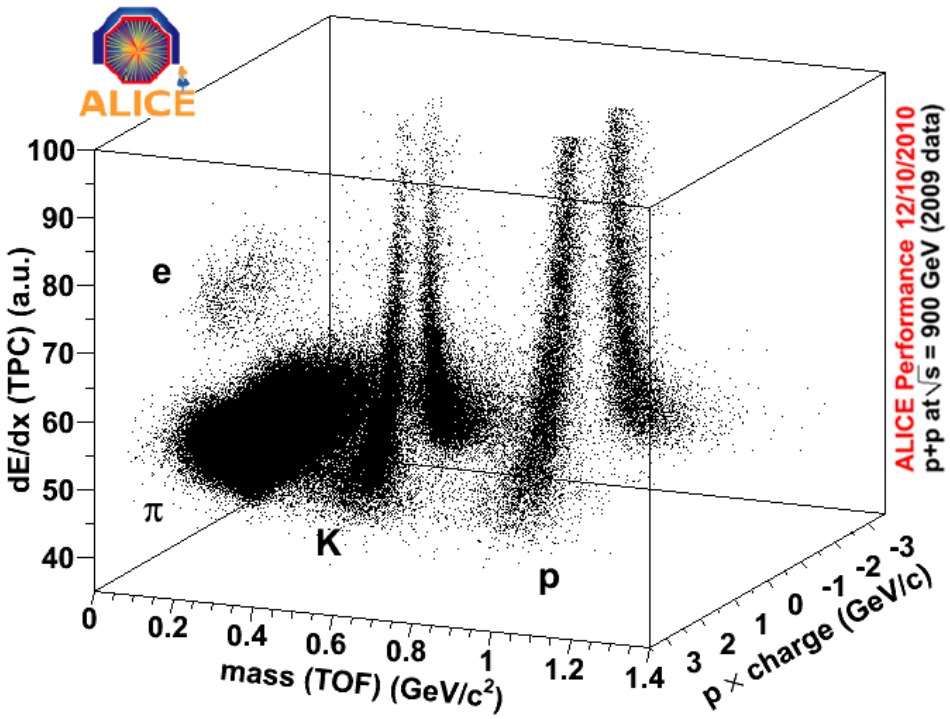

Figure 3.9: Combination of the TPC (dE/dx) information and the mass calculated from the TOF detector, as a function of momentum×charge, in pp collisions at $\sqrt{s} = 900\,\mathrm{GeV}$ at the LHC, illustrating the separation of the particle species. Figure from [137].

4 GeV/c for p/K [139]. Figure 3.9 illustrates the separation power by combining information from the TPC and TOF, in this case for pp collisions. As can be seen from the figure, a clear separation of the particle species is acheived.

In addition to the detectors used for PID in this thesis, there are additional options which offer additional identification possibilities, and were considered for use in the analysis. The EMCal detector provides discrimination of electrons and hadrons by calculating the ratio E/p of the energy deposited, E, to the momentum, p. As electrons deposit all of their energy in the EMCal, the ratio, E/p, is around unity, while for charged hadrons the ratio is, on average, much smaller [140]. This approach can greatly improve the purity of the electron sample, and has been used, e.g., in the measurement of electrons from heavy-flavour hadron decays in p–Pb collisions in the range 6 < p_{T} <12 GeV/c [140]. The ITS detector also offers PID capabilities by $\mathrm{d}E/\mathrm{d}x$ measurements in the four outer layers, i.e., the SDD and SSD, at low p_{T}, with π/kaon

separation up to $\sim$0.5 GeV/c, and K/p separation up to $\sim$ 1GeV/c. As mentioned in Section 3.2.3, the TRD can also be used to identify electrons, and separate them from pions for momenta above 1 GeV/c.

Chapter 4

Reconstruction and Track Selection

This chapter will discuss the reconstruction of D^0 mesons and selection of electrons used in the analysis of D^0-e correlations. In Section 4.1, a brief description of the p–Pb collision system, event selection and data sample will be presented. A detailed description of the D^0 meson reconstruction will be given in Section 4.2, followed by the discussion of the selection strategy for heavy-flavour electrons (HFE) in Section 4.3.

4.1 Data Sample and Event Selection

The data analyzed in this thesis was recorded by ALICE during p–Pb collisions at $\sqrt{s_{\mathrm{NN}}} = 5.02\,\mathrm{TeV}$, in the beginning of 2013[1]. Due to the different energy of the colliding beams ($\sqrt{s} = 4\,\mathrm{TeV}$ for protons and $\sqrt{s_{\mathrm{NN}}} = 1.58\,\mathrm{TeV}$ lead nuclei), the nucleon-nucleon centre-of-mass frame was moving with a rapidity $|\Delta y_{\mathrm{NN}}| = 0.465$ in the proton beam direction (positive rapidities), leading to a rapidity coverage of -0.96 $< y_{cms} <$ 0.04 [141]. A minimum bias trigger scheme was used to select events, with the requirement of at least one hit in both the V0A and V0C detectors, estimated to be sensitive to ∼96.4% of the p–Pb inelastic cross section [80,142]. A further restriction on the selection was introduced by considering only events with a primary vertex within ±10 cm of the centre of the detector along the beam line. The total number of events passing these criteria was approximately 10^8, corresponding to an integrated luminosity, $L_{\mathrm{int}} = N_{\mathrm{MB}}/\sigma_{\mathrm{MB}} = (48.6 \pm 1.6)\ \mu\mathrm{b}^{-1}$, where N_{MB} is the number of p–Pb collisions passing the minimum-bias trigger condition, and σ_{MB} is the cross section of

[1] See Appendix A for more details of the data sample.

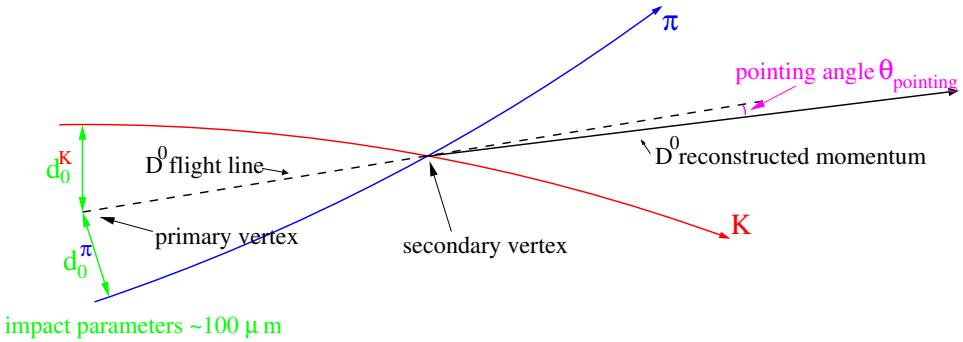

Figure 4.1: Schematic representation of the $D^0 \rightarrow K^-\pi^+$ decay. The displacement of the secondary vertex from the primary vertex, and the product of the transverse projections of the impact parameters of the daughter tracks, $d_0^K x d_0^\pi$, are particularly useful as topological D^0 meson selection cuts. Figure from [21].

the V0 trigger, measured to be 2.09 b $\pm$ 3.5% (syst) with a p–Pb van der Meer (vdM) scan [142] [141].

4.2 Reconstruction and Selection of D^0 Mesons

The procedure used for reconstruction and selection of D^0 mesons follows the common strategy within the ALICE collaboration, as explained in detail in [101]. The D^0 meson has been studied via the hadronic decay channel $D^0 \rightarrow K^-\pi^{+[2]}$, which has a branching ratio B. R.= (3.88 $\pm$ 0.05)% [11]. In order to separate the D^0 signal from the large combinatorial background caused by uncorrelated tracks, the secondary vertex was reconstructed and constrained by a topological selection. A particle identification strategy of the daughter particles was applied to further reduce the combinatorial background. Finally, the raw signal yield was extracted from the invariant mass of the decay daughers. In the following, the selection procedure will be discussed briefly.

4.2.1 Secondary Vertex Reconstruction and Selection

The D^0 meson decay via weak processes and have a mean proper decay length of 122.9 μm [11], resulting in a typical displacement of the secondary vertices by a few hundred μm from the primary vertex of the interaction, as illustrated in Figure 4.1. The D^0 meson is created at the primary vertex and travels along the flight line until it decays into a kaon and a pion, creating a secondary vertex. The decay occurs before the D^0 meson reaches the first layer of the detector, and thus the secondary vertex must be reconstructed by identifying a kaon and a pion track which can be traced back to a common origin. D^0 meson candidates were defined using pairs of such tracks, with a charge sign combination of the daughter tracks matching that of the aforementioned decay channel. A secondary vertex was computed for each D^0 meson candidate and a selection procedure was imposed based on typical kinematical and geometrical properties of the single tracks and the reconstructed secondary vertex [105]. The minimum accepted displacement from the primary vertex to the secondary vertex was 100 μm. The tracks were required to be within the pseudorapidity range of $|\eta|$<0.8 and have transverse momenta $p_{\mathrm{T}} > 0.5$ GeV/c. At least 70 (of the maximum 159) associated space points were required in the TPC, in addition to a cut on the χ^2 per degree of freedom (ndf) of the momentum fit in the TPC at χ^2/ndf < 2. Additionally, at least one hit in either of the two layers of the SPD was required, and both the TPC and ITS had to be included in the refitting procedure during the track reconstruction[3].

The cut values, summarized in Table 4.1, were tuned for the different daughter species and D meson p_{T} regions in order to obtain a large statistical significance of the D^0 meson signal. The maximum distance of closest approach (DCA) between two tracks was required to be less than 300 μm. The θ^* angle is defined as the angle between the pion momentum and the D^0 flight line in the reference frame of the decaying D^0, and in this reference frame the pion and the kaon are emitted isotropically with three-momenta of equal magnitude and opposite direction [105]. This causes the cos(θ^*) distribution for signal pairs to be almost flat, while the distribution for background pairs accumulates at cos(θ^*)= $\pm$1, and the background can therefore be reduced by removing pairs above a given |cos(θ^*)| limit close to this value [105]. The absolute value of the cosine of θ^* was required to be less than 0.8 for D meson p_{T} up to 8 GeV/c, and tightened to |cos(θ^*)| < 0.9 in the 8 < p_{T} < 12 GeV/c region, and

[2] This analysis studies the decay of both the $D^0 \rightarrow K^-\pi^+$ and the decay of the antiparticle $\overline{D^0} \rightarrow K^+\pi^-$, but for compactness only the D^0 decay is discussed.

[3] The track reconstruction procedure is discussed in detail in [126].

Table 4.1: Topological cuts applied to D^0 candidates in different p_{T} intervals, adapted for p–Pb collisions.

$\mathrm{p_T}$ (GeV/c) Filter variable		[2,4]	[4,5]	[5,6]	[6,8]	[8,12]	[12,16]
DCA [μm]	<	300	300	300	300	300	300
$\lvert\cos(\theta^*)\rvert$	<	0.8	0.8	0.8	0.8	0.9	1.0
$\mathrm{p_T}$ (K, π) [GeV/c]	>	0.7	0.7	0.7	0.7	0.7	0.7
$\mathrm{d}_0^{K,\pi}$ [cm]	<	0.1	0.1	0.1	0.1	0.1	0.1
$\mathrm{d}_0^K \mathrm{x} \mathrm{d}_0^\pi$ [μm^2]	<	-30000	-15000	-10000	-8000	-5000	10000
$\cos(\theta_{pointing})$	>	0.9	0.9	0.9	0.85	0.85	0.85

$|\cos(\theta^*)| < 1.0$ in the $12 < p_{\mathrm{T}} < 16$ GeV/c region.

The pointing angle, $\theta_{pointing}$, is the angle between the reconstructed momentum vector of the D^0 meson and the flight line, where the flight line is defined by the primary and secondary vertex, as illustrated in Figure 4.1. In a recent study [105] of the D^0 meson at ALICE, no correlation was found between the reconstructed momentum and the reconstructed flight line for background pairs, meaning that the $\cos(\theta_{pointing})$ is almost uniformely distributed for these pairs. For the signal pairs, however, the distribution was found to be characterized by a peak at $\cos(\theta_{pointing})$=1. A cut on low values of $\theta_{pointing}$ was therefore applied.

The product of the two transverse projections of the impact parameters of the daugher tracks, $\mathrm{d}_0^{\mathrm{K}}\mathrm{x}\mathrm{d}_0^{\pi}$, tend to be negative and large in absolute value for true decays, while being symmetric around zero for background decays [105]. Due to the strong correlation of $\cos(\theta_{pointing})$ and $\mathrm{d}_0^{\mathrm{K}}\mathrm{x}\mathrm{d}_0^{\pi}$ in the signal, these two parameters are very powerful for increasing the signal-to-background ratio [143].

In order to reduce the combinatorial background, particle identification was applied to the decay daughter candidates, i.e., kaons and pions. The candidates were required to be compatible within $\pm\, 3\sigma$ of the expected signal of the particle species for both TPC $\mathrm{d}E/\mathrm{d}x$ and TOF time-of-flight values. For tracks where the TOF information was not available, only the TPC PID was applied. The PID strategy was found to provide a reduction of the combinatorial background by about a factor three at low p_{T}, while preserving an efficiency of 95%, in a recent study of the D-meson production in p–Pb collisions, using the same PID procedure as stated here [80] (see section 4.2.3 for a discussion of the D^0 efficiency).

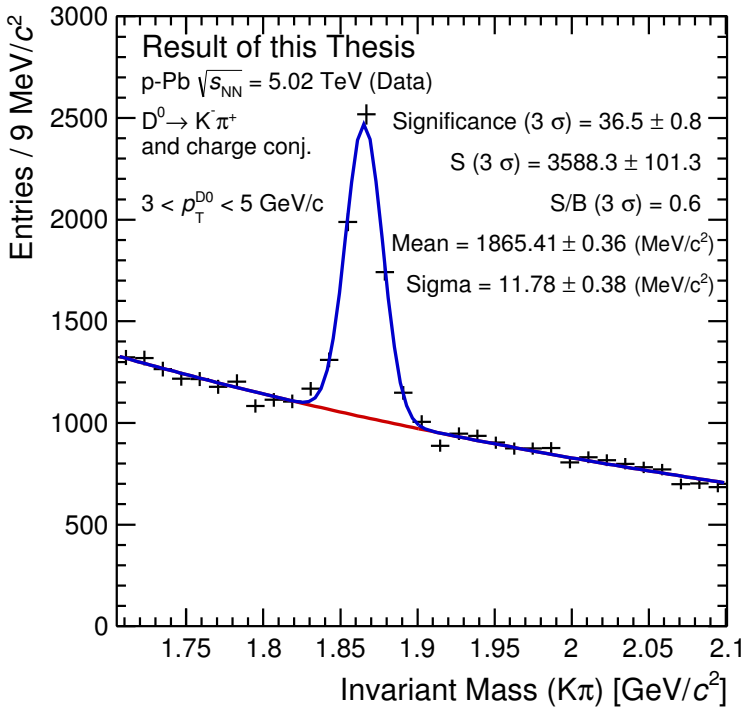

Figure 4.2: Invariant mass distribution of D^0 meson candidates reconstructed from $\mathrm{D}^0 \rightarrow \mathrm{K}^-\pi^+$ decays, and their charge conjugates. The candidates are selected in the interval $3 < p_{\mathrm{T}}^{\mathrm{D}^0} < 5$ GeV/c, in $\sqrt{s_{\mathrm{NN}}} = 5.02$ TeV p–Pb collisions at ALICE. The background is estimated by an exponential fit (red line) and the signal is fitted by a Gaussian function (blue line).

4.2.2 Invariant Mass Calculation and Yield Extraction

The invariant mass of the the D^0 meson candidates was calculated based on the daughter particles, producing a distribution for each p_{T} region. The invariant mass distributions were fitted by a Gaussian function for the signal, and an exponential function for the combinatorial background, as seen in Figure 4.2. The extracted raw signal yield, signal over background ratio, statistical significance, and the parameters of the Gaussian peaks for each p_{T} region is seen in Table 4.2.

Table 4.2: Raw D0-meson yields, extracted from fits of the invariant mass distributions of D^0 meson candidates.

p_{T} range [GeV/c]	Signal (3σ)	Significance	μ [MeV/c]	σ [MeV/c]
3-5	3588 ± 101	36.5 ± 0.8	1865.41 ± 0.36	11.78 ± 0.38
5-8	2044 ± 65	31.7 ± 0.8	1866.13 ± 0.48	13.42 ± 0.47
8-16	1003 ± 45	22.9 ± 0.8	1865.18 ± 0.89	18.00 ± 0.94

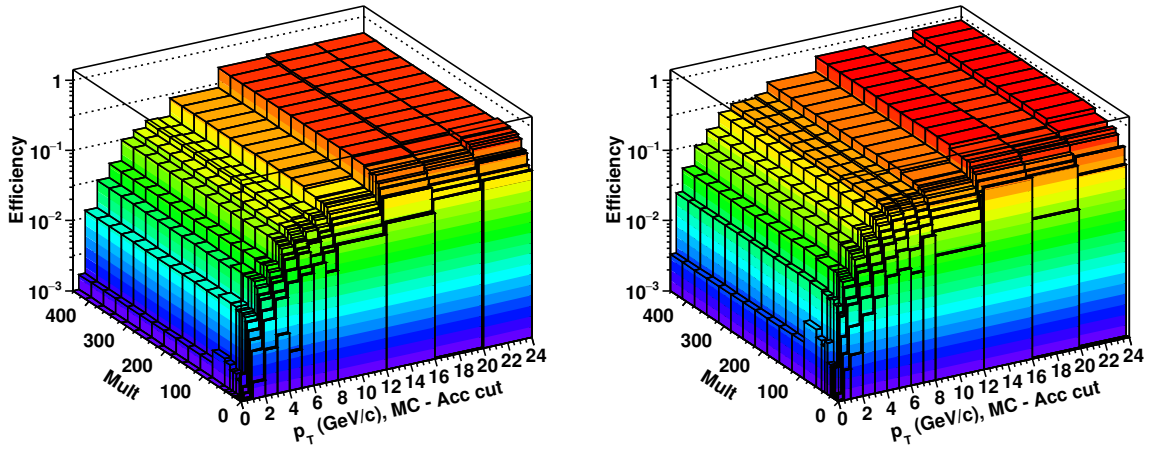

Figure 4.3: Reconstruction efficiency versus p_{T} and multiplicity for prompt (left) and feed-down (right) D^0 mesons in p–Pb collisions at $\sqrt{s_{\mathrm{NN}}} = 5.02\,\mathrm{TeV}$.

4.2.3 Efficiency of D^0 Selection

The reconstruction efficiency has been calculated separately for prompt and feed-down D^0 mesons, using Monte Carlo (MC) simulations including detailed descriptions of the geometry of the apparatus and of the detector response, as explained in [80]. The MC sample[4] consists of an underlying p–Pb sample generated with HIJING, enhanced with one $\mathrm{c\bar{c}}$ or $\mathrm{b\bar{b}}$ pair decaying semileptonically per event, using the PYTHIA event generator. The generated particles were transported through the detector using GEANT3. In order to correct for geometrical acceptance effects, an acceptance factor was calculated in a minimum bias sample, and multiplied by the reconstruction efficiency to generate the full efficiency maps, as seen in Figure 4.3,

[4] See Appendix A.2 for further details of the sample.

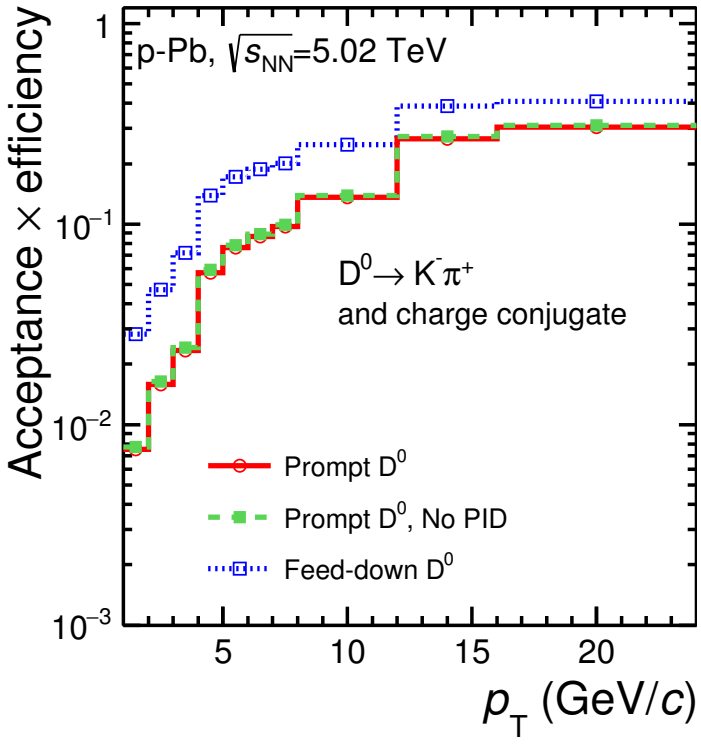

Figure 4.4: Product of acceptance and efficiency for D^0 mesons as a function of p_{T}. Efficiencies are shown for prompt D^0 with (solid line) and without (dashed line) PID selection applied, and for feed-down D^0 (dotted line). Figure and caption from [80].

for prompt and feed-down D^0 mesons. The prompt D^0 meson efficiency rises from about 1-2% in the $1 < p_{\mathrm{T}} < 2$ GeV/c interval, where a stricter selection is enforced due to the higher combinatorial background in that region, to 20 % in the $12 < p_{\mathrm{T}} < 24$ GeV/c range. The observed multiplicity dependence of the efficiencies is a result of the improved primary vertex resolution at high multiplicity, which is an important topological parameter in the selection of D^0 mesons. The feed-down D^0 efficiency is higher by about a factor two compared to that of the prompt D^0, mainly due to the more displaced primary vertex, making the topological selection more efficient [144]. A comparison of the acceptance×efficiency as a function of p_{T} for prompt and feed-down D^0 mesons is seen in Figure 4.4, while also comparing the prompt efficiency with and without PID of the decay daughters implemented. The efficiency was found to be about 5% lower when the PID procedure was implemented [80].

4.3 Electron Selection

The selection of electrons from heavy-flavour decays (HFE) is a process that requires a separation of electrons from other particle species, in addition to separating heavy-flavour electrons from non-heavy-flavour electrons. The selection strategy was based on that of the measurement of electrons from semi-leptonic heavy-flavour hadron decays with the ALICE experiment [73], along with the changes added for the D-e correlation analysis in pp collisions at ALICE [18]. A high purity sample of electrons has been obtained, with an selection efficiency above 60% in the $1 < p_{\mathrm{T}}^{\mathrm{e}} < 4$ GeV/c interval.

The stages of the selection procedure will be discussed in the following, and can be summarized in three steps:

1. Selection of reconstructed tracks.
2. Particle identification of electrons (PID).
3. Removal of non-HFE contributions.

4.3.1 Selection of Reconstructed Tracks

Reconstructed tracks are selected based on a variety of criteria, or *cuts*, as summarized in Table 4.3. As already mentioned, the selection cuts are based on previous experience [18, 73], and have been further adapted for the data sample of p–Pb collisions from 2013. As the energy deposit of electrons on the Fermi plateau is approximately 1.6 times larger than for minimum ionizing particles, the associated clusters are insensitive to detector threshold effects, and electron tracks have, on average, a higher number of clusters in the TPC [73]. A cut on the number of clusters can thus be used to enhance the electron/pion separation, and the number of clusters used for track reconstruction was therefore set to a minimum of 100 of the maximum 159 available clusters, while for the particle identification procedure a minimum of 80 clusters was required for the energy loss calculation. The pseudorapidity range was restricted to $|\eta_{lab}| < 0.8$ to ensure a high electron identification performance with the TPC. Background and non-primary tracks were suppressed by applying a cut on the distance of closest approach (DCA) to the primary vertex in the transverse plane (xy), DCAr, as well as in the beam direction (z), DCAz [73]. In the momentum region up to 1.3 GeV/c, where the TOF PID is crucial for the separation of particle species, a matching of the track to the TOF detector was required as part of the quality track cuts, to

ensure that the TOF PID could be used for tracks in this momentum region. Both the TPC and ITS were required to be included in the refitting procedure during the track reconstruction[5].

Table 4.3: List of quality track cuts for electron candidates.

Cut	Cut-values
ITS clusters	4
SPD requirement	hit in first layer (kFirst)
TPC clusters	100
TPC clusters for PID	80
$\|\eta\|$	0.8
p_T	0.5-10 GeV/c
DCAr [cm]	1
DCAz [cm]	2
TOF-matching	Yes (p < 1.3 GeV/c)
TPC refit	Yes
ITS refit	Yes

4.3.2 Particle Identification of Electrons

The particle identification for electrons was performed using the TPC in the full momentum range. In addition, TOF PID was used for momenta, p, up to 2 GeV/c. For tracks with p < 1.3 GeV/c TOF matching was required, while in the interval 1.3 GeV/c < p < 2 GeV/c TOF PID was used only while available, without enforcing the TOF matching criterion. The purpose of this momentum-segmented PID-strategy is to fully benefit from the TOF PID where it is needed the most, while using it only when available in less important regions, thus reducing the of loss in efficiency from the limited TOF matching efficiency[6].

The TPC PID was configured to accept track candidates with a measured specific energy loss within ± 3 standard deviations (n_σ^{TPC}) of the expected value for electrons, while the TOF PID accepted track candidates within ± 3 n_σ^{TOF} from the expected electron time-of-flight for the tracks. The relatively loose lower bound of -3 n_σ^{TPC} for the

[5] The track reconstruction procedure is discussed in detail in [126].
[6] Considerations regarding the selection efficiency are discussed in Section 4.3.4.

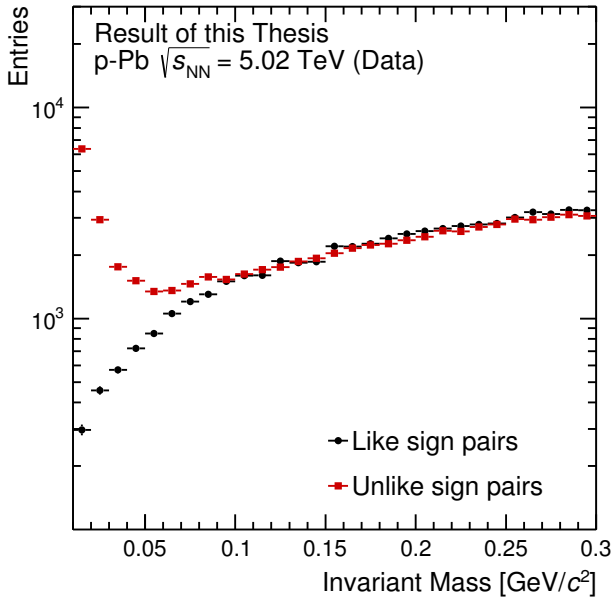

Figure 4.5: Invariant mass distributions of unlike sign (ULS) and likesign (LS) pairs of electrons. The difference between the unlike sign and like sign contributions is estimated to be photonic background.

electron PID results in a noticeable background contribution, especially from pions, which was reduced by identifying pion candidate tracks within $\pm 3\ n_\sigma^{\mathrm{TPC}}$ of the expected $\mathrm{d}E/\mathrm{d}x$ for pions in the TPC for all tracks above 1 GeV/c, and rejecting these. In the range where the TOF PID is used without the TOF-matching requirement, i.e., 1.3 < p_{T} < 2.0 GeV/c, the background proton contribution was reduced by removing track candidates within a $\pm 3\ n_\sigma^{\mathrm{TPC}}$ band around the expected $\mathrm{d}E/\mathrm{d}x$ for protons.

4.3.3 Removal of Non-HFE Contributions

The selected electron candidate sample after track cuts and PID, referred to as the *inclusive* electron sample, contains electrons from background electrons (non-HFE), in addition to HFE electrons. The majority of the background contribution originates from photon conversions in the detector material ($\gamma \rightarrow \mathrm{e}^+\mathrm{e}^-$) and Dalitz decays of neutral mesons, e.g., $\pi^0 \rightarrow \mathrm{e}^+\mathrm{e}^-$ and $\eta \rightarrow \mathrm{e}^+\mathrm{e}^-$ [140]. These background electrons will

Table 4.4: List of quality cuts for the partner electron used to reconstruct non-HFEs from Dalitz decay of neutral mesons and gamma conversion.

Cut	Cut-values
TPC clusters	80
TPC refit	Yes
$\|\eta\|$	0.8
p_T	0.5-10GeV/c
σ TPC PID	$\pm$ 3

be referred to as *photonic* electrons. The photonic electrons are produced in pairs of opposite charge ($\mathrm{e}^+\mathrm{e}^-$), and the calculated invariant mass of these pairs is very small. The photonic electrons can thus be identified and removed by using an invariant mass method [140] [145].

The invariant mass was calculated for electron pairs with opposite charge (unlike sign (ULS)) and like sign (LS) pairs, as seen in Figure 4.5. The LS distribution estimates the uncorrelated pairs, and subtracting these from the ULS pairs yields the number of electrons with a photonic partner [140]. In order to calculate the invariant mass distributions, each candidate from the inclusive electron sample was paired with other tracks (photonic partner electron candidates) in the same event. The partner electrons were selected with looser selection criteria compared to those of the inclusive electron sample in order to increase the efficiency of finding the photonic partners. The selection criteria for the partner electrons can be seen in Table 4.4. Any track in the inclusive electron sample with an ULS photonic partner yielding an invariant mass below 0.14 GeV/c^2 was removed from the selection, resulting in the *semi-inclusive* electron sample used in the correlation analysis.

4.3.4 Electron Selection Efficiency and Purity

The electron selection strategy applied in this analysis was tuned to provide a high purity electron and HFE sample, while at the same time keeping the efficiency as high as possible in order to exploit the limited statistics available in an optimal way.

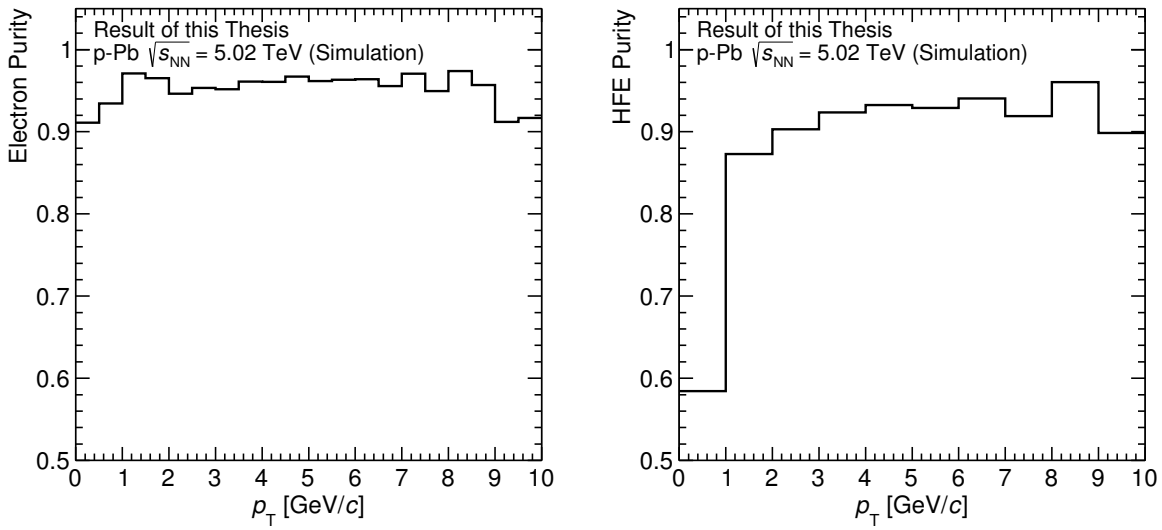

Figure 4.6: The calculated (left) electron purity and (right) heavy-flavour electron purity of the selected electron candidates, after the full selection procedure.

Electron Purity

The electron purity was extracted from Monte Carlo simulations, based on the ratio of the p_{T} distributions of contamination, i.e., any particles that were misidentified as electrons[7], and the total number of tracks after the full electron selection, in the following way:

$$Purity_e = 1 - \frac{N_{contamination}}{N_{tracks}}, \tag{4.1}$$

where $N_{contamination}$ is the number of tracks in a given p_{T}-bin (range) which are not electrons, and N_{tracks} is the total number of tracks.

The HFE purity was defined in a similar way, by taking the ratio of the p_{T} distribution of correctly identified HFE and that of the full selected sample:

$$Purity_{HFE} = \frac{N_{HFE}}{N_{tracks}}, \tag{4.2}$$

where N_{HFE} is the number of tracks in a given p_{T}-bin originating from charm or beauty decays. The p_{T} distributions of the electron purity and HFE purity is seen in

[7] After the electron sample has been selected by the same procedure as in the analysis run over data, the true identity of the particle is checked using the MC information.

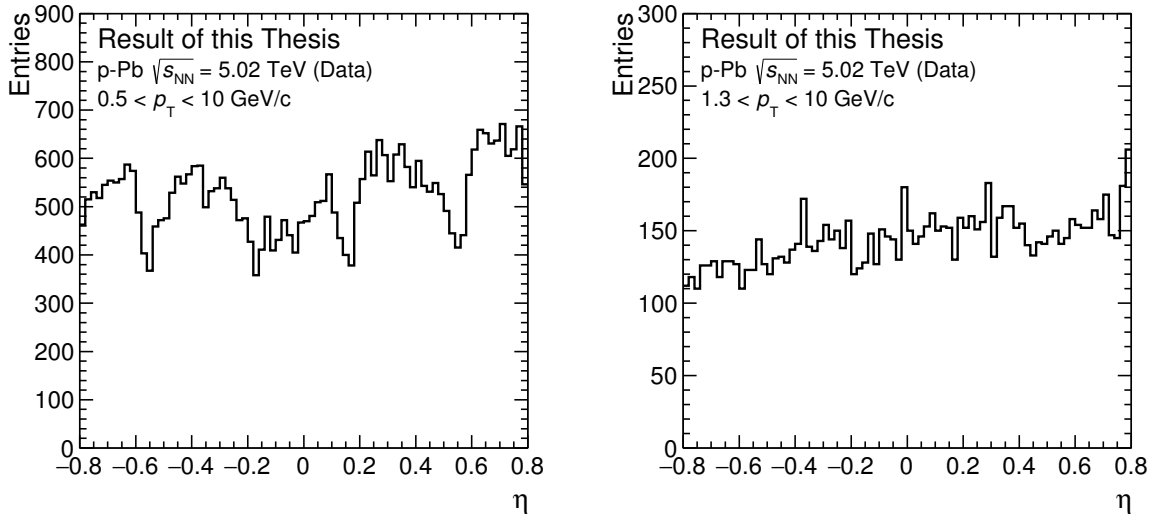

Figure 4.7: Pseudorapidity, η, distributions for the selected electron sample in the regions (left) 0.5 < p_{T} < 10 GeV/c and (right) 1.3 < p_{T} < 10 GeV/c. In the region below p_{T} = 1.3 GeV/c, a requirement of TOF matching is imposed, and a clear structure caused by the segmentation of the TOF detector into 5 segments in the beam direction is seen, indicating a loss of selection efficiency towards the edges of the detector segments. Above p_{T} = 1.3 GeV/c, TOF matching is no longer required, and a smoother distribution is observed. An increasing trend is observed from negative to positive η, due to the asymmetric p–Pb collision environment, where the proton arrives from positive η and the lead ion from negative η.

Figure 4.6. The electron purity was found to be above 95% for nearly the complete p_{T} range. A HFE purity higher than 88% was achieved for transverse momenta above 1 GeV/c.

Electron Efficiency

The efficiency of the electron selection depends on which detectors and cuts are used in the selection procedure. Tracks can be lost in several ways, e.g., due to inefficient regions of the detector, or poor track reconstruction or matching leading to the quality track cuts not being fulfilled. In the Figures 4.7 and 4.8, the number of selected electrons can be seen for various selection criteria, projected in the η and φ dimen-

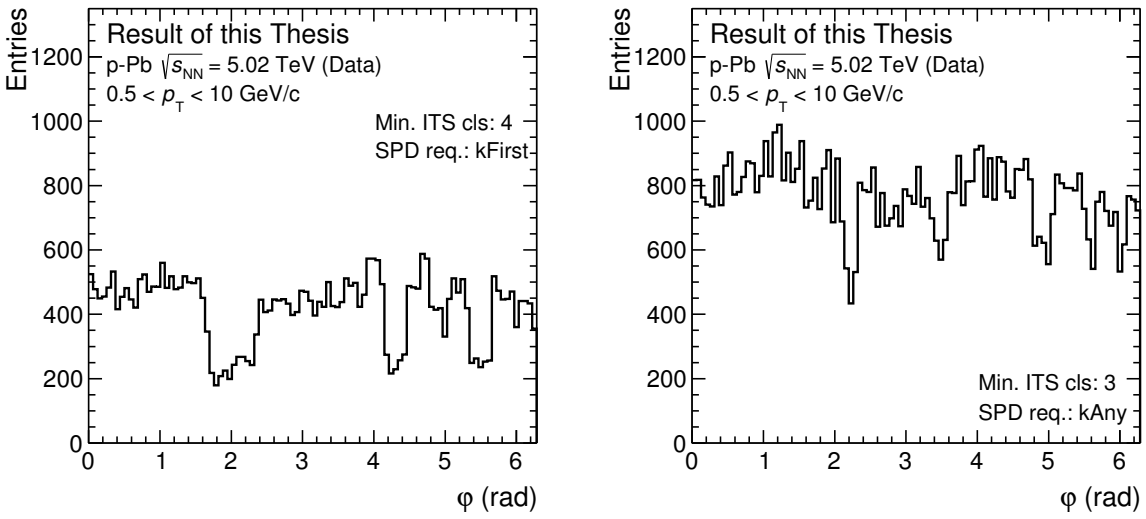

Figure 4.8: Azimuthal, φ, distributions for the selected electron sample. The left panel displays the ITS cut configuration used in the thesis, where 4 hits are required in the detector, and a hit in the first layer of the SPD is required (kFirst). The panel to the right shows the same distribution with less strict cuts, where only 3 hits are required in the ITS, and a hit must be registered in one of the two layers in the SPD. The well defined structures seen in the distribution produced with strict cuts are washed out to some degree in the case of looser cuts. A higher total number of entries is also observed for the scenario using looser cuts, indicating some loss of efficiency while tightening the ITS requirements.

sions respectively. In the left panel of Figure 4.7, which covers the full p_{T} range of electrons being studied in this analysis, distinct structures are seen in the distribution, indicating a loss of efficiency in certain regions. The right panel displays the same distribution with the lower p_{T} limit increased to 1.3 GeV/c, i.e., above the range where TOF matching is required. A much smoother distribution is observed, indicating that the structures are largely caused by the gaps between the five segments in the beam direction of the TOF modules. In Figure 4.8 structures are also observed, which are partly removed by applying a less strict selection in the ITS, as seen in Figure 4.8. The requirement of the track being registered in 4 layers of the ITS, with one hit being in the first layer of the SPD (left plot), was reduced to a requirement of 3 hits with one being in either of the two SPD layers (right plot). Efficiency maps were calcu-

lated for the appropriate electron selection strategy, and used to correct for selection inefficiencies.

The efficiency was calculated by running the electron selection procedure over a MC sample[8], and storing the particles along with their η, φ, Z-vertex position and p_{T} values at different stages of the selection. The particles stored at the generated level with only kinematic acceptance cuts applied were used as a reference, and the efficiency was calculated at various stages of the selection as the ratio of the distributions at the given stage and at the generated level. The *tracking efficiency* seen in the upper left panel of Figure 4.9, describes the selection efficiency after the quality track cuts have been applied. In the p_{T} region below 1.3 GeV/c the efficiency is limited by the TOF matching criterion, while for p_{T} above 3 GeV/c the efficiency is nearly flat in both p_{T} and η, at 60%. A peak is seen in the interval 1.3 < p_{T} < 3 GeV/c, related to the relatively loose cut of a minimum of 100 clusters in the TPC.

In order to study the efficiency of the PID selection by itself, the ratio of tracks remaining after the PID selection (including the quality track cuts), and after only the quality track cuts have been applied, was calculated, as seen in the upper right panel of Figure 4.9. A PID efficiency above 90% was achieved for p_{T} < 5 GeV/c, after which a rapid drops towards 50% at p_{T} = 10 GeV/c was observed. The drop in efficiency towards higher p_{T} is mainly caused by the intersection of the pion and electron $\mathrm{d}E/\mathrm{d}x$ bands (see Figure 3.7, page 62), and the removal of tracks fitting within $\pm 3\, n_{\sigma}^{\mathrm{TPC}}$ of the expected pion value, which is important in order to maintain a high electron purity as the p_{T} increases.

In the lower left panel of Figure 4.9, the combined efficiency after quality track cuts and PID is seen. As expected, an efficiency close to 60% was observed in the 1.3 < p_{T} < 5 GeV/c interval, followed by a decrease with a similar shape as the PID efficiency towards 30 %. A projection in p_{T} of the three efficiency stages is seen in the lower right panel of Figure 4.9, and the efficiency after the full selection, including the invariant mass cut has been added for reference. An invariant mass cut efficiency of 80% was observed at the lower p_{T} range, increasing rapidly to 95% at $p_{\mathrm{T}} \simeq 1.5$ GeV/c, slowly increasing towards 98% at p_{T}= 10 GeV/c.

The efficiency correction for electrons was applied at the PID stage, and not after the full selection including the invariant mass cut. While the electron efficiency after the full selection can be calculated, as presented here, the efficiency correction for the invariant mass cut should rather correct for the efficiency of the non-HFE selection, given that the cut was implemented to remove non-HFE from the HFE sample. Cor-

[8] See Appendix A.2 for details on the Monte Carlo sample used.

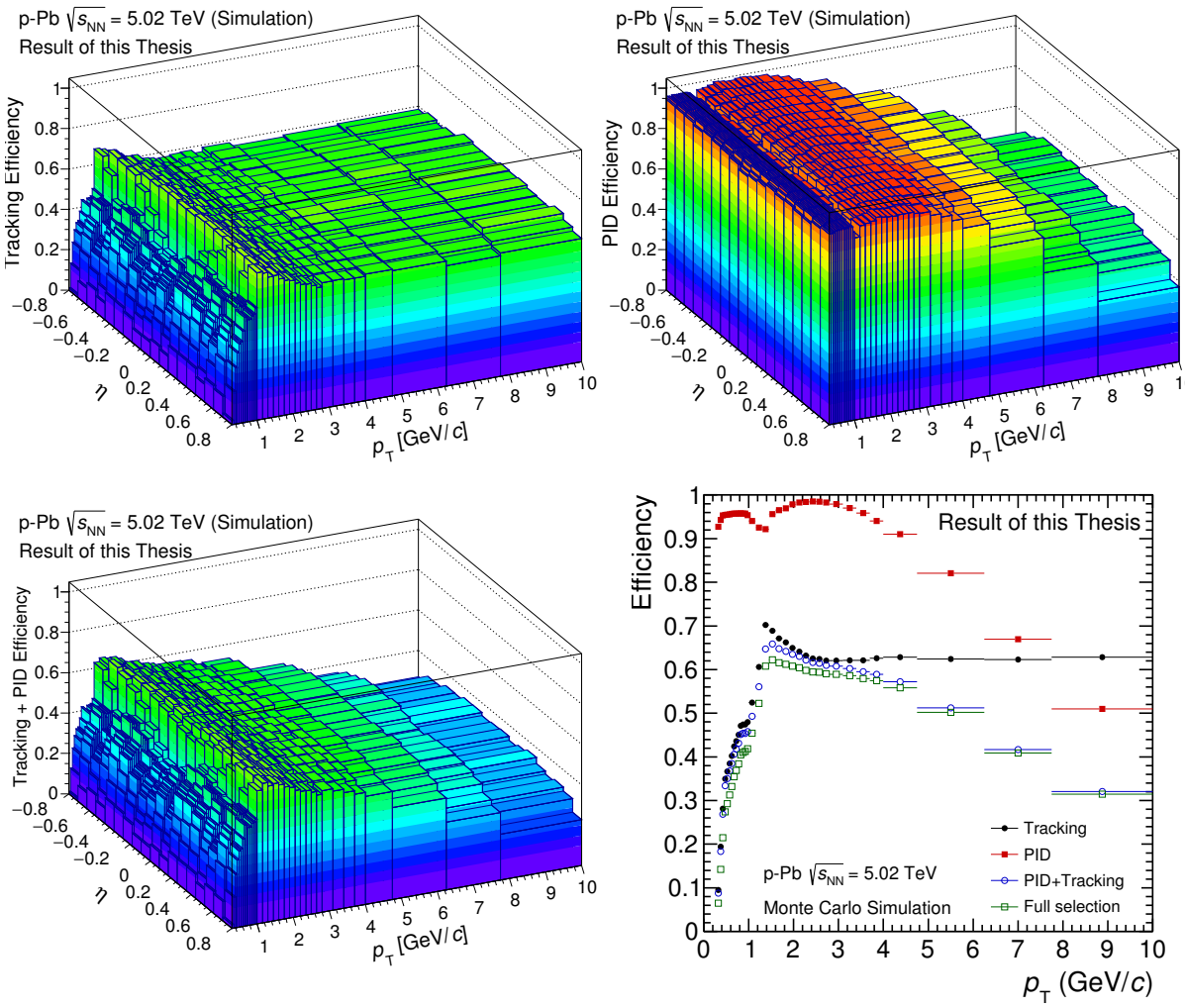

Figure 4.9: Efficiency at various stages of the electron selection as a function of pseudorapidity, η, and transverse momentum, p_{T}. The upper left panel displays the tracking efficiency, the upper right plot shows the PID efficiency, while the efficiency after both tracking and PID is seen in the lower left plot. Projections in p_{T} of the efficiencies at various stages can be seen in the lower right plot, where also the efficiency after the full selection, i.e., after tracking, PID and the invariant mass cut has been applied, is displayed.

rections of this type have been performed for other HFE analyses, e.g., the measurement of azimuthal angular correlations between heavy-flavour decay electrons and charged hadrons in pp collisions at $\sqrt{s} = 2.76\,\mathrm{TeV}$ in ALICE [146], but as discussed

in the study of correlations between D^0-HFE in pp collisions [18], such corrections are not feasible for the D^0-HFE analysis with the currently available statistics. A correlation distribution between D^0 mesons and the unlike sign electron sample is required in the process, which would lead to a large statistical error of the correction due to the limited statistics available.

4.3.5 Electron Selection Strategies

Due to the relatively low statistics available in the p–Pb data sample from 2013, alternative selection strategies were studied in order to increase the efficiency of the electron selection compared to that of the analysis performed in 2010 pp collisions [18], complementary to this analysis, while maintaining the high purity of the electron and HFE sample. Two of the factors found to reduce the electron selection efficiency most significantly were the strict n_σ^{TPC} cut of the electron PID, and the limited track matching efficiency to the TOF detector. In addition to these parameters, the quality track cuts of the TPC were tuned, and a minor adjustment was made in the invariant mass cut.

A brief summary presenting the differences from the strategy used in the pp analysis and the strategy found to be the ideal compromise between purity and efficiency in the p–Pb analysis, will be presented in this section, along with comparisons of the performance of these strategies. Each strategy has been given a numerical identifier consisting of three digits, in the form 'Strategy-XYZ', where 'X' denotes the PID strategy, 'Y' includes variations related to tracking in the TPC, and 'Z' relates to the upper limit of the invariant mass cut for unlike sign pairs of electron candidates. The strategy used in the pp analysis is *Strategy-000*, while the new strategy used in the p–Pb analysis is *Strategy-712*. A list of differences between the two strategies is presented in Table 4.5.

Efficiency of the TPC PID of Electrons

The electron PID efficiency of the TPC depends on the size of the band defined by a given number of sigmas, n_σ^{TPC} around the expected $\mathrm{d}E/\mathrm{d}x$[9] of electrons in which tracks are accepted. The upper limit of the band is commonly set to 3 n_σ^{TPC}, ensuring that most of the electrons are included. The lower bound requires more attention, as the electron and pion bands are close to each other in this region, which can cause

[9] The bands of various particles can be seen in Figure 3.7, page 62.

Table 4.5: Variations of selection requirements for a variety of electron selection strategies. The strategies are labeled as 'Strategy-XYZ', where 'X' denotes the PID strategy, 'Y' includes variations related to tracking in the TPC, and 'Z' relates to the upper limit of the invariant mass cut for unlike sign pairs of electron candidates. A subset of the considered selection strategies are presented, while the numbering is kept as in the analysis code, for reference; thus the numbering of the variations do not appear sequential.

	X		Y		Z	
Variation	0	7	0	1	0	2
TPC PID, electron	-1 < n_σ^{TPC} < 3	-3 < n_σ^{TPC} < 3	-	-	-	-
TOF-matching	p < 2.0	p < 1.3 GeV/c	-	-	-	-
e-PID, TOF	p < 2.0	p < 2.0 GeV/c	-	-	-	-
π rejection, $\pm 3\ n_\sigma^{\mathrm{TPC}}$	-	p > 1.0 GeV/c	-	-	-	-
p rejection, $\pm 3\ n_\sigma^{\mathrm{TPC}}$	-	1.3 < p < 2.0 GeV/c	-	-	-	-
TPC clusters	-	-	120	100	-	-
TPC cluster ratio	-	-	0.8	0.6	-	-
Invariant Mass (GeV/c^2)	-	-	-	-	0.15	0.14

contamination if a value of -3 n_σ^{TPC} is used. A comparison of the PID efficiency, where only the TPC PID for electrons has been applied, is seen in Figure 4.10 for the two ranges $\pm 3\ n_\sigma^{\mathrm{TPC}}$ and -1 < n_σ^{TPC} < 3. As expected from the definition of standard deviations, a selection efficiency close to 100 % was observed while using the $\pm 3\ n_\sigma^{\mathrm{TPC}}$ band, while an efficiency of 84 % was found for the tighter cut. A constant ratio of approximately 84 % was found between the efficiency of the two scenarios, as indicated by the lower panel of the figure. A large portion of the electrons can thus be conserved by applying a looser cut, given that the pion contamination can be dealt with in a more efficient way. In Strategy-7YZ, pions were identified and removed by a ± 3 n_σ^{TPC} band around the expected $\mathrm{d}E/\mathrm{d}x$ value of pions.

Efficiency of the TOF Track Matching

In order to apply the TOF PID selection, the reconstructed track has to be successfully matched with a track in the TOF detector. The TOF matching efficiency for the 2013 p–Pb collisions is seen in Figure 4.11. A very low efficiency is observed at low p_{T}, while in the region of interest for this analysis the matching efficiency rises gradually from 70% at p_{T} = 1GeV/c, to 80% at p_{T} = 5GeV/c. The common implementation of

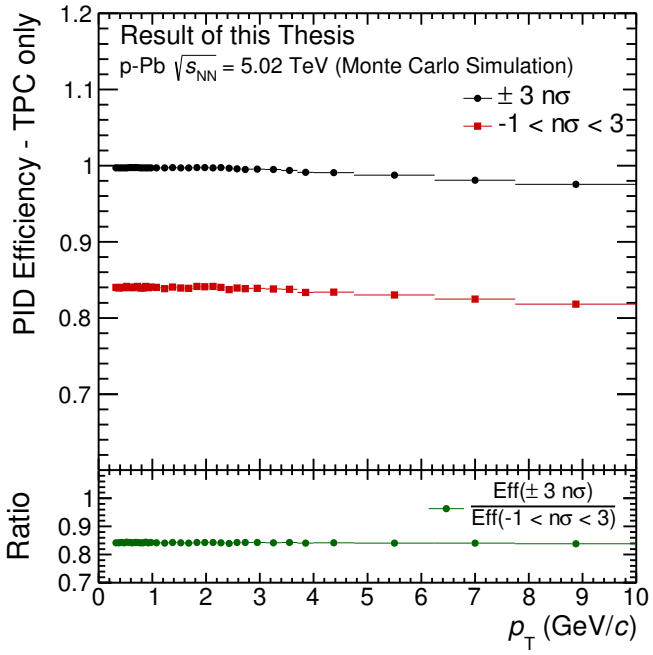

Figure 4.10: Efficiency of the TPC PID for electrons. Two cut variables on the number of sigma deviation from the expected $\mathrm{d}E/\mathrm{d}x$ of electrons are shown, ($\pm$ 3 nσ) and (-1 < nσ < 3), used in Strategy-7YZ and Strategy-0YZ respectively. The lower panel shows the ratio of the two scenarios, found to be constant at approximately 84%.

the TOF PID procedure is to require TOF matching for all tracks within the p_{T} region where TOF PID is used, to avoid that tracks without TOF matching pass through the TOF PID unfiltered. Both Strategy-000 and Strategy-712 apply TOF PID up to p_{T} = 2 GeV/c, but in order to reduce the impact of the limited TOF matching efficiency, the TOF matching requirement was removed in the interval 1.3 < p < 2.0 GeV/c in Strategy-712. The removal of this requirement leads to electrons and contamination tracks without TOF matching to pass the selection, increasing the background in the sample. The main contribution of contamination in this p_{T} interval was found to be protons, which had to be removed by another approach in order to keep a high electron purity. In Strategy-7YZ, protons were identified and removed by a $\pm 3\ n_{\sigma}^{\mathrm{TPC}}$ band around the expected $\mathrm{d}E/\mathrm{d}x$ value of protons.

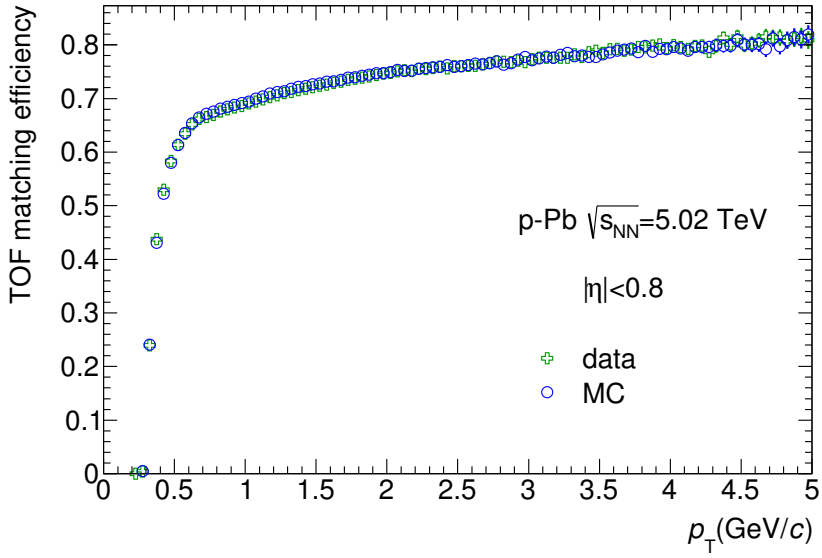

Figure 4.11: Matching efficiency (including the geometric acceptance factor) at TOF for tracks reconstructed in the TPC in p–Pb collisions at $\sqrt{s_{\mathrm{NN}}} = 5.02\,\mathrm{TeV}$, compared to Monte Carlo simulation. Figure and caption from [126].

Evaluation of the Selection Strategies

The most drastic change of the electron selection strategy was the change in PID, aiming to address the efficiency loss in the TPC and TOF procedures. A comparison of Strategy-000 and Strategy-700 is seen in Figure 4.12. The efficiency after quality track cuts is seen in the panel to the left, and the efficiency of the PID procedure to the right. The tracking efficiency was found to increase by up to a factor 1.5 in the interval $1 < p_{\mathrm{T}} < 2$, due to the removal of the TOF matching requirement in Strategy-700[10]. The PID efficiency for Strategy-700 was found to improve by a factor of 1.2 compared to Strategy-000, for $p_{\mathrm{T}} < 4\ \mathrm{GeV}/c$, after which the efficiency rapidly drops towards higher p_{T} due to the pion rejection cut removing electrons as the two bands approach each other. The efficiency after the full selection, i.e., after the quality track cuts, PID and invariant mass cut has been imposed, is summarized for the different strategies

[10] The TOF matching criterion is applied based on the momentum, p, while the transverse momentum, p_{T}, is used as a selection cut for the candidates, and thus also used for the representation of the efficiency. As a result, the increase in efficiency caused by the cut-off for the TOF matching requirement is not observed as a sharp increase at p_{T}=1.3 GeV/c, but appears somewhat smudged.

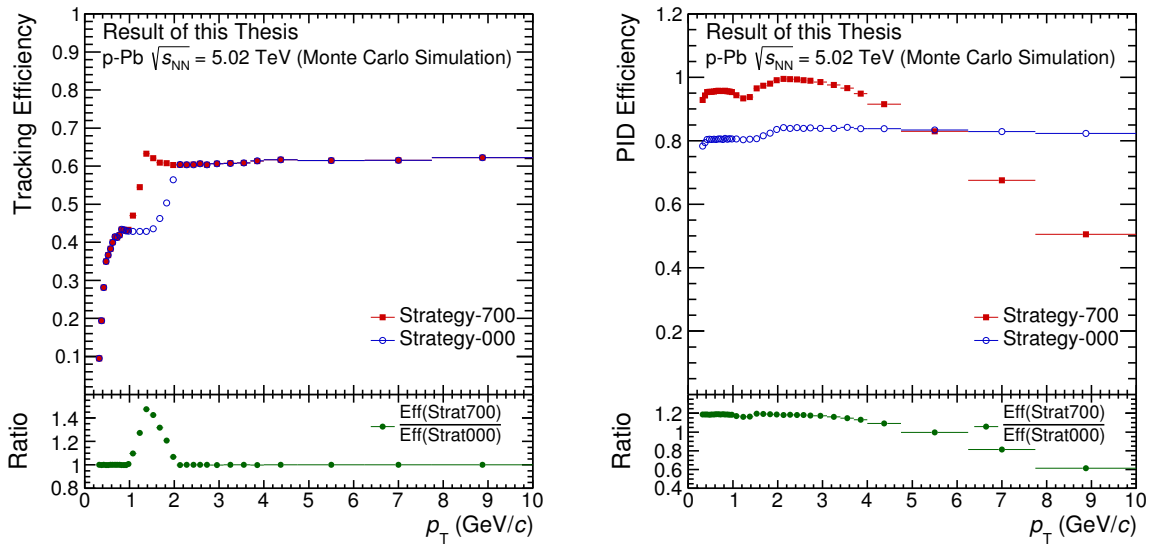

Figure 4.12: Comparison of (left) tracking and (right) PID efficiencies for Strategy-700 and Strategy-000 of the electron selection. The change in tracking efficiency is caused by different p_{T} regions where TOF matching is applied, while the differences in PID efficiency results from changes in the PID strategies.

at the end of the section, in Figure 4.15. A maximum increase in efficiency of factor 1.7 in Strategy-700 compared to Strategy-000 was found around p_{T}=1.5 GeV/c, while a nearly constant increase of factor 1.2 was observed up to p_{T}=4 GeV/c, which agrees well with the observations from the PID and tracking efficiencies.

The second set of changes, related to the tracking in the TPC, was compared by studying the differences in tracking efficiency for Strategy-712 and Strategy-700, as seen in Figure 4.13. Strategy-712 requires a minimum of 100 registered clusters hit for a given track in the TPC, in addition to a ratio of the *found over findable* number of clusters of 0.6[11]. In Strategy-700, a stricter selection of a minimum of 120 clusters and a ratio of 0.8 was required. A deviation of the two strategies was observed in the 0.7 < p_{T} < 3.0 GeV/c region, increasing by a maximum ratio of 1.1 in the case of Strategy-712. The effect of the looser cut was mainly observed for low p_{T} tracks as

[11] The found over findable ratio is calculated as the number of clusters associated with a track, divided by the total number of potentially findable clusters, where the number of findable clusters is limited by various factors, e.g., that tracks may pass through dead zones of detectors or outside the acceptance.

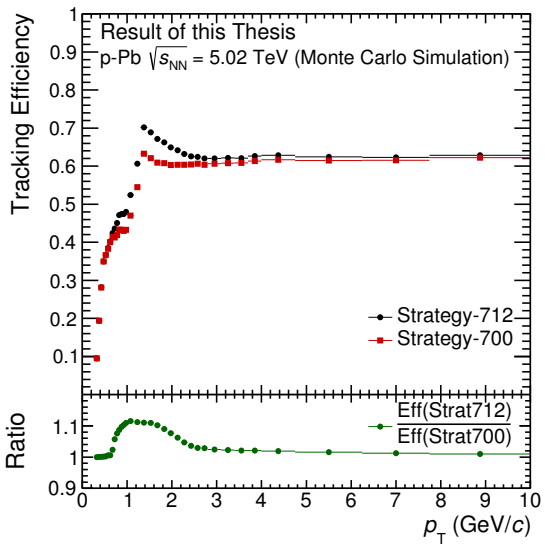

Figure 4.13: Comparison of tracking efficiencies for the electron selection using Strategy-712 and Strategy-700. The two strategies vary with respect to the cluster requirements of the TPC, with Strategy-712 imposing less strict cuts, allowing more electrons to pass the selection. Mainly low p_{T} tracks are effected by this change, as they are bent more in the magnetic field, and thus are more likely to cross the dead region between two sectors, resulting in fewer registered clusters for the track.

these are bent more in the magnetic field compared to those with higher p_{T}, and thus are more likely to pass regions in between two sectors, where there are no clusters, resulting in fewer registered cluster hits for these tracks.

The final change in electron selection strategy was related to the invariant mass cut of unlike-sign pairs, as discussed in Section 4.3.3. A minor adjustment was made from a cut value of 0.15 GeV/c^2, to 0.14 GeV/c^2, a value which was also used for the measurement of electrons from heavy-flavour hadron decays in p–Pb collisions at ALICE [140]. A comparison of the purity and HFE purity with and without the invariant mass cut implemented, is presented in Figure 4.14, displaying an increase in HFE purity, particularly at the low end of the p_{T} range. A maximum increase in efficiency of 2% was observed after applying the looser cut.

Figure 4.15 presents a summary of the change in efficiency and purity of the electron selection, caused by changing the various parameters discussed in this section. Strategy-712 was found to provide a significant increase in efficiency over Strategy-

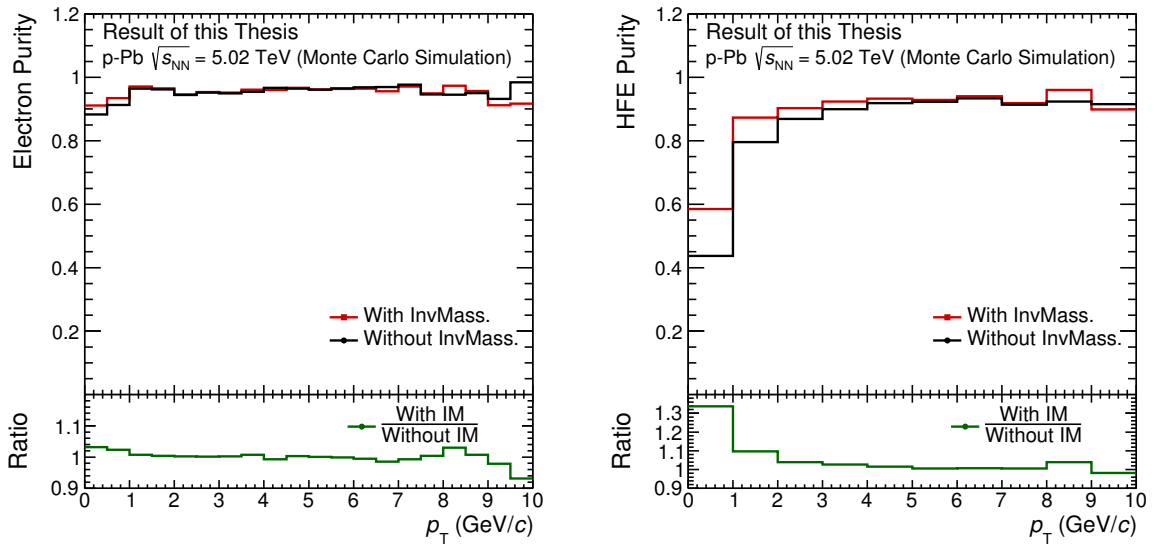

Figure 4.14: The (left) electron and (right) heavy-flavour electron purity with and without the removal of background by the invariant mass cut. Little change is observed in the electron purity, while an improvement in the HFE purity is observed when applying the cut, especially at the low end of the p_{T} range.

000, resulting in ∼40% more tracks in the $0.5 < p_{\mathrm{T}}^{\mathrm{e}} < 5$ GeV/c interval, while obtaining a high purity heavy-flavour electron sample. A stricter selection was chosen above p_{T} = 5 GeV/c compared to Strategy-000 in order to maintain the high purity in up to p_{T} = 10 GeV/c, allowing for an extension of the usable p_{T} range at the cost of lower efficiency in this region. A comparison of the final D^0-e correlation distributions using electrons selected by Strategy-000 and Strategy-712 is presented in Section 6.1.

In addition to the adjustments of the strategies discussed in this section, an increased selection efficiency in the 2013 data sample from p–Pb collisions compared to that of data samples from 2010 and 2011 has been observed as a consequence of reductions of gaps in the ITS acceptance. In 2010 and 2011 the two innermost SPD layers had up to 20% and 30% inactive modules, respectively, which was reduced to ∼5% in 2012 after solving problems with detector cooling [126]. The improvement in ITS acceptance led to improved ITS-TPC track reconstruction, and an increase in efficiency by 10 percent points was observed for 2013 p–Pb compared to 2010 pp, using identical selection strategies.

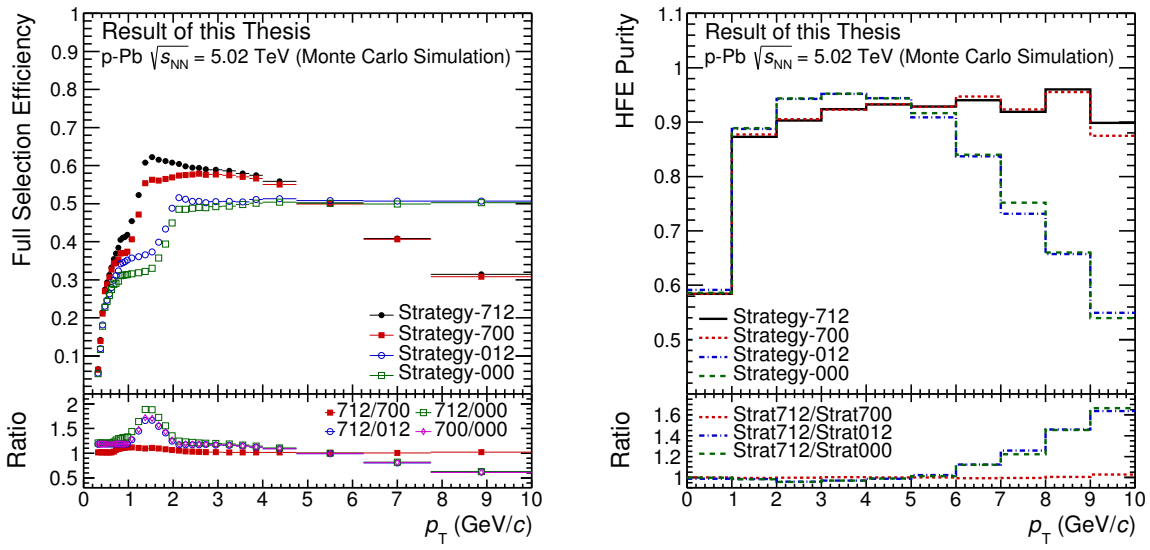

Figure 4.15: (Left) Comparison of the full electron selection efficiency for the strategies described in this section, along with (right) a comparison of the resulting heavy-flavour electron purities.

Chapter 5

Azimuthal Angular D^0-e Correlations

This chapter will focus on the strategy and stages of the azimuthal angular correlation analysis of the D^0 meson and heavy-flavour electron candidates, selected by the procedure discussed in Chapter 4. Section 5.1 begins with the calculation of raw correlation distributions, and follows the analysis to the final extraction of the associated yield and sigma by fitting the corrected correlation distributions. In Section 5.2, a study of the analysis over simulated data is presented.

5.1 Analysis Strategy

The analysis strategy can be divided into five main parts, as discussed in the following, namely:

1. Correlation of trigger and associated particles to produce the raw correlation distribution.

2. Correction for acceptance and detector inhomogeneity by the event mixing method.

3. Subtraction of background correlations by the sideband subtraction method.

4. Correction of trigger and associated particle selection inefficiencies.

5. Extraction of particle yields by fitting of the projected azimuthal angular correlation distributions.

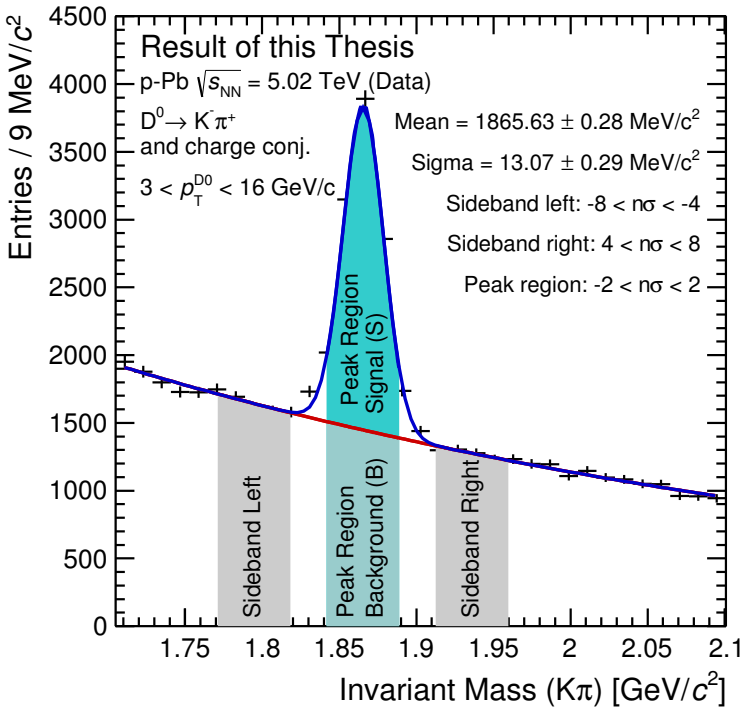

Figure 5.1: Invariant mass distribution of D^0 meson candidates in the interval $3 < p_{\mathrm{T}}^{\mathrm{D}^0} < 16\ \mathrm{GeV}/c$. The peak and sideband regions have been marked, and a division of the peak region into the signal (S) and background (B) component can be seen.

5.1.1 Raw Correlation Distribution

The correlation distributions were built by correlating trigger particles with associated particles, which in this analysis are D^0 mesons and HFE, respectively. The selection procedure for these candidate particles is described in detail in Chapter 4. The trigger and associated particles were selected on a per event basis, and relevant information was stored for each particle, such as the transverse momentum, p_{T}, azimuthal angle, φ and pseudorapidity, η. When a trigger and associate particle candidate[1] are selected within the same event (SE), the difference in φ and η of each

[1] More than one trigger or associated particle can be selected in a single event, in which case each trigger candidate will be correlated with each associated particle candidate.

pair is calculated as $\Delta\varphi = \varphi^{trig} - \varphi^{assoc}$, and $\Delta\eta = \eta^{trig} - \eta^{assoc}$, where *trig* and *assoc* denotes the trigger and associate particle candidate respectively. This process is repeated for all the available events, followed by filling a histogram with the $\Delta\eta, \Delta\varphi$ distribution, for the desired p_{T} ranges of the particle candidates. The correlation distribution is separated into two parts, the peak and sideband (SB) regions, based on the invariant mass of the D^0 meson candidate. A Gaussian fit is applied to the invariant mass, M, of all selected D^0 candidates, and the peak, μ, and width, σ, of the fit is extracted. The peak region is defined to contain D^0 candidates within the range $|M - \mu| < 2\sigma$, and the sideband region is defined to contain D^0 candidates within the range $4\sigma < |M - \mu| < 8$. The different regions are illustrated in the example of an invariant mass distribution shown in Figure 5.1.

5.1.2 Correction of Acceptance and Detector Inhomogeneity

The correlation distribution is susceptible to effects caused by the limited detector acceptance and spatial inhomogeneities, which was corrected for by using the *event mixing* technique. The trigger candidates found in a given event were correlated to the associated particles of other events with similar multiplicity and position of the primary vertex along the beam axis (Zvertex), which was achieved by assigning the particles to *pools* defined by given intervals of these variables, as seen along with other pool settings in Table 5.1. The event mixing procedure was performed in two stages, an online and an offline part. The online component was performed while running the analysis task, which requires large computing resources and was done on the Grid. The offline component of the analysis includes the post processing done on a local machine, e.g., the extraction of correlation distributions from the output files produced online. While running the analysis online, both a Same Event (SE) and Mixed Event (ME) analysis was run simultaneously. In the SE analysis, selected trigger and associated particle candidates within the same event were correlated, and assigned to a pool bin according to the Zvertex and multiplicity of the event. In the Mixed Event (ME) sample, an *event pool* was created for each of the pool bins, and filled by the events preceding a selected trigger particle (D^0 meson) candidate. When a trigger candidate was found, the correlation analysis was performed on the mixed events if the conditions of Table 5.1 were fulfilled. While running the analysis, the data sample was split into several smaller parts (subjobs), and distributed on the Worldwide LHC Computing Grid (WLCG) for efficient processing. The limited data available to each subjob determines the number of events available for filling

Table 5.1: Summary of the configuration for the mixed event corrections. The upper two entries defines the dimensions of the pool bins, while the lower four define the requirements related to the minimum number of events or tracks required in a pool for the event mixing to be performed, or the maximum number of entries a pool can hold before refreshing.

Pool variable	Value
Zvertex bins [cm]	(-10, -2.5), (-2.5, 2.5), (2.5 - 10)
Multiplicity bins	(0, 50), (50, 500)
Min. #events in pool	1
Max. #events in pool	200
Min. #tracks in pool	25
Max. #tracks in pool	10000

the event mixing pools, as information can not be shared between the subjobs. The amount of data processed by each subjob was limited by memory restrictions of the machines running the analysis, and the pool configuration was tuned to perform optimally within these limitations. The output from the SE and ME analyses were stored, and the correction itself was performed locally during the correlation distribution extraction. The mixed event distributions were calculated, and corrected for, in each separate pool bin. The introduction of corrections in separate pool bins, in contrast to computing a mixed event distribution integrated for all pool bins, combined with the optimization of event pools by tuning the data of the subjobs, were found to reduce fluctuations of the final correlation distributions. The resulting distribution from the mixed events (ME) shows a triangular shape as a function of $\Delta\eta$, due to the limited η coverage of the detector, while a nearly flat distribution is observed in $\Delta\varphi$, as seen in the middle row of Figure 5.2. The ME-distribution was rescaled by its average value in the range ($-\frac{\pi}{8} < \Delta\varphi < \frac{\pi}{8},\ -0.2 < \Delta\eta < 0.2$), i.e., the 4 bins closest to ($\Delta\eta, \Delta\varphi$)=(0,0), as the maximum efficiency for the particle pairs is located at these coordinates. The ME-corrected correlation distributions, $\frac{dN^{corr}(\Delta\eta,\Delta\varphi)}{d\Delta\eta\, d\Delta\varphi}$, were obtained by dividing the SE distribution by the normalized ME distribution [18]:

$$\frac{dN^{MEcorr}(\Delta\eta,\Delta\varphi)}{d\Delta\eta\, d\Delta\varphi} = \frac{\frac{dN^{SE}(\Delta\eta,\Delta\varphi)}{d\Delta\eta\, d\Delta\varphi}}{\frac{dN^{ME}(\Delta\eta,\Delta\varphi)}{d\Delta\eta\, d\Delta\varphi}} \frac{dN^{ME}(0,\ 0)}{d\Delta\eta\, d\Delta\varphi}. \tag{5.1}$$

An example of correlation distributions for the SE, normalized ME, and SE corrected for ME cases can be seen in the upper, middle and lower rows of Figure 5.2 respectively, for the signal region (left) and sideband region (right). The upper row shows the raw correlation distributions for the two regions, while the bottom row displays the correlations after the mixed event correction has been applied. An increase in entries for the less efficient bins was found in the corrected distributions.

As was the case for the D^0-HFE correlation analysis performed in pp collisions at $\sqrt{s_{\mathrm{NN}}} = 7\,\mathrm{TeV}$ [18], the statistics of the data sample was found to be a major challenge in the correlation analysis in p–Pb collisions at $\sqrt{s_{\mathrm{NN}}} = 5.02\,\mathrm{TeV}$, which becomes evident when studying the correlation distributions as a function of both $\Delta\eta$ and $\Delta\varphi$, as seen in Figure 5.2. A more convenient way of presenting the distributions is thus to project them in the $\Delta\varphi$ dimension, which will be done for the remainder of the thesis. A comparison of the ME-corrected peak and sideband region, projected in $\Delta\varphi$ and normalized to the number of trigger particles[2], is presented in the left panel of Figure 5.3.

5.1.3 Sideband Subtraction

The peak region of the invariant mass distribution contains both a signal (S) and background (B) region, as seen in Figure 5.1. The background region contains combinatorial background (particles misidentified as D^0 mesons), which has to be removed to in order to study the signal by itself. The correlation distribution of the sideband region was normalized to the distribution of the background in the peak region, and subtracted from the peak region correlation distribution. The azimuthal angular correlation distribution before and after the sideband subtraction method was implemented is seen in Figure 5.3. Large fluctuations and statistical uncertainties are observed in both the peak and sideband correlations, causing also the sideband subtracted peak region correlations to suffer from the same effects. Indications of a near side peak can be observed, and a weak increase in the central away side bin, $\Delta\varphi = \pi$, can be seen, though it is still compatible with the surrounding bins within uncertainties, and no obvious conclusions can be drawn. The shapes of the peak- and sideband region correlation distributions were observed to exhibit similar shapes, which to some degree can be attributed to the matching of one true D^0 daughter with a non-D^0 daughter, in

[2] The normalization to the number of trigger particles is done by scaling the distribution by $1/N_{D0}$, where N_{D0} is the number of trigger particles extracted from the invariant mass plot in the peak region after background subtraction.

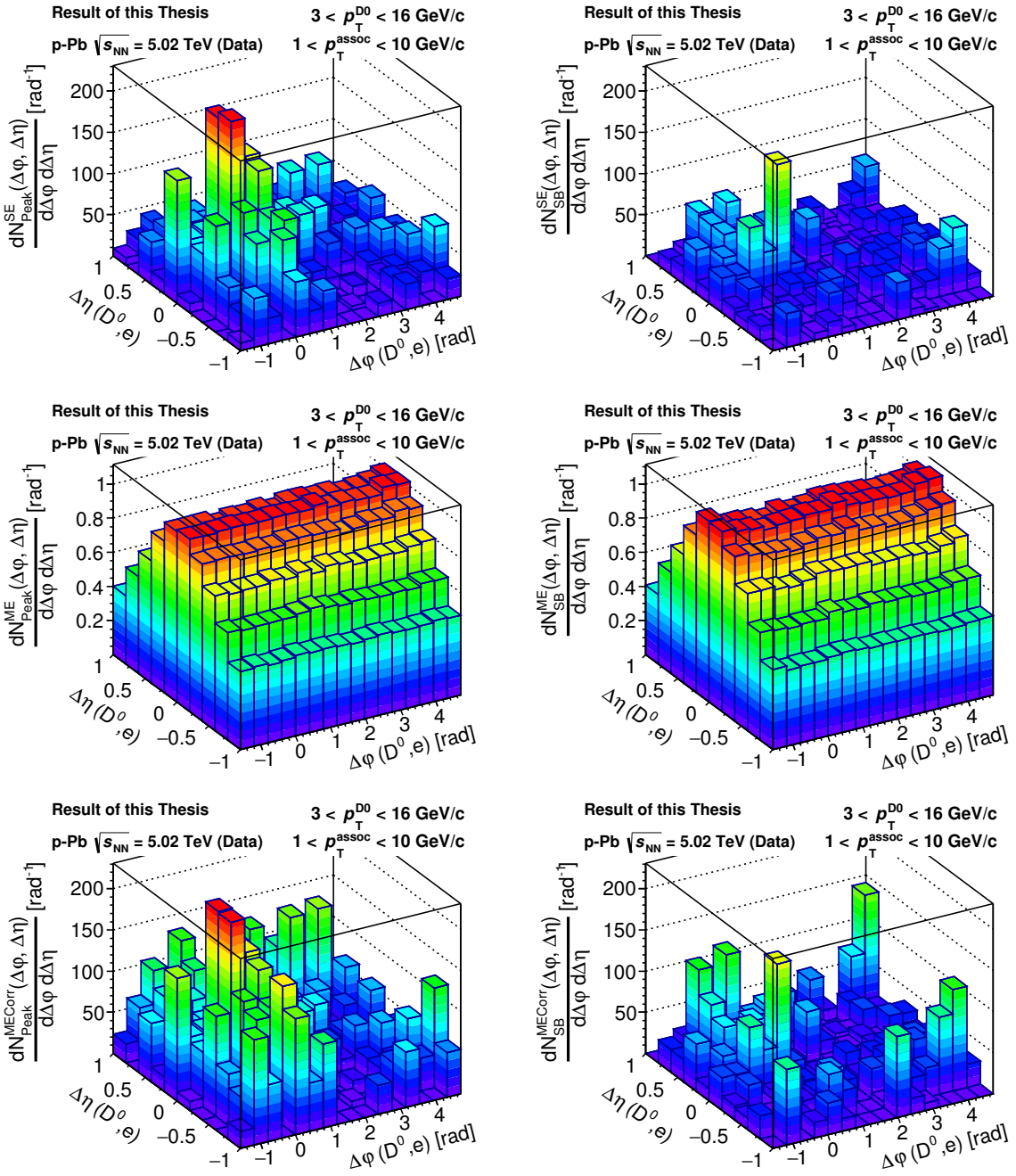

Figure 5.2: Example correlation distributions in the (left column) peak region and (right column) sideband region, (top row) before and (bottom row) after the event mixing correction. The middle row shows the mixed event correlations, normalized to the 4 points closest to $(\Delta\eta\Delta\varphi) = (0,0)$, and is seen to have a triangular shape in $\Delta\eta$ and a nearly flat shape in $\Delta\varphi$. While the number of entries remain mostly unchanged close to $(\Delta\eta\Delta\varphi) = (0,0)$, expected to be the most efficient region, the correction result in more entries at the outer regions of $\Delta\eta$. The mixed event correction is performed for each pool bin, but the example figures display the integrated entries from all bins.

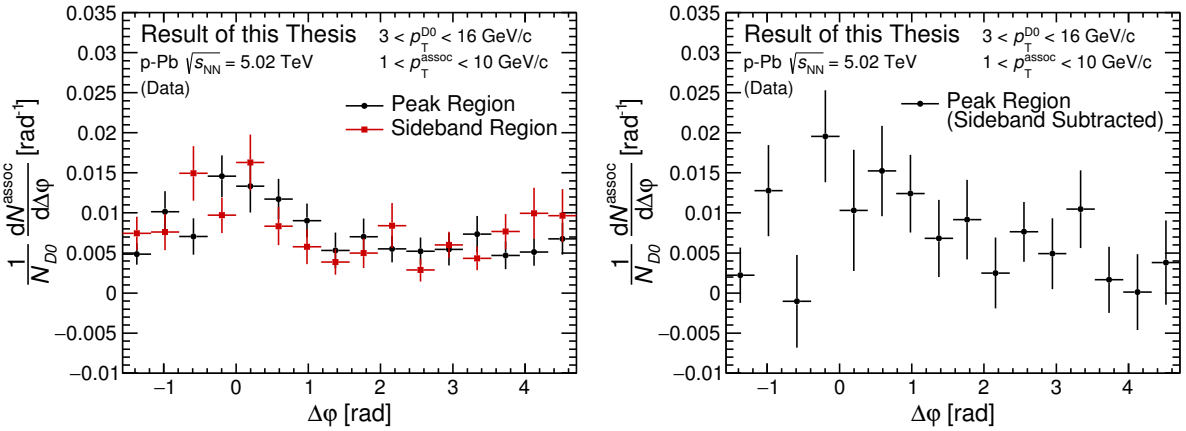

Figure 5.3: (Left) Correlation distributions of the peak and sideband regions, and (right) correlation distribution of the peak region after the sideband correlations have been subtracted. The subtraction procedure is performed in order to remove background correlations, leaving only the signal.

which case the fake reconstructed D^0 candidate is likely to have a similar kinematics as the proper D^0 meson, and correlating it with a correctly identified HFE would result in a similar shape as for a real D^0-e pair. An hint of an enhancement in the bins to the right of $\Delta\varphi$=π was observed for the sideband correlation distribution, but also in this case the variation was found to remain compatible with the baseline.

Reflection of Correlation Distributions

The large statistical fluctuations observed for the sideband subtracted distribution were reduced by exploiting the symmetry of the correlations around $\Delta\varphi$ = 0 and $\Delta\varphi$ = π, as seen in the remaining plots of correlations in $\Delta\varphi$ in this thesis. *Reflected* plots were produced by mirroring the data points to the left of $\Delta\varphi$ = 0 onto the data points to the right of $\Delta\varphi$ = 0, and similarly, the data points to the right of $\Delta\varphi$ = π were mirrored onto the data points to the left of $\Delta\varphi$ = π[3]. The resulting distribution was scaled by a factor 0.5 to correct for the summation of two and two bins.

[3] To clarify, in the case of this analysis, where 16 bins are defined in $\Delta\varphi$ from -$\frac{\pi}{2}$ to 3$\frac{\pi}{2}$, the following bins were combined, with the resulting 8 bins ordered as they appear here: [4,5], [3,6], [2,7], [1,8], [9,16], [10,15], [11,14], [12,13].

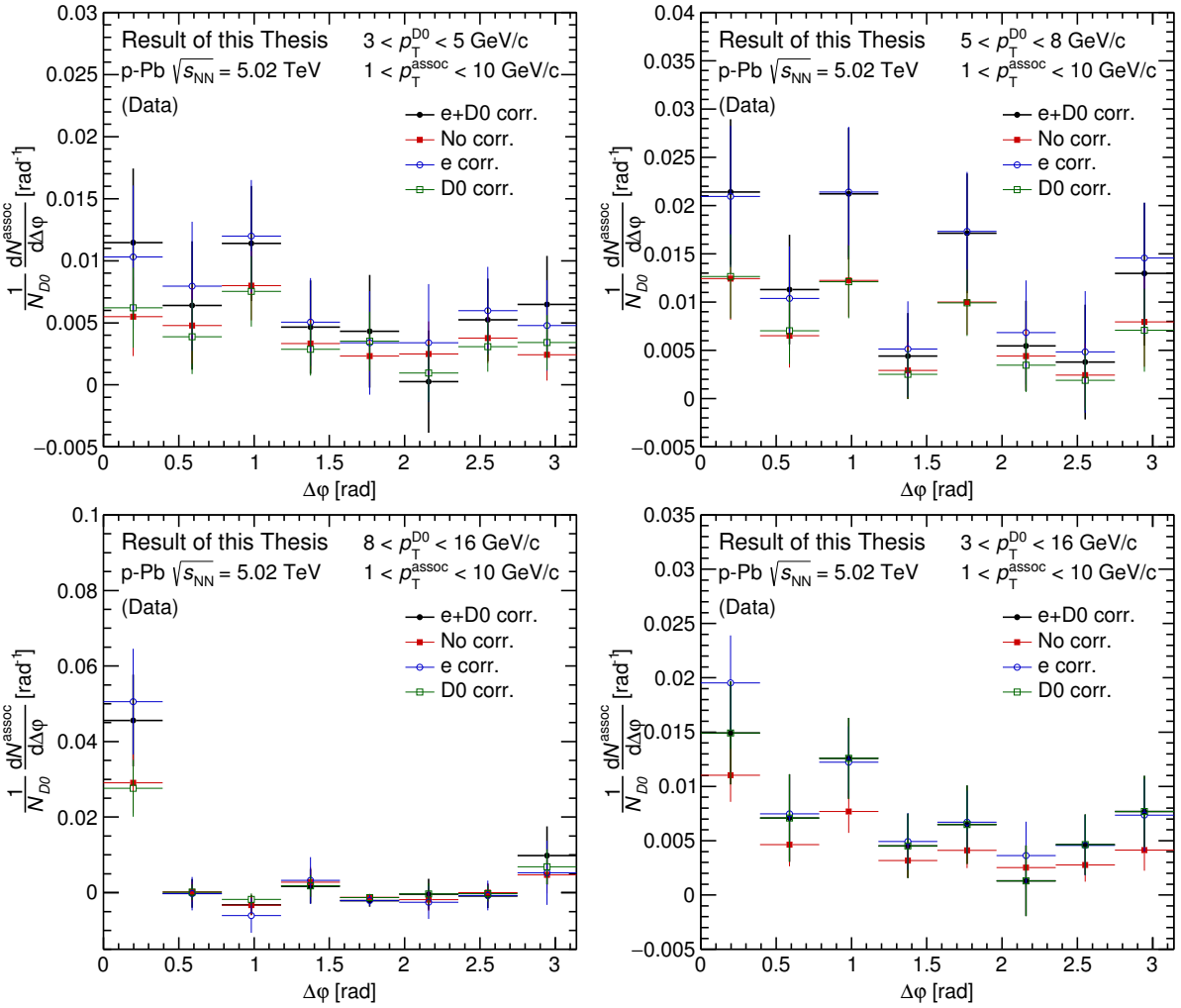

Figure 5.4: Correlation distributions after the mixed event correction and sideband subtraction, normalized to the number of trigger particles. Four different intervals of $p_T^{D^0}$ are presented, all covering the full p_T range considered for electrons in this thesis. The different lines indicate the correction of various combinations of selection efficiencies.

5.1.4 Selection Efficiency Corrections

The limited reconstruction efficiency of the trigger and associated particle was corrected for by applying the inverse of a weight, w, to each pair of trigger and associated particles, calculated as $w = \mathit{eff}_{trig}(p_{\mathrm{T}},\ mult) \times \mathit{eff}_{assoc}(p_{\mathrm{T}},\ \mathrm{Zvertex},\ \eta)$, where eff_{trig} and eff_{assoc} are the selection efficiencies of the trigger and associated particles, respectively. In the case of the trigger, the efficiency depends on the multiplicity and p_{T}, while for the associated particle the efficiency was extracted based on the particle p_{T}, its pseudorapidity, η, and its position on the z-coordinate of the primary vertex, $\mathrm{Zvertex}$. The details of the efficiency calculations are discussed in detail in Chapter 4.

A comparison of the azimuthal angular correlation distributions before and after the trigger and associated particle efficiency corrections have been applied can be seen in Figure 5.4, for various p_{T} regions of the trigger particle. A general increase in the yields was observed for the efficiency corrected distributions, compared to the uncorrected distributions, though the results of all variations presented in Figure 5.4 agree within uncertainties of each other, for the majority of the $\Delta\varphi$ bins. The largest contribution to the increase in yield is attributed to the correction of the associated particle selection efficiency. Large fluctuations of the correlation distributions were observed in all of the studied p_{T} regions of D^0, though a distinct near side peak was observed in the $8 < p_{\mathrm{T}}^{\mathrm{D}^0} < 16\ \mathrm{GeV}/c$ region, where indications of an away side peak could also be found. For the full $3 < p_{\mathrm{T}}^{\mathrm{D}^0} < 16\ \mathrm{GeV}/c$ range, indications of a wide near side peak was observed.

The relatively wide transverse momentum bins, i.e., $3 < p_{\mathrm{T}}^{\mathrm{D}^0} < 5\ \mathrm{GeV}/c$, $5 < p_{\mathrm{T}}^{\mathrm{D}^0} < 8\ \mathrm{GeV}/c$ and $8 < p_{\mathrm{T}}^{\mathrm{D}^0} < 16\ \mathrm{GeV}/c$, were chosen to increase the number of correlated pairs available in each bin, and thus reduce statistical fluctuations in the correlation distributions. At low $p_{\mathrm{T}}^{\mathrm{D}^0}$, the near- and away side peaks of the distribution have small amplitudes that can not be disentangled from the statistical fluctuations of the baseline, which is related to the multiplicity of the event and thus is higher in p–Pb collisions than in pp collisions [113].

5.1.5 Extraction of Associated Particle Yields

After the fully corrected correlation distributions had been produced, the associated yield per trigger particle was extracted by fitting the correlation distribution in $\Delta\varphi$. The reflected distributions were fitted by a function composed of two Gaussian terms, describing the near side and away side peaks, in addition to a constant term, b, de-

scribing the baseline [113]:

$$f(\Delta\varphi) = b + \frac{A_{NS}}{\sqrt{2\pi}\sigma_{fit,NS}} e^{-\frac{(\Delta\varphi)^2}{2\sigma^2_{fit,NS}}} + \frac{A_{AS}}{\sqrt{2\pi}\sigma_{fit,AS}} e^{-\frac{(\Delta\varphi-\pi)^2}{2\sigma^2_{fit,AS}}} . \quad (5.2)$$

The integrals of the Gaussian terms, A_{NS} and A_{AS}, describe the associated particle yields for the near side and away side peaks, while $\sigma_{fit,NS}$ and $\sigma_{fit,AS}$ quantify the width of the correlation peaks. The mean of the peaks were fixed to $\Delta\varphi$ = 0 and $\Delta\pi$, due to symmetry considerations and the baseline represents the physical minimum of the distribution. The baseline was determined by calculating the weighted average of the two bins of the distribution with the lowest amplitude. The fitted $\Delta\varphi$ distributions and the extracted yields and sigmas for various scenarios will be presented in Chapter 6.

5.2 Study of Correlations in Monte Carlo Simulations

The correlation analysis was performed on a Monte Carlo (MC) sample[4], in order to gain a better understanding of the performance of the analysis strategy. The sample used for studies of simulated events is enriched by one $\mathrm{c\bar{c}}$ or $\mathrm{b\bar{b}}$ pair forced to decay semileptonically in each event, in order to provide enough statistics for studies on separate particle origins. This section will discuss the correlation distributions of particles on the generated level (*kinematical*), and the distributions of particles which have been propagated through a detailed simulation of the detector and been successfully reconstructed using the same methods as for data (*reconstructed*). Comparisons between results from data and simulations can be found in Chapter 6.

Studies of correlation distributions in simulated events allows an understanding of how the analysis strategy performs in terms of reproducing the generated particles at the reconstructed level. For the analysis at the kinematical level, only acceptance cuts were applied to the trigger and associated particles, and Monte Carlo information was used for directly identifying the particles. Correlations of D^0 mesons with electrons decaying from that same D^0 meson cause an unnaturally high and narrow near-side peak, and to avoid this auto-correlation, these electrons were removed from the kinematical sample [18]. In the analysis at the reconstructed level, the selection of particles was performed with the exact same method as was used in the analysis

[4] See Appendix A.2 for details of the sample.

run over data. At both the reconstructed and kinematical level, only tracks which were true MC D^0 or electrons were stored, and additionally only primary electrons, i.e., electrons produced directly from the collision or decaying from heavy-flavour mesons, were considered. While the analysis at the reconstructed level follows the full correlation distribution extraction presented in this chapter, the particles in the kinematical analysis are known to be a pure sample, and do not suffer from selection inefficiencies, and thus the sideband subtraction and efficiency correction is not applied. Acceptance correction by the mixed event method is still applied, to account for the effects of the acceptance cuts.

The correlation distributions at the kinematical and reconstructed levels were produced for four different combinations of D^0 meson and electron origins, as seen in Figure 5.5. The full sample of D^0 mesons and electrons (allD^0-allEl) was computed, in addition to separated samples where both the D^0 meson and electron were required to originate from charm quarks (cD^0-cEl) or beauty quarks (bD^0-bEl), in addition to a sample where D^0 mesons from all origins were correlated with non-HFE electrons (allD^0-nonHFEl). The analyses on the reconstructed level was performed for each combination of the applied selection efficiency corrections, i.e., no efficiency corrections, only electron or D-meson corrections separately, or both applied combined. In the case of the D^0 meson efficiency correction, the origin of the meson was identified, and the prompt D^0 efficiency was applied to D^0 mesons originating from charm, while the feed-down efficiency was applied to D^0 mesons originating from beauty[5]. The resulting distributions are seen in Figure 5.5. The distributions in the given p_{T} range are dominated by correlated pairs originating from beauty, which is particularly prominent on the near side. In the kinematical distribution an elevation of the away side can also be seen, attributed to pairs originating from charm, though this was found to be far less the case at the reconstructed level, even with the full efficiency corrections implemented. The correlation distributions at the reconstructed level appear to keep the same shape for all combinations of the efficiency maps, despite discrepancies in amplitude, indicating that the shapes of the distributions are not affected by the efficiency corrections.

A further comparison of the reconstructed and kinematical distributions was performed by computing the ratio of the distributions with the different variations of efficiency corrections for the reconstructed case, as seen in Figure 5.6. The ratio of the distributions for all of the samples were observed to lie below unity in the scenario without efficiency corrections. For all cases except the analysis of particles originating

[5] The prompt and feed-down D^0 meson efficiencies are presented in Figure 4.3, at page 70.

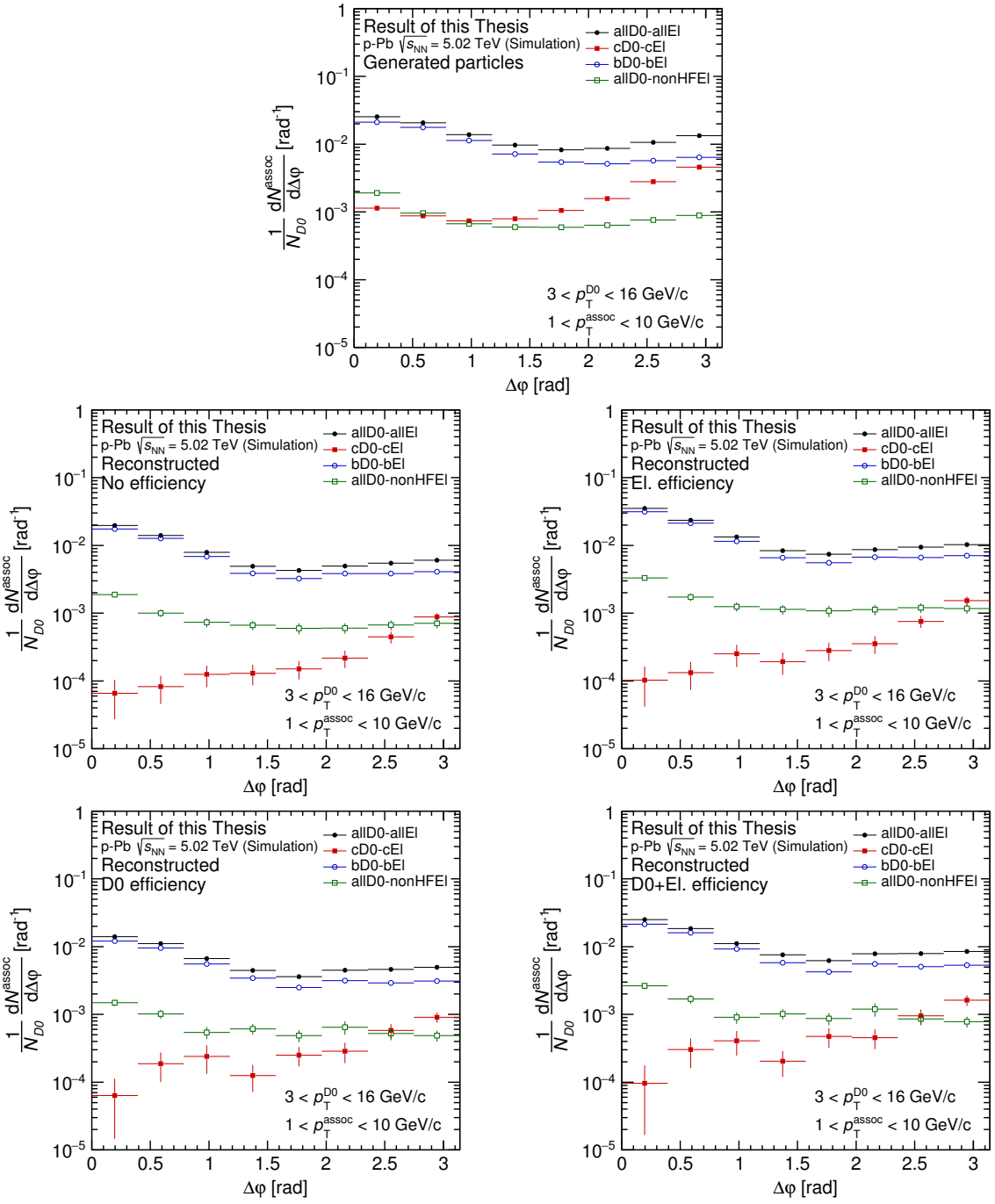

Figure 5.5: Azimuthal angular D^0-e correlations at the kinematical level, and at the reconstructed level with four variations of efficiency corrections. The analysis is shown for four combinations of D^0 and electron candidate sources, namely, (black circles) all sources of D^0 mesons and electrons, D^0 mesons and electrons originating from (red squares) charm quarks or (blue, open circles) beauty quarks, and (green, open squares) D^0 mesons from any origin, correlated with electrons which are not heavy-flavour electrons.

from charm, applying only the D-meson or electron efficiency correction was found to result in a under and over estimation, respectively. The combined efficiency correction result in a nearly flat ratio close to unity for the distributions of beauty and all origins, while the case of all D^0 mesons correlated to non-HFE was found to be subject to more fluctuations, due to limited statistics for the sample. The distribution of particles originating from charm is nearly flat, but the distribution at the reconstructed level was found to lie consistently lower than that of the generated particles.

The ratios of the distributions at various levels of efficiency corrections was performed for the distributions with different particle sources, as seen in Figure 5.7. The ratios of the distributions were calculated at given levels of efficiency correction, over the uncorrected distributions. For the studies with particles of all four combination of sources, the ratios of the distributions were observed to be nearly flat, within uncertainties, indicating that the efficiency corrections only scale the distributions, and do not introduce any unwanted structures to the correlation distributions.

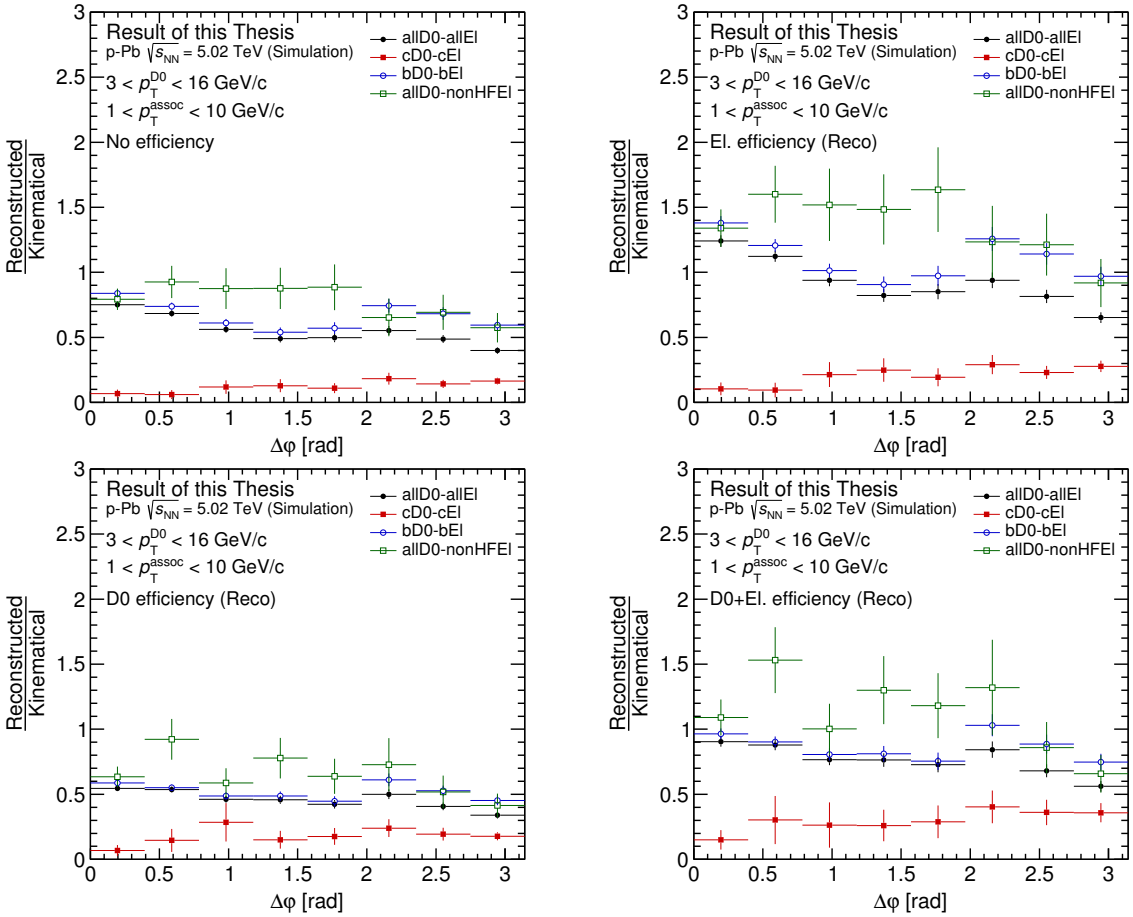

Figure 5.6: Ratio of Azimuthal angular D^0-e correlations at the reconstructed level and at the kinematical level, with four variations of efficiency corrections for the distributions at the reconstructed level. The scenario with no efficiency corrections is seen in the upper left panel, the distribution corrected for only electrons is presented in the upper right panel, and only for D^0 in the lower left corner. The lower right distribution shows the ratio corrected for both D^0 and electron efficiencies. The colours and symbols of the D^0 meson and electron origins is the same as presented in Figure 5.5. In an ideal case, the ratio after corrections should be unity, indicating that no difference between the generated and measured distributions are present.

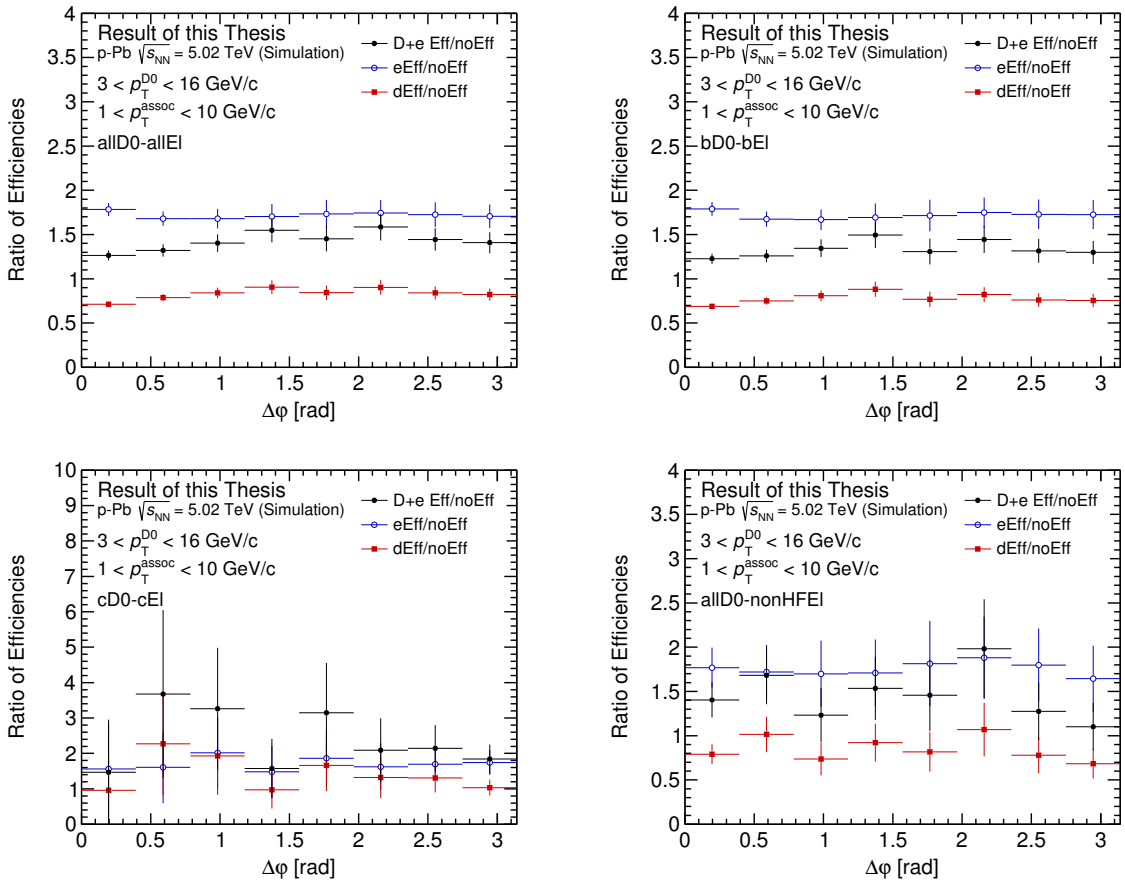

Figure 5.7: Ratio of Azimuthal angular D^0-e correlations at different levels of efficiency corrections, for various particle sources. The ratio has been calculated between (black circles) the fully efficiency corrected sample, (blue, open circles) the electron efficiency corrected sample, and (red squares) the D^0 efficiency corrected sample, versus the non-corrected sample. The distributions are observed to be nearly flat within uncertainties, indicating that the efficiency corrections scales the distributions, but does not introduce structures. Note: very large uncertainties were observed in the (lower left) case where particles originating from charm quarks are studied, leading to the larger range of the y-axis in this panel compared to the other scenarios.

Chapter 6

Results from D^0-e Correlations

The final results extracted from the measurement of azimuthal angular correlations of D^0 mesons and electrons will be presented in this chapter. The results from data collected from p–Pb collisions at $\sqrt{s_{\mathrm{NN}}} = 5.02\,\mathrm{TeV}$ are compared to Monte Carlo simulations in two intervals of $p_{\mathrm{T}}^{\mathrm{D}^0}$ in Section 6.1. In the same section, an additional comparison is made between results obtained using the two of the electron selection strategies discussed in Section 4.3.5, namely Strategy-712 and Strategy-000. A comparison of D^0-e correlation distributions in the p–Pb collision system at $\sqrt{s_{\mathrm{NN}}} = 5.02\,\mathrm{TeV}$ and in pp collisions at $\sqrt{s} = 7\,\mathrm{TeV}$ [18] is presented in Section 6.2.

The final, corrected, azimuthal angular correlation distributions were reflected[1] and fitted by a two-Gaussian function (see Section 5.1.5) in order to extract the associated particle yield and sigma per trigger particle in the near and away side peaks. The yield quantifies the number of associated particles in the given peak, while the sigma describes the width of the fit. As was discussed in Section 2.3, the shapes of the peaks, both in width and amplitude, is related to production processes and fragmentation functions of the heavy-flavour quark pairs produced in the initial hard scattering processes of the collisions, and for the p–Pb case the interaction with the medium. These measurements can thus provide restraints to models describing such systems.

[1] See Section 5.1.3 for information about the reflection procedure.

6.1 Results from p–Pb Collisions at $\sqrt{s_{NN}} = 5.02\,\mathrm{TeV}$

The resulting distributions from D^0-e correlations in the p–Pb collision system is presented in the two upper rows of Figure 6.1 for the full p_{T} range of trigger and associated particles studied in this analysis, i.e, $3 < p_{\mathrm{T}}^{\mathrm{D}^0} < 16\ \mathrm{GeV}/c$ and $1 < p_{\mathrm{T}}^{\mathrm{e}} < 10\ \mathrm{GeV}/c$. The top row shows the correlation distributions where electrons have been selected by Strategy-712, while those in the middle row have been produced using Strategy-000. In these two rows, the left panels display the distribution produced from the data sample, while the plots to the right shows the case in Monte Carlo simulations. Large fluctuations and statistical uncertainties were observed in data for both scenarios, leading to large errors in the fitting procedure, as seen from the extracted yield and sigma of the near- and away side peaks in the two bottom panels of Figure 6.1. Particularly the near side sigma was found to have a large uncertainty. The fluctuations also introduces uncertainties in the baseline determination of the distributions, further adding to the uncertainty of the amplitudes of the peaks. The baseline was estimated using the weighted average of the two bins with lowest amplitude in all the results presented in this chapter. The results from data and simulation were observed to be compatible within uncertainties for both strategies, except from a deviation of the near side sigma. The two compared strategies were found to be in agreement with each other.

From the comparison of the segmented $p_{\mathrm{T}}^{\mathrm{D}^0}$ ranges, seen in Figure 5.4 (page 96), the interval $8 < p_{\mathrm{T}}^{\mathrm{D}^0} < 16\ \mathrm{GeV}/c$ was observed to have a distinct near side peak as well as indications of an away side peak, while obvious structures could not be identified in the other $p_{\mathrm{T}}^{\mathrm{D}^0}$ regions. The distributions of D^0 mesons in the range $8 < p_{\mathrm{T}}^{\mathrm{D}^0} < 16\ \mathrm{GeV}/c$ correlated with electrons with p_{T} between 1-10 GeV/c were fitted and compared to simulations, as presented in Figure 6.2. Comparing the distributions and fits in data and simulations revealed a disagreement in the width of the near and away side peaks, both in the case of Strategy-712 and Strategy-000. A more narrow peak of higher amplitude was observed for the correlation distributions in data. Despite the differences in width and amplitude, the extracted yields in the near- and away side for both data and simulations are compatible within uncertainty for each electron selection strategy. Both strategies were found to have compatible yields within uncertainties, but a disagreement in the near side yields in the distributions from Monte Carlo was observed, with the near side peak of Strategy-000 having a higher amplitude. The p–Pb simulation used in these comparisons were, as previously mentioned, enhanced by $\mathrm{b\bar{b}}$ and $\mathrm{c\bar{c}}$ pairs, which is likely to bias the distribution. Ideally,

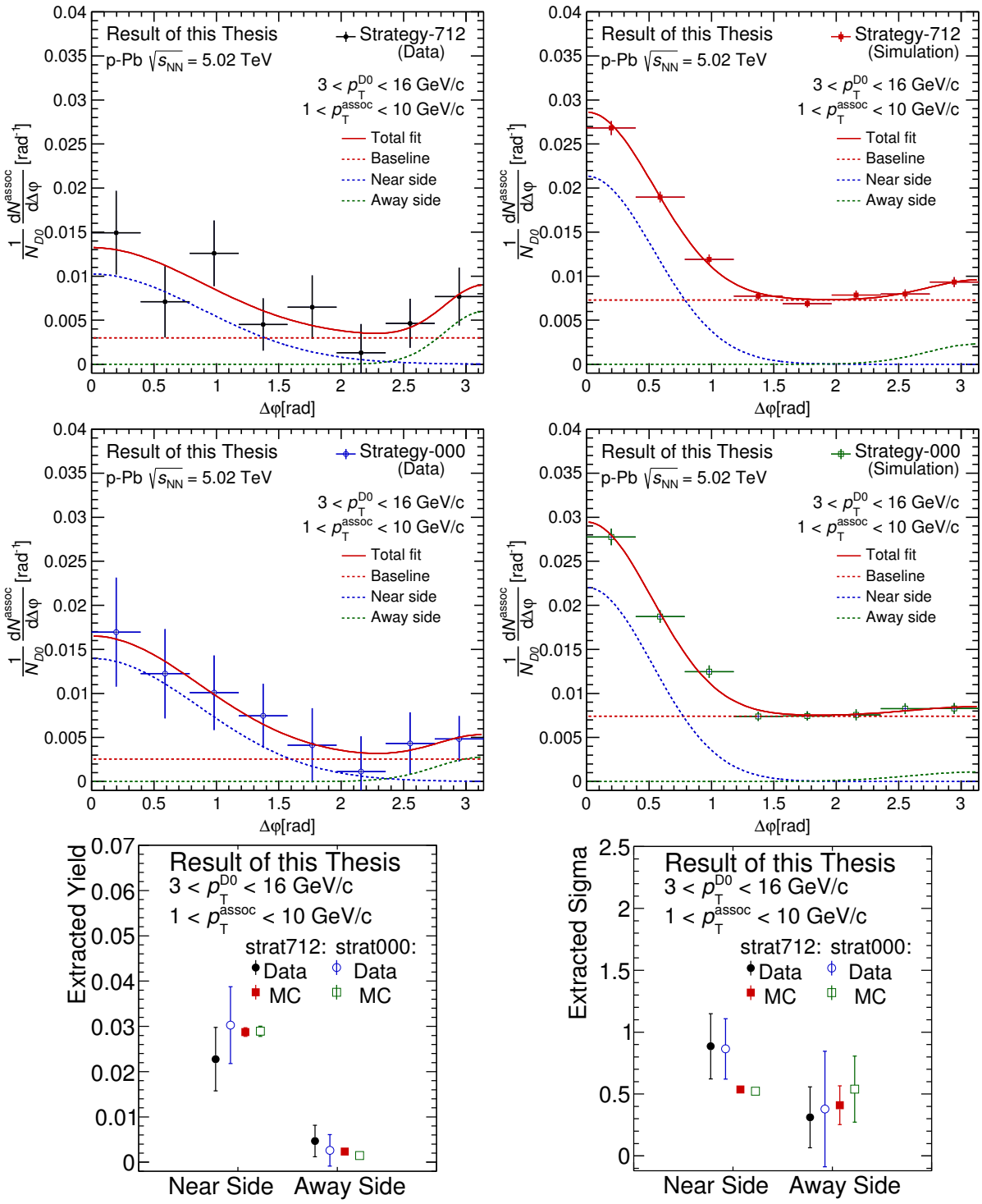

Figure 6.1: Comparison of the correlation distributions for the electron selection Strategy-712 (upper row) and Strategy-000 (middle row), and the extracted yield and sigma (bottom row) in data and Monte Carlo simulations. The correlations are performed for the p_T ranges $3 < p_T^{D^0} < 16$ GeV/c, $1 < p_T^{e} < 10$ GeV/c.

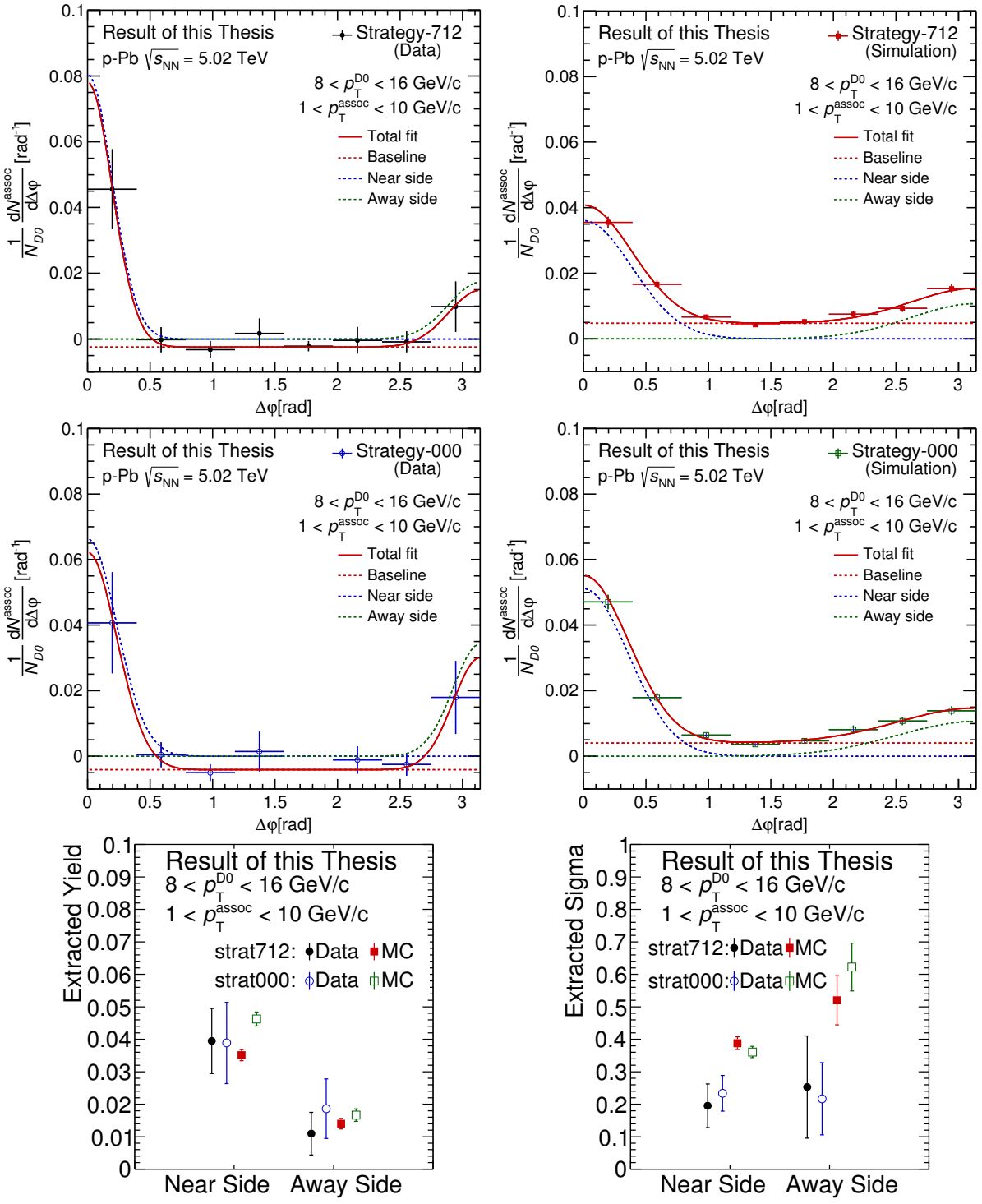

Figure 6.2: Comparison of the correlation distributions for the electron selection Strategy-712 (upper row) and Strategy-000 (middle row), and the extracted yield and sigma (bottom row) in data and Monte Carlo simulations. The correlations are performed for the p_T ranges $8 < p_T^{D^0} < 16$ GeV/c, $1 < p_T^{e} < 10$ GeV/c.

a minimum bias sample should be used for the comparison, but no such sample with sufficient statistics for the correlation analysis of D^0-e was available at the time of the thesis.

In the correlation distribution produced with the selection Strategy-000, the 5^{th} bin is missing, resulting from the limited statistics available. In fact, 4 of the 16 bins (bin 3, 9, 15 and 16) of the non-reflected $\Delta\varphi$ distribution using Strategy-000 for the electron selection, and one bin (bin 16) in the case of Strategy-712, were not filled for the 8 $< p_{\mathrm{T}}^{\mathrm{D}^0} <$ 16 GeV/c, 1 $< p_{\mathrm{T}}^{\mathrm{e}} <$ 10 GeV/c scenario. The missing 5^{th} bin in the reflected distribution of Strategy-000 results from the combination of the 9^{th} and 16^{th} bin during the reflection procedure. The lower electron selection efficiency of Strategy-000 thus result in a less precise determination of the baseline, in addition to the marginally larger error bars observed for this sample. Despite these issues, both strategies were found to agree well in both of the considered scenarios, which indicates that the results are not significantly altered by the electron selection strategy.

6.2 Comparison with pp Collisions at $\sqrt{s} = 7$ TeV

To conclude the results, a comparison between correlation distributions from simulations and data in pp at $\sqrt{s} = 7\,\mathrm{TeV}$ [18] and p–Pb collisions at $\sqrt{s_{\mathrm{NN}}} = 5.02\,\mathrm{TeV}$ was performed, as seen in Figure 6.3. The $p_{\mathrm{T}}^{\mathrm{D}^0}$-range studied in the pp analysis extended down to 2 GeV/c, with an interval of 1 $< p_{\mathrm{T}}^{\mathrm{e}} <$ 4 GeV/c for associated particles, and thus the range of the p–Pb analysis was extended to the same value for this comparison. In order to perform a comparison with equal conditions of the fit, the data points from the pp-analysis [18] were reflected and re-fitted. The electron selection Strategy-000 was used in both correlation analyses. From the fits in the p–Pb collision system, the yields were observed to decrease compared to the values extracted from the distributions in the ranges 3 $< p_{\mathrm{T}}^{\mathrm{D}^0} <$ 16 GeV/c with 1 $< p_{\mathrm{T}}^{\mathrm{e}} <$ 10 GeV/c.

A comparison of the extracted yields and sigmas from the distributions in data and simulations in pp and p–Pb is seen in the bottom panels of Figure 6.3. The values of the near- and away side sigma obtained from p–Pb data, and for simulations on the away side, were found to be very large, and thus provide little information. Particularly for the p–Pb distributions this is expected from the marginal amplitude of the away side. The near- and away side yields from simulated events in p–Pb were found to not be in agreement with either data or simulations in the pp collision system, and the near side sigma was also found to deviate from pp simulations. A compatibility within uncertainties of the yield and sigma from p–Pb data and simulations was

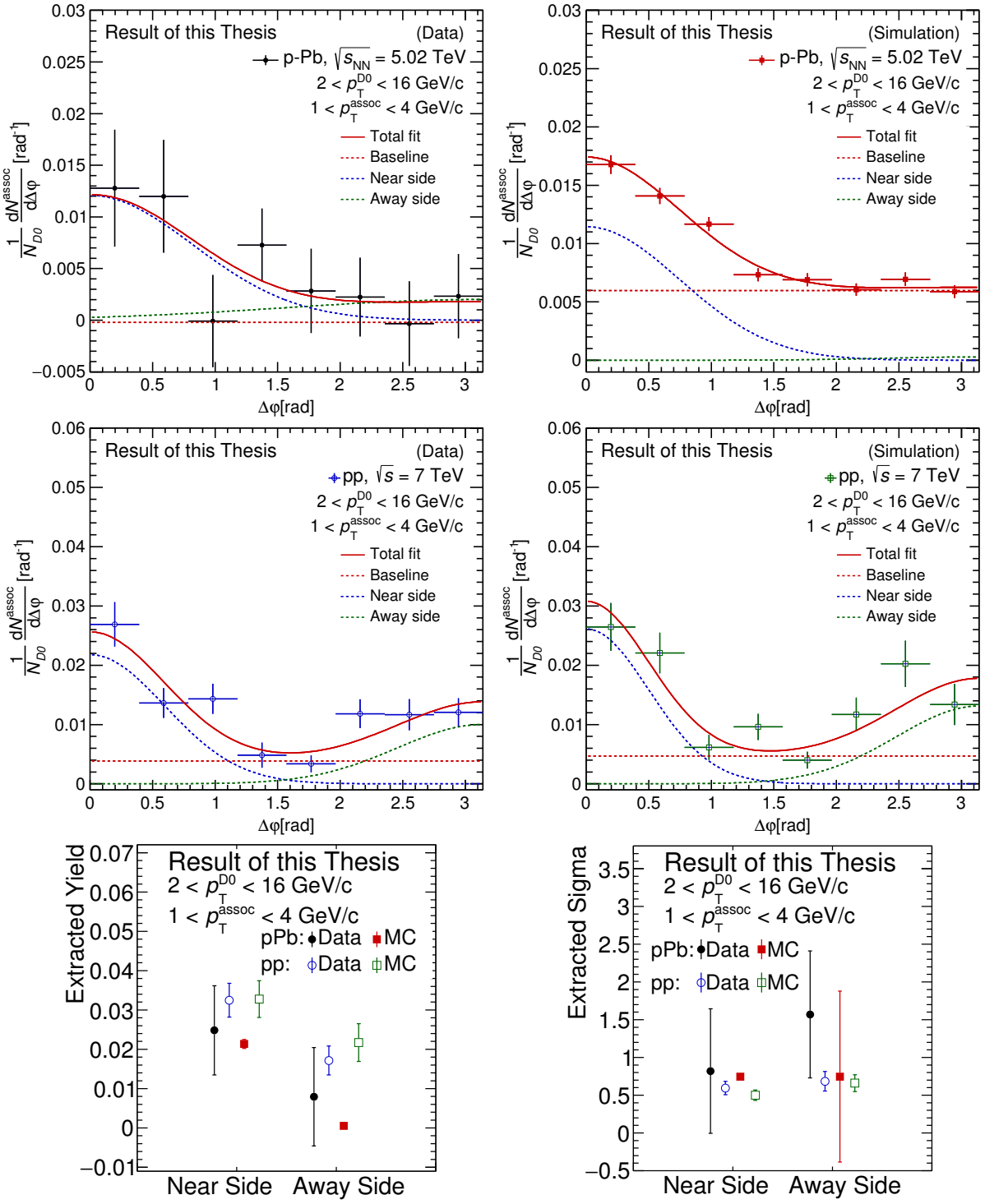

Figure 6.3: Comparison of the correlation distributions from p–Pb (upper row) and pp collisions (pp distributions originating from [18] were refitted) (middle row), and the extracted yield and sigma (bottom row) in data and Monte Carlo simulations. The correlations are performed for the p_T ranges $2 < p_T^{D^0} < 16$ GeV/c, $1 < p_T^{e} < 4$ GeV/c.

found, as well as an agreement with the results from simulations and data in the pp collision system. The results from p–Pb were observed to agree with both data and simulations in pp, and the deviation of the p–Pb simulations is likely to be a result of the aforementioned enhancement of this Monte Carlo sample. The most remarkable difference between the results from p–Pb and pp is the shape of the away side peak, which, although compatible within uncertainties, appears to have a lower amplitude. This change in shape between the two collision systems provides great potential for the understanding of interactions with the medium.

Chapter 7

Conclusion and Outlook

7.1 Conclusion

The measurement of azimuthal angular correlation distributions between D^0 mesons and electrons in proton-lead collisions at $\sqrt{s_{\mathrm{NN}}} = 5.02\,\mathrm{TeV}$ in ALICE has been presented in this thesis, and compared to results from pp collisions at $\sqrt{s} = 7\,\mathrm{TeV}$, and Monte Carlo simulations. A large part of the work leading to these results has revolved around the development of the analysis software, as an ongoing process throughout the duration of the project, aiming for a flexible and stable framework. A challenge for the analysis has been the limited statistics available from data, and substantial efforts were dedicated to optimize the electron selection efficiency while maintaining a high purity of heavy-flavour electrons, in order to exploit the statistics to its full extent.

The results of the analysis were presented in Chapter 6. Despite the limited statistics and relatively large fluctuations observed from the correlation distributions, a compatibility of the compared scenarios was observed, within uncertainties. The extracted yields and sigma for the analysis were found to be in agreement for both the comparison of distributions obtained with two different electron selection strategies, in the two D^0 meson p_{T} regions $3 < p_{\mathrm{T}}^{\mathrm{D}^0} < 16\ \mathrm{GeV}/c$ and $8 < p_{\mathrm{T}}^{\mathrm{D}^0} < 16\ \mathrm{GeV}/c$, and for the comparison of correlation of particles from the pp and p–Pb collision systems in the $2 < p_{\mathrm{T}}^{\mathrm{D}^0} < 16\ \mathrm{GeV}/c$ interval. While discrepancies were found in some scenarios between the widths of the distributions in Monte Carlo simulations and data, the associated yields of the near side and away side peaks were found to be in agreement for the different cases.

The introduction of new electron selection strategies increased the efficiency of the electron selection, while maintaining a high electron- and HFE purity. This resulted in an increase of the number of selected electrons for the correlation analysis by ∼40% in the region $0.5 < p_{\mathrm{T}}^{\mathrm{e}} < 5\ \mathrm{GeV}/c$, where the purity of the two strategies are comparable. A significant increase in HFE purity in the $5 < p_{\mathrm{T}}^{\mathrm{e}} < 10\ \mathrm{GeV}/c$ interval was achieved, increasing the p_{T} region in which electrons could be studied. The effect on the fluctuations and uncertainties of the final distributions was not observed to be very large, but particularly for the higher end of the D^0 meson p_{T} range studied, the increased efficiency reduced the occurrence of empty $\Delta\varphi$ bins. This, in turn, allowed for an increased precision of the baseline determination, which is an important factor in the fitting procedure and the extraction of the associated yield and sigma of the distribution peaks.

The results obtained from the analysis proves that there is a strong potential for further work on this analysis in ALICE, and places an important foundation, along with the previous analysis in pp collisions [18], for studies of correlations between D^0 mesons and electrons in the Pb–Pb collision system. An increase in statistics is expected from the recent p–Pb collisions at $\sqrt{s_{\mathrm{NN}}} = 5.02\,\mathrm{TeV}$, as discussed in Section 7.3, which will play an important role in reducing the statistical uncertainties of the analysis.

7.2 Potential for Improvements of the Analysis

Despite the efforts put into the development and tuning of the analysis, there is still room for improvement. A few suggestions for future work will be discussed in this section.

7.2.1 Offline Mixed Event Corrections

The correction for detector acceptance and inhomogeneities, performed by the event mixing method, depends on the number of events available to build the event mixing pools, described in Section 5.1.2. The correction is currently done by storing the information of correlated pairs in the Same Event and Mixed Event analyses as they are run, assigning the pairs to pool bins based on their multiplicity and Z-vertex position. The number of particle pairs used to build the mixed event distribution is limited by the number of events available to the analysis job, which in turn is limited by the amount of data sent to each subjob of the analysis. In an ideal case, the mixed

event correction should be performed with all available events of the data sample. An adaption of an *offline*[1] method for the mixed event corrections has been under development recently for the analysis of D-hadron correlations in ALICE, by the PWG-HF Physics Analysis Group HFCJ. In this approach, particle information is stored for all track combinations, and the correction is performed during post-processing, providing an improved correction due to the higher statistics. This approach requires reworking of the storage structure of the analysis task, and was unfortunately not feasible within the timeframe of this thesis. Further quality assessment of the analysis would also be required after such a change. The offline mixed event corrections should be a priority in the further work of the analysis.

7.2.2 Particle Identification of Electrons

Two approaches for particle identification (PID) of electrons were presented in this thesis, and despite the different implementations, both of these rely mainly on information from the TPC and TOF. As mentioned in Section 3.3, other detectors also have PID capabilities, and could be introduced to the analysis. The TRD, EMCal, PHOS and DCal[2] detectors have electron PID capabilities, and are of interest for the D^0-e correlation analysis. The TRD and EMCal detectors have already been used for particle identification in other analyses studying electrons from heavy-flavour hadron decays [73, 140], and could improve the purity for $p_{\mathrm{T}}^{\mathrm{e}} > 5\ \mathrm{GeV}/c$, without the strict pion rejection cut of $\pm 3\ n_{\sigma}^{\mathrm{TPC}}$ used to separate the pion and electron samples in this thesis. The EMCal has limited acceptance in azimuth, covering $80^{\mathrm{o}} < \varphi < 187^{\mathrm{o}}$[3], in addition to a lower η coverage compared to the TPC and TOF. Thus, the efficiency of the electron selection using EMCal would be limited. The TRD also had a limited azimuthal coverage during the 2013 p–Pb data taking, while during LHC Run 2 a full coverage was achieved as all modules were installed [4], with a pseudorapidity coverage of $|\eta| < 0.8$. Due to the already scarce statistics and relatively high purity, the inclusion of these detectors is more relevant when more statistics is available, and the selection purity does not have to be compromised as much in favor of the selection efficiency.

[1] The terminology online and offline refers to if the analysis requires large computing resources and is run on a computing cluster, e.g., the WLCG (online), or if it can be run locally (offline).

[2] DCal was installed after LHC Run 1, and was not available during the p–Pb data taking in 2013.

[3] The addition of the DCal will extend the acceptance in azimuth by 67^{o}.

[4] At the time of the 2013 p–Pb collisions, 13 of the 18 modules were installed, as seen in Figure 3.5, page 57, while all 18 modules were installed during Run 2.

More complicated PID schemes could be employed for further increasing the efficiency. The proton rejection implemented for the region where TOF matching is not enforced, as described in Section 4.3.5, could be limited to only cases where the TOF matching is not found, instead of cutting purely based on the tracks momentum. Further studies would be required to ensure that no bias is imposed by this approach, and only minor increases in efficiency would be expected.

7.2.3 Simultaneous Tuning of Electron and D^0 Selection

The selection of D^0 mesons and electrons have, to a large extent, been optimized separately for the results presented in this thesis. While the selection strategies of electrons have received most attention, attempts were also made to tune the D^0 selection, but in general the statistical significance of the signal was found to drop rapidly with looser selection cuts. Due to the correlation of D^0 mesons and heavy-flavour electrons, the requirement of finding a heavy-flavour electron candidate in each correlated event acts as a cut on the D^0 meson candidates as well, and thus a simultaneous tuning of the D^0 and electron selection could yield a higher significance for D^0, despite using a looser selection. In order to perform this study the efficiency and purity of the correlated electrons and D^0 mesons would need to be studied and understood properly, in addition to studying the separate particle selection cases.

7.3 Increased Statistics - LHC Run 2

The analysis presented in this thesis is optimized for high selection efficiencies and purities of the particle samples, and thus more data must be collected to reduce the statistical uncertainties significantly. Additional collisions at $\sqrt{s_{\mathrm{NN}}} = 5.02\,\mathrm{TeV}$ in ALICE, were performed in the end of 2016, expected to yield approximately 6 times the statistics available from 2013. These additional data will be compatible with the already available data, and could prove to reduce statistical fluctuations and errors, allowing more precise measurements of the azimuthal angular correlations of D^0 mesons and electrons.

During the Long Shutdown (LS1) between Run 1 and Run 2, the detector performance was increased by installing the final 5 TRD modules and one additional PHOS module. A new detector using modules of the EMCal design, named the Di-jet Calorimeter (DCal), was also installed around PHOS, allowing for back-to-back correlation

studies when used along with EMCal, extending the coverage in azimuth by 67°, resulting in a total of 174°.

7.4 Detector Upgrades - LHC Run 3

After Run 2 ends in the end of 2018, LHC will shut down for two years, after which collisions will resume in Run 3 [147]. During this long shutdown the ALICE experiment will undergo upgrades, improving the detector performance and allowing higher collision rates. ALICE aims to run at a 50 kHz collision rate in Pb–Pb collisions, with improved low-momentum vertexing and tracking capabilities [148]. The planned upgrades are as follows [148]:

- **Reduced beam pipe:** The beampipe inner radius will be reduced from 29 mm to 18.6 mm, allowing for an additional layer of ITS closer to the interaction point [149].
- **New ITS:** A new, high-resolution, low-material-thickness Inner Tracking System (ITS) will be installed, increasing the resolution of the distance of closest approach (DCA) between a track and the primary vertex by a factor 3, and increasing the standalone ITS tracking performance significantly. The current ITS has six layers covering a radius from 39 mm to 430 mm, while the new system will have seven layers with the inner radius reduced to 23 mm [150], made possible by the reduction of the radius of the beam pipe. The detector technology of all layers is planned to be replaced by Monolithic Active Pixel Sensors (MAPS) with higher resolution than the current ones, while at the same time reducing the material budget per layer to 0.3% X_0 [150].
- **Upgraded TPC:** The Multi Wire Proportional Chamber (MWPC) read-out system of the TPC will be replaced by Gas Electron Multiplier (GEM) detectors, with new continous read-out electronics required for the planned increase of the interaction rate.
- **Improved read-out electronics:** The read-out electronics of the TPC, TOF, TRD, PHOS and Muon spectrometer will be improved, in order to cope with the planned high rate of data taking.
- **Upgrade of forward trigger detectors:** The forward trigger detectors will be upgraded as required by the increased interaction rate.

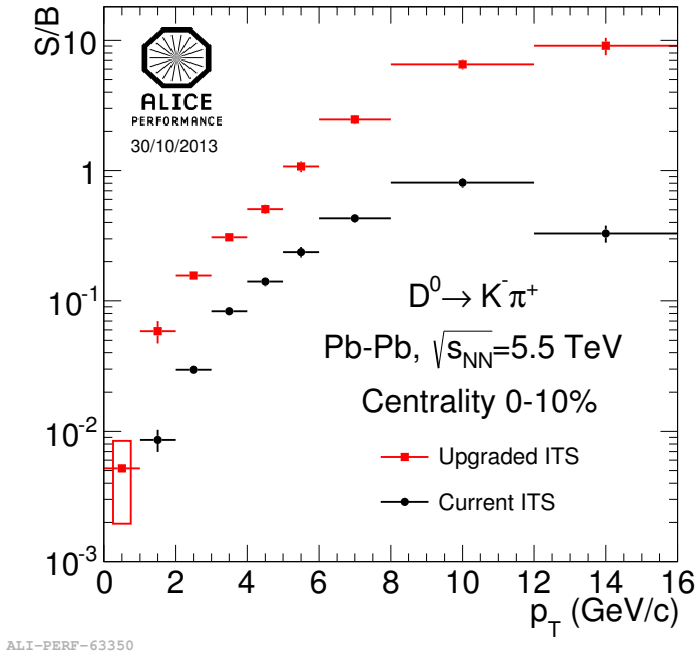

Figure 7.1: Comparison of the signal over background, S/B, for $\mathrm{D}^0 \to \mathrm{K}^-\pi^+$ in Pb–Pb collisions at 0-10% centrality at $\sqrt{s_{\mathrm{NN}}} = 5.5\,\mathrm{TeV}$, with the current (Run 1) and upgraded (Run 3) ITS. The efficiency of the signal selection with the current and upgraded ITS was found to be comparable, while the background rejection using the upgraded detector is exptected to improve by a factor 4-5 for $p_{\mathrm{T}} > 2\ \mathrm{GeV}/c$, and a factor close to 10 for $p_{\mathrm{T}} < 2\ \mathrm{GeV}/c$, thus increasing the S/B ratio [151].

A statistics estimate was performed for the measurement of correlations between D^0 mesons and electrons from heavy-flavour hadron decays in Pb–Pb collisions, with a realistic description of the upgraded ITS detector as planned for Run 3. The study, which is summarized here, and discussed in more detail in [18][5], considered a simulated sample of 8×10^9 events at 0-10% centrality at $\sqrt{s_{\mathrm{NN}}} = 5.5\,\mathrm{TeV}$, with an average charged-particle pseudorapidity density, $\mathrm{d}N_{ch}/\mathrm{d}\eta$=2000, generated by HIJING [153]. The heavy-flavour signal was added to the HIJING sample using a cocktail of parametric generators and heavy-quark pairs generated with PYTHIA [154] [18]. The ex-

[5] Some discrepancies between the values and results of the statistics estimate presented in this thesis and [18] are present, due to additional tuning and further checks during the continuation of the studies, leading to the finalization of the results [152].

pected D^0 meson signal and background were extracted from the simulation, in addition to estimates of the efficiencies of various electron sources. A large increase in the background rejection was observed, of about factor 4-5 for $p_{\mathrm{T}} > 2$ GeV/c, and a factor close to 10 for $p_{\mathrm{T}} < 2$ GeV/c [151]. The efficiency of the signal selection was found to be comparable for the current (Run 1) and upgraded (Run 3) ITS, leading to a significant increase of the signal over background, S/B, as seen in Figure 7.1, due to the improved background rejection [151]. Furthermore, the efficiency of various electron sources was calculated from the simulated sample, and the tracking efficiency was found to increase significantly compared to the situation observed in 2010 pp data [18]. Finally, the baseline was calculated by a correlation analysis over the HIJING sample, estimating the underlying event.

A second Monte Carlo simulation generated using PYTHIA, with the requirement of having at least one D^0 meson in each event, was used to create $\Delta\varphi$ distributions for D^0 mesons with different electron sources [18]. As a first approximation, a perfect heavy-flavour electron (HFE) sample was assumed. From this simulated sample, a template $\Delta\varphi$ distribution was produced, as seen in Figure 7.2, for the two trigger-p_{T} ranges of $5 < p_{\mathrm{T}}^{\mathrm{D}^0} < 8$ GeV/c and $8 < p_{\mathrm{T}}^{\mathrm{D}^0} < 16$ GeV/c. The $\Delta\varphi$ distributions were calculated separately for D^0-e pairs originating from prompt and feed-down D^0 mesons, and scaled by the fraction of prompt and feed-down calculated using FONLL predictions in order to create the combined template distribution, seen as the solid red line in the two upper panels of Figure 7.2. The $\Delta\varphi$ distribution was further scaled by the calculated HFE efficiency, in addition to the S/B of the D^0 meson candidates with the upgraded ITS, seen in Figure 7.1. The baseline of the distribution from PYTHIA was removed and replaced with the one estimated from the HIJING sample, which better describes the underlying sample. The near side peak was observed to be artificially low compared to measurements in data, due to the assumption of a completely pure HFE sample, and thus only the away side peak was used for the statistics estimate [18]. Finally, the distribution was smeared according to Poisson statistics on a bin-by-bin basis using 100 iterations, in order to induce realistic fluctuations. The resulting distributions for the two p_{T} regions studied are seen in the lower panels of Figure 7.2.

The relative uncertainty of the away side yield and sigma was extracted from the final $\Delta\varphi$ distributions (lower panels of Figure 7.2) by applying a double Gaussian fit function, similar to the procedure presented in Section 5.1.5, as seen in Figure 7.3. The results were calculated for the two previously mentioned regions of $p_{\mathrm{T}}^{\mathrm{D}^0}$, for three different ranges of $p_{\mathrm{T}}^{\mathrm{e}}$, all having an upper limit of 10 GeV/c, while the lower limits are

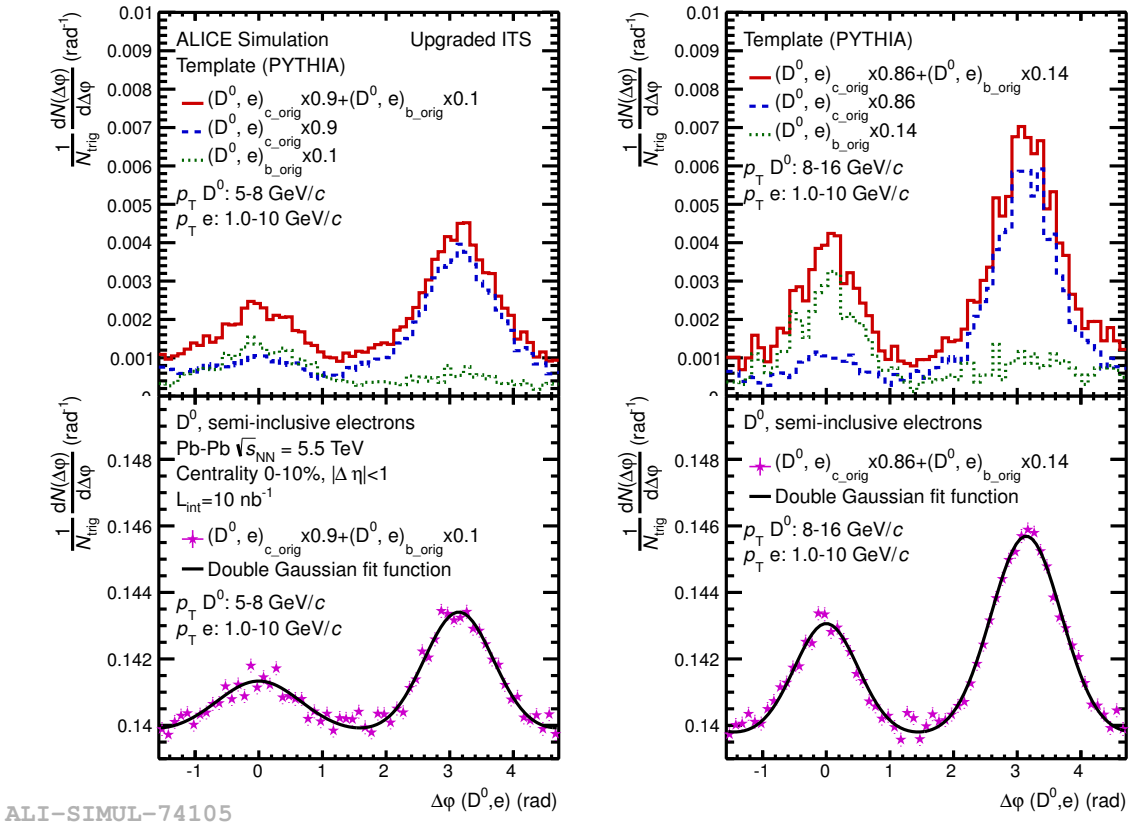

Figure 7.2: D0-e correlations based on simulations with the ITS detector upgrade planned for LHC Run 3. The template (upper row) and output (lower row) distributions, as expected for 8x10^9 Pb–Pb collisions at 0-10% centrality, at $\sqrt{s_{\mathrm{NN}}} = 5.5\,\mathrm{TeV}$, are presented in the two trigger particle p_{T} regions of $5 < p_{\mathrm{T}}^{\mathrm{D}^0} < 8\ \mathrm{GeV}/c$ and $8 < p_{\mathrm{T}}^{\mathrm{D}^0} < 16\ \mathrm{GeV}/c$, with the associated particles studied in the interval $1 < p_{\mathrm{T}}^{\mathrm{e}} < 10\ \mathrm{GeV}/c$. The blue dashed line represent the contribution from prompt D^0 mesons, while the dotted green line correspond to the feed-down contribution. The prompt and feed-down contributions were scaled by their relative fractions calculated from FONLL predictions, as indicated by the numbers in the legend. The solid red line represents the combined distribution from both sources. Figure from [152].

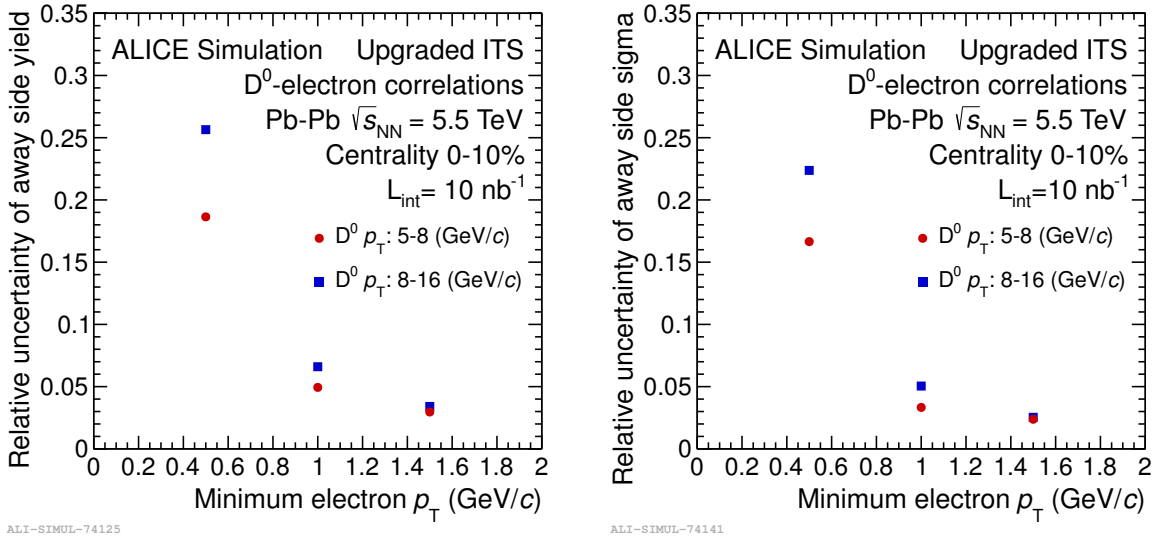

Figure 7.3: D0-e correlations with detector upgrade: Relative uncertainty of the away side yield (left) and away side sigma (right), as expected for 8x10^9 Pb–Pb collisions at 0-10% centrality, at $\sqrt{s_{\mathrm{NN}}} = 5.5\,\mathrm{TeV}$. A statistical uncertainty below $\sim$ 7% was observed for the away side yield and sigma for $p_{\mathrm{T}}^{\mathrm{e}}$ >1 GeV/c. Figure from [152].

noted on the x-axis of the plots, i.e., 0.5, 1.0 and 1.5 GeV/c. The statistical uncertainty was estimated to be lower than $\sim$ 7% for the away side yield and sigma for $p_{\mathrm{T}}^{\mathrm{e}} > 1$ GeV/c for D^0-e correlations in Pb–Pb collisions at $\sqrt{s_{\mathrm{NN}}} = 5.5\,\mathrm{TeV}$ with the planned upgrades of the ITS detector. The statistics estimate shows great potential for measurements of azimuthal angular correlations between D^0 mesons and electrons with improved detectors and increased statistics, as expected during Run 3 of the LHC.

Bibliography

[1] J. Dalton, *A New System of Chemical Philosophy*. William Dawson & Sons, 1808. http://openlibrary.org/books/OL7037962M/A_new_system_of_chemical_philosophy.

[2] *Standard Model*. http://www.physik.uzh.ch/groups/serra/StandardModel.html. Accessed: 07.06.2016.

[3] M. Gell-Mann, "A Schematic Model of Baryons and Mesons," *Phys. Lett.* **8** (1964) 214–215.

[4] G. Zweig, "An SU_3 model for strong interaction symmetry and its breaking; Version 1," Tech. Rep. CERN-TH-401, CERN, Geneva, Jan, 1964. https://cds.cern.ch/record/352337.

[5] J. D. Bjorken and S. L. Glashow, "Elementary Particles and SU(4)," *Phys. Lett.* **11** (1964) 255–257.

[6] M. Kobayashi and T. Maskawa, "CP Violation in the Renormalizable Theory of Weak Interaction," *Prog. Theor. Phys.* **49** (1973) 652–657.

[7] H. Harari, "An Analysis of a New Quark Model of Hadrons," *Annals Phys.* **94** (1975) 391.

[8] R. Rapp and H. van Hees, "Heavy Quark Diffusion as a Probe of the Quark-Gluon Plasma," arXiv:0803.0901 [hep-ph].

[9] D. J. Gross and F. Wilczek, "Ultraviolet Behavior of Nonabelian Gauge Theories," *Phys. Rev. Lett.* **30** (1973) 1343–1346.

[10] H. D. Politzer, "Reliable Perturbative Results for Strong Interactions?," *Phys. Rev. Lett.* **30** (1973) 1346–1349.

[11] K. A. Olive et al. (Particle Data Group), "Review of Particle Physics," *Chin. Phys.* **C38** (2014) 090001.

[12] E. Eichten, K. Gottfried, T. Kinoshita, J. Kogut, K. D. Lane, and T. M. Yan, "Spectrum of Charmed Quark-Antiquark Bound States," *Phys. Rev. Lett.* **34** (Feb, 1975) 369–372. http://link.aps.org/doi/10.1103/PhysRevLett.34.369.

[13] S. Schuchmann, *Modification of K^0_s and $\Lambda(\overline{\Lambda})$ transverse momentum spectra in Pb-Pb collisions at $\sqrt{^sNN}$ = 2.76 TeV with ALICE*. PhD thesis, Frankfurt U., 2015-04-14. http://inspirehep.net/record/1429481/files/fulltext_6cIw6W.pdf.

[14] K. G. Wilson, "Confinement of Quarks," *Phys. Rev.* **D10** (1974) 2445–2459.

[15] F. Karsch, E. Laermann, and A. Peikert, "The Pressure in two flavor, (2+1)-flavor and three flavor QCD," *Phys. Lett.* **B478** (2000) 447–455, arXiv:hep-lat/0002003 [hep-lat].

[16] P. Braun-Munzinger and J. Wambach, "The Phase Diagram of Strongly-Interacting Matter," *Rev. Mod. Phys.* **81** (2009) 1031–1050, arXiv:0801.4256 [hep-ph].

[17] B.-J. Schaefer and M. Wagner, "On the QCD phase structure from effective models," *Prog. Part. Nucl. Phys.* **62** (2009) 381, arXiv:0812.2855 [hep-ph].

[18] H. A. Erdal, *D^0-electron correlations in pp collisions at $\sqrt{s}$ =7 TeV*. PhD thesis, University of Bergen, 2014. https://cds.cern.ch/record/1704528.

[19] N. Cabibbo and G. Parisi, "Exponential Hadronic Spectrum and Quark Liberation," *Phys. Lett.* **B59** (1975) 67–69.

[20] J. C. Collins and M. J. Perry, "Superdense Matter: Neutrons Or Asymptotically Free Quarks?," *Phys. Rev. Lett.* **34** (1975) 1353–1356.

[21] A. Dainese, *Charm production and in-medium QCD energy loss in nucleus-nucleus collisions with ALICE. A performance study*. PhD thesis, Padova University, 2003. arXiv:nucl-ex/0311004. https://cds.cern.ch/record/680662.

[22] C. Alcock, *The Astrophysics and Cosmology of Quark—Gluon Plasma*, pp. 300–342. Springer Berlin Heidelberg, Berlin, Heidelberg, 1990. http://dx.doi.org/10.1007/978-3-642-75289-6_6.

[23] *New State of Matter Created at CERN*. https://press.cern/press-releases/2000/02/new-state-matter-created-cern. Published: 10.02.2000, Accessed: 19.12.2016.

[24] U. W. Heinz and M. Jacob, "Evidence for a new state of matter: An Assessment of the results from the CERN lead beam program," arXiv:nucl-th/0002042 [nucl-th].

[25] P. Braun-Munzinger and J. Stachel, "The quest for the quark-gluon plasma," *Nature* **448** (2007) 302–309.

[26] **STAR** Collaboration, J. Adams *et al.*, "Experimental and theoretical challenges in the search for the quark gluon plasma: The STAR Collaboration's critical assessment of the evidence from RHIC collisions," *Nucl. Phys.* **A757** (2005) 102–183, arXiv:nucl-ex/0501009 [nucl-ex].

[27] **PHENIX** Collaboration, K. Adcox *et al.*, "Formation of dense partonic matter in relativistic nucleus-nucleus collisions at RHIC: Experimental evaluation by the PHENIX collaboration," *Nucl. Phys.* **A757** (2005) 184–283, arXiv:nucl-ex/0410003 [nucl-ex].

[28] **BRAHMS** Collaboration, I. Arsene *et al.*, "Quark gluon plasma and color glass condensate at RHIC? The Perspective from the BRAHMS experiment," *Nucl. Phys.* **A757** (2005) 1–27, arXiv:nucl-ex/0410020 [nucl-ex].

[29] B. B. Back *et al.*, "The PHOBOS perspective on discoveries at RHIC," *Nucl. Phys.* **A757** (2005) 28–101, arXiv:nucl-ex/0410022 [nucl-ex].

[30] B. Hippolyte, "Heavy-ion session: a (quick) introduction," in *Proceedings, 48th Rencontres de Moriond on QCD and High Energy Interactions: La Thuile, Italy, March 9-16, 2013*, pp. 201–206. 2013. https://inspirehep.net/record/1268454/files/Pages_from_C13-03-09_201.pdf.

[31] J. D. Bjorken, "Highly Relativistic Nucleus-Nucleus Collisions: The Central Rapidity Region," *Phys. Rev.* **D27** (1983) 140–151.

[32] **ALICE** Collaboration, K. Aamodt *et al.*, "Two-pion Bose-Einstein correlations in central Pb-Pb collisions at $\sqrt{s_{NN}} = 2.76$ TeV," *Phys. Lett.* **B696** (2011) 328–337, arXiv:1012.4035 [nucl-ex].

[33] Y. Zhou., "Anisotropic flow measurements in Pb-Pb collisions at 5.02 TeV with ALICE," 16th International Conference on Strangeness in Quark Matter (SQM 2016) Berkeley, California, United States, June 27-July 1, 2016. https://indico.cern.ch/event/403913/contributions/1849254/attachments/1301687/1943748/YZhou_SQM_v7.pdf.

[34] **ALICE** Collaboration, J. Adam *et al.*, "Anisotropic flow of charged particles in Pb-Pb collisions at $\sqrt{s_{\rm NN}} = 5.02$ TeV," *Phys. Rev. Lett.* **116** no. 13, (2016) 132302, arXiv:1602.01119 [nucl-ex].

[35] **ALICE** Collaboration, J. Adam *et al.*, "Pseudorapidity dependence of the anisotropic flow of charged particles in Pb-Pb collisions at $\sqrt{s_{\rm NN}} = 2.76$ TeV," arXiv:1605.02035 [nucl-ex].

[36] **ALICE** Collaboration, J. Adam *et al.*, "Correlated event-by-event fluctuations of flow harmonics in Pb-Pb collisions at $\sqrt{s_{\rm NN}} = 2.76$ TeV," arXiv:1604.07663 [nucl-ex].

[37] S. Voloshin and Y. Zhang, "Flow study in relativistic nuclear collisions by Fourier expansion of Azimuthal particle distributions," *Z. Phys.* **C70** (1996) 665–672, arXiv:hep-ph/9407282 [hep-ph].

[38] **ALICE** Collaboration, B. Abelev *et al.*, "Anisotropic flow of charged hadrons, pions and (anti-)protons measured at high transverse momentum in Pb-Pb collisions at $\sqrt{s_{NN}}$=2.76 TeV," *Phys. Lett.* **B719** (2013) 18–28, arXiv:1205.5761 [nucl-ex].

[39] J. Noronha-Hostler, M. Luzum, and J.-Y. Ollitrault, "Hydrodynamic predictions for 5.02 TeV Pb-Pb collisions," *Phys. Rev.* **C93** no. 3, (2016) 034912, arXiv:1511.06289 [nucl-th].

[40] **ALICE** Collaboration, K. Aamodt *et al.*, "Higher harmonic anisotropic flow measurements of charged particles in Pb-Pb collisions at $\sqrt{s_{NN}}$=2.76 TeV," *Phys. Rev. Lett.* **107** (2011) 032301, arXiv:1105.3865 [nucl-ex].

[41] **ALICE** Collaboration, K. Aamodt *et al.*, "Elliptic flow of charged particles in Pb-Pb collisions at 2.76 TeV," *Phys. Rev. Lett.* **105** (2010) 252302, arXiv:1011.3914 [nucl-ex].

[42] **ATLAS** Collaboration, G. Aad *et al.*, "Measurement of the azimuthal anisotropy for charged particle production in $\sqrt{s_{NN}} = 2.76$ TeV lead-lead collisions with the ATLAS detector," *Phys. Rev.* **C86** (2012) 014907, arXiv:1203.3087 [hep-ex].

[43] **CDF** Collaboration, T. Aaltonen *et al.*, "Measurement of Particle Production and Inclusive Differential Cross Sections in $p\bar{p}$ Collisions at $\sqrt{s} = 1.96$-TeV," *Phys. Rev.* **D79** (2009) 112005, arXiv:0904.1098 [hep-ex]. [Erratum: Phys. Rev.D82,119903(2010)].

[44] **ALICE** Collaboration, K. Aamodt *et al.*, "Suppression of Charged Particle Production at Large Transverse Momentum in Central Pb-Pb Collisions at $\sqrt{s_{NN}} = 2.76$ TeV," *Phys. Lett.* **B696** (2011) 30–39, arXiv:1012.1004 [nucl-ex].

[45] **ALICE** Collaboration, A. Festanti, "Heavy-flavour production and nuclear modification factor in Pb-Pb collisions at $\sqrt{s_{\rm NN}}$=2.76 TeV with ALICE," *Nucl. Phys.* **A931** (2014) 514–519, arXiv:1407.6541 [nucl-ex].

[46] **ALICE** Collaboration, D. Moreira de Godoy, "Measurements of the nuclear modification factor and the elliptic azimuthal anisotropy of heavy flavours with ALICE," *J. Phys. Conf. Ser.* **458** (2013) 012013.

[47] M. L. Miller, K. Reygers, S. J. Sanders, and P. Steinberg, "Glauber modeling in high energy nuclear collisions," *Ann. Rev. Nucl. Part. Sci.* **57** (2007) 205–243, arXiv:nucl-ex/0701025 [nucl-ex].

[48] **PHENIX** Collaboration, S. S. Adler *et al.*, "High p_T charged hadron suppression in Au + Au collisions at $\sqrt{s}_{NN} = 200$ GeV," *Phys. Rev.* **C69** (2004) 034910, arXiv:nucl-ex/0308006 [nucl-ex].

[49] **STAR** Collaboration, J. Adams *et al.*, "Transverse momentum and collision energy dependence of high p(T) hadron suppression in Au+Au collisions at ultrarelativistic energies," *Phys. Rev. Lett.* **91** (2003) 172302, arXiv:nucl-ex/0305015 [nucl-ex].

[50] J. W. Cronin, H. J. Frisch, M. J. Shochet, J. P. Boymond, R. Mermod, P. A. Piroue, and R. L. Sumner, "Production of hadrons with large transverse momentum at 200, 300, and 400 GeV," *Phys. Rev.* **D11** (1975) 3105–3123.

[51] B. Z. Kopeliovich, J. Nemchik, A. Schafer, and A. V. Tarasov, "Cronin effect in hadron production off nuclei," *Phys. Rev. Lett.* **88** (2002) 232303, arXiv:hep-ph/0201010 [hep-ph].

[52] **ALICE** Collaboration, B. B. Abelev *et al.*, "Transverse momentum dependence of inclusive primary charged-particle production in p-Pb collisions at $\sqrt{s_{\rm NN}} = 5.02$ TeV," *Eur. Phys. J.* **C74** no. 9, (2014) 3054, arXiv:1405.2737 [nucl-ex].

[53] **CMS** Collaboration, S. Chatrchyan *et al.*, "Study of high-pT charged particle suppression in PbPb compared to pp collisions at $\sqrt{s_{NN}} = 2.76$ TeV," *Eur. Phys. J.* **C72** (2012) 1945, arXiv:1202.2554 [nucl-ex].

[54] **CMS** Collaboration, S. Chatrchyan *et al.*, "Study of Z boson production in PbPb collisions at $\sqrt{s_{NN}}$ = 2.76 TeV," *Phys. Rev. Lett.* **106** (2011) 212301, arXiv:1102.5435 [nucl-ex].

[55] **CMS** Collaboration, S. Chatrchyan *et al.*, "Study of W boson production in PbPb and pp collisions at $\sqrt{s_{NN}} = 2.76$ TeV," *Phys. Lett.* **B715** (2012) 66–87, arXiv:1205.6334 [nucl-ex].

[56] **CMS** Collaboration, S. Chatrchyan *et al.*, "Measurement of isolated photon production in pp and PbPb collisions at $\sqrt{s_{NN}} = 2.76$ TeV," *Phys. Lett.* **B710** (2012) 256–277, arXiv:1201.3093 [nucl-ex].

[57] N. Brambilla *et al.*, "QCD and Strongly Coupled Gauge Theories: Challenges and Perspectives," *Eur. Phys. J.* **C74** no. 10, (2014) 2981, arXiv:1404.3723 [hep-ph].

[58] **CMS** Collaboration, S. Chatrchyan *et al.*, "Observation and studies of jet quenching in PbPb collisions at nucleon-nucleon center-of-mass energy = 2.76 TeV," *Phys. Rev.* **C84** (2011) 024906, arXiv:1102.1957 [nucl-ex].

[59] J. D. Bjorken, "Energy Loss of Energetic Partons in Quark - Gluon Plasma: Possible Extinction of High p(t) Jets in Hadron - Hadron Collisions,"

FERMILAB-PUB-82-059-THY (1982) .
http://inspirehep.net/record/181746.

[60] **ATLAS** Collaboration, G. Aad *et al.*, "Observation of a Centrality-Dependent Dijet Asymmetry in Lead-Lead Collisions at $\sqrt{s_{NN}} = 2.77$ TeV with the ATLAS Detector at the LHC," *Phys. Rev. Lett.* **105** (2010) 252303, arXiv:1011.6182 [hep-ex].

[61] **ALICE** Collaboration, K. Aamodt *et al.*, "Particle-yield modification in jet-like azimuthal di-hadron correlations in Pb-Pb collisions at $\sqrt{s_{NN}} = 2.76$ TeV," *Phys. Rev. Lett.* **108** (2012) 092301, arXiv:1110.0121 [nucl-ex].

[62] **STAR** Collaboration, J. Adams *et al.*, "Direct observation of dijets in central Au+Au collisions at s(NN)**(1/2) = 200-GeV," *Phys. Rev. Lett.* **97** (2006) 162301, arXiv:nucl-ex/0604018 [nucl-ex].

[63] F.-M. Liu and S.-X. Liu, "Quark-gluon plasma formation time and direct photons from heavy ion collisions," *Phys. Rev.* **C89** no. 3, (2014) 034906, arXiv:1212.6587 [nucl-th].

[64] **ALICE** Collaboration, J. Adam *et al.*, "Transverse momentum dependence of D-meson production in Pb-Pb collisions at $\sqrt{\mathrm{s_{NN}}} = 2.76$ TeV," *JHEP* **03** (2016) 081, arXiv:1509.06888 [nucl-ex].

[65] A. Andronic *et al.*, "Heavy-flavour and quarkonium production in the LHC era: from proton–proton to heavy-ion collisions," *Eur. Phys. J.* **C76** no. 3, (2016) 107, arXiv:1506.03981 [nucl-ex].

[66] M. G. Mustafa, "Energy loss of charm quarks in the quark-gluon plasma: Collisional versus radiative," *Phys. Rev.* **C72** (2005) 014905, arXiv:hep-ph/0412402 [hep-ph].

[67] R. Averbeck, "Heavy-flavor production in heavy-ion collisions and implications for the properties of hot QCD matter," *Prog. Part. Nucl. Phys.* **70** (2013) 159–209, arXiv:1505.03828 [nucl-ex].

[68] M. Djordjevic and U. W. Heinz, "Radiative energy loss in a finite dynamical QCD medium," *Phys. Rev. Lett.* **101** (2008) 022302, arXiv:0802.1230 [nucl-th].

[69] M. Djordjevic, "Theoretical formalism of radiative jet energy loss in a finite size dynamical QCD medium," *Phys. Rev.* **C80** (2009) 064909, arXiv:0903.4591 [nucl-th].

[70] M. Djordjevic, "Collisional energy loss in a finite size QCD matter," *Phys. Rev.* **C74** (2006) 064907, arXiv:nucl-th/0603066 [nucl-th].

[71] Y. L. Dokshitzer and D. E. Kharzeev, "Heavy quark colorimetry of QCD matter," *Phys. Lett.* **B519** (2001) 199–206, arXiv:hep-ph/0106202 [hep-ph].

[72] **ALICE** Collaboration, B. Abelev *et al.*, "Measurement of charm production at central rapidity in proton-proton collisions at $\sqrt{s} = 7$ TeV," *JHEP* **01** (2012) 128, arXiv:1111.1553 [hep-ex].

[73] **ALICE** Collaboration, "Measurement of electrons from semileptonic heavy-flavour hadron decays in pp collisions at $\sqrt{s}$=7 TeV," *Phys. Rev. Lett.* **D86** (2012) 112007, arXiv:1205.5423 [hep-ex].

[74] **ALICE** Collaboration, B. Abelev *et al.*, "Measurement of electrons from beauty hadron decays in pp collisions at $\sqrt{s} = 7$ TeV," *Phys. Lett.* **B721** (2013) 13–23, arXiv:1208.1902 [hep-ex].

[75] B. A. Kniehl, G. Kramer, I. Schienbein, and H. Spiesberger, "Reconciling open charm production at the Fermilab Tevatron with QCD," *Phys. Rev. Lett.* **96** (2006) 012001, arXiv:hep-ph/0508129 [hep-ph].

[76] B. A. Kniehl, G. Kramer, I. Schienbein, and H. Spiesberger, "Inclusive Charmed-Meson Production at the CERN LHC," *Eur. Phys. J.* **C72** (2012) 2082, arXiv:1202.0439 [hep-ph].

[77] M. Cacciari, M. Greco, and P. Nason, "The P(T) spectrum in heavy flavor hadroproduction," *JHEP* **05** (1998) 007, arXiv:hep-ph/9803400 [hep-ph].

[78] M. Cacciari, S. Frixione, N. Houdeau, M. L. Mangano, P. Nason, and G. Ridolfi, "Theoretical predictions for charm and bottom production at the LHC," *JHEP* **10** (2012) 137, arXiv:1205.6344 [hep-ph].

[79] **ATLAS** Collaboration, G. Aad *et al.*, "Measurements of the electron and muon inclusive cross-sections in proton-proton collisions at $\sqrt{s} = 7$ TeV with the ATLAS detector," *Phys. Lett.* **B707** (2012) 438–458, arXiv:1109.0525 [hep-ex].

[80] **ALICE** Collaboration, J. Adam *et al.*, "D-meson production in p-Pb collisions at $\sqrt{s_{\rm NN}} = 5.02$ TeV and in pp collisions at $\sqrt{s} = 7$ TeV," arXiv:1605.07569 [nucl-ex].

[81] **ALICE** Collaboration, B. B. Abelev *et al.*, "Production of charged pions, kaons and protons at large transverse momenta in pp and Pb–Pb collisions at $\sqrt{s_{\rm NN}}$ =2.76 TeV," *Phys. Lett.* **B736** (2014) 196–207, arXiv:1401.1250 [nucl-ex].

[82] **ALICE** Collaboration, B. Abelev *et al.*, "Centrality Dependence of Charged Particle Production at Large Transverse Momentum in Pb–Pb Collisions at $\sqrt{s_{\rm NN}} = 2.76$ TeV," *Phys. Lett.* **B720** (2013) 52–62, arXiv:1208.2711 [hep-ex].

[83] M. Djordjevic, M. Djordjevic, and B. Blagojevic, "RHIC and LHC jet suppression in non-central collisions," *Phys. Lett.* **B737** (2014) 298–302, arXiv:1405.4250 [nucl-th].

[84] S. Wicks, W. Horowitz, M. Djordjevic, and M. Gyulassy, "Elastic, inelastic, and path length fluctuations in jet tomography," *Nucl. Phys.* **A784** (2007) 426–442, arXiv:nucl-th/0512076 [nucl-th].

[85] W. A. Horowitz and M. Gyulassy, "The Surprising Transparency of the sQGP at LHC," *Nucl. Phys.* **A872** (2011) 265–285, arXiv:1104.4958 [hep-ph].

[86] W. A. Horowitz, "Testing pQCD and AdS/CFT Energy Loss at RHIC and LHC," *AIP Conf. Proc.* **1441** (2012) 889–891, arXiv:1108.5876 [hep-ph].

[87] J. Xu, J. Liao, and M. Gyulassy, "Consistency of Perfect Fluidity and Jet Quenching in semi-Quark-Gluon Monopole Plasmas," *Chin. Phys. Lett.* **32** no. 9, (2015) 092501, arXiv:1411.3673 [hep-ph].

[88] J. Xu, J. Liao, and M. Gyulassy, "Bridging Soft-Hard Transport Properties of Quark-Gluon Plasmas with CUJET3.0," *JHEP* **02** (2016) 169, arXiv:1508.00552 [hep-ph].

[89] M. Nahrgang, J. Aichelin, P. B. Gossiaux, and K. Werner, "Influence of hadronic bound states above T_c on heavy-quark observables in Pb + Pb collisions at at the CERN Large Hadron Collider," *Phys. Rev.* **C89** no. 1, (2014) 014905, arXiv:1305.6544 [hep-ph].

[90] J. Uphoff, O. Fochler, Z. Xu, and C. Greiner, "Elliptic Flow and Energy Loss of Heavy Quarks in Ultra-Relativistic heavy Ion Collisions," *Phys. Rev.* **C84** (2011) 024908, arXiv:1104.2295 [hep-ph].

[91] O. Fochler, J. Uphoff, Z. Xu, and C. Greiner, "Jet quenching and elliptic flow at RHIC and LHC within a pQCD-based partonic transport model," *J. Phys.* **G38** (2011) 124152, arXiv:1107.0130 [hep-ph].

[92] J. Uphoff, O. Fochler, Z. Xu, and C. Greiner, "Open Heavy Flavor in Pb+Pb Collisions at $\sqrt{s} = 2.76$ TeV within a Transport Model," *Phys. Lett.* **B717** (2012) 430–435, arXiv:1205.4945 [hep-ph].

[93] S. Cao, G.-Y. Qin, and S. A. Bass, "Heavy-quark dynamics and hadronization in ultrarelativistic heavy-ion collisions: Collisional versus radiative energy loss," *Phys. Rev.* **C88** (2013) 044907, arXiv:1308.0617 [nucl-th].

[94] W. M. Alberico, A. Beraudo, A. De Pace, A. Molinari, M. Monteno, M. Nardi, and F. Prino, "Heavy-flavour spectra in high energy nucleus-nucleus collisions," *Eur. Phys. J.* **C71** (2011) 1666, arXiv:1101.6008 [hep-ph].

[95] A. Beraudo, A. De Pace, M. Monteno, M. Nardi, and F. Prino, "Heavy flavors in heavy-ion collisions: quenching, flow and correlations," *Eur. Phys. J.* **C75** no. 3, (2015) 121, arXiv:1410.6082 [hep-ph].

[96] M. He, R. J. Fries, and R. Rapp, "Heavy Flavor at the Large Hadron Collider in a Strong Coupling Approach," *Phys. Lett.* **B735** (2014) 445–450, arXiv:1401.3817 [nucl-th].

[97] T. Song, H. Berrehrah, D. Cabrera, W. Cassing, and E. Bratkovskaya, "Charm production in Pb + Pb collisions at energies available at the CERN Large Hadron Collider," *Phys. Rev.* **C93** no. 3, (2016) 034906, arXiv:1512.00891 [nucl-th].

[98] R. Sharma, I. Vitev, and B.-W. Zhang, "Light-cone wave function approach to open heavy flavor dynamics in QCD matter," *Phys. Rev.* **C80** (2009) 054902, arXiv:0904.0032 [hep-ph].

[99] **ALICE** Collaboration, B. B. Abelev *et al.*, "Azimuthal anisotropy of D meson production in Pb-Pb collisions at $\sqrt{s_{\rm NN}} = 2.76$ TeV," *Phys. Rev.* **C90** no. 3, (2014) 034904, arXiv:1405.2001 [nucl-ex].

[100] **STAR** Collaboration, L. Adamczyk *et al.*, "Observation of D^0 Meson Nuclear Modifications in Au+Au collisions at $\sqrt{s_{NN}} = 200$ GeV," *Phys. Rev. Lett.* **113** no. 14, (2014) 142301, arXiv:1404.6185 [nucl-ex].

[101] **ALICE** Collaboration, "Measurement of Prompt D-Meson Production in p–Pb Collisions at $\sqrt{S_{NN}}$=5.02 TeV," *Phys. Rev. Lett.* **113** (2014) 232301, arXiv:1405.3452 [nucl-ex].

[102] **ALICE** Collaboration, B. Abelev *et al.*, "D meson elliptic flow in non-central Pb-Pb collisions at $\sqrt{s_{\rm NN}}$ = 2.76TeV," *Phys. Rev. Lett.* **111** (2013) 102301, arXiv:1305.2707 [nucl-ex].

[103] S. Batsouli, S. Kelly, M. Gyulassy, and J. L. Nagle, "Does the charm flow at RHIC?," *Phys. Lett.* **B557** (2003) 26–32, arXiv:nucl-th/0212068 [nucl-th].

[104] V. Greco, C. M. Ko, and R. Rapp, "Quark coalescence for charmed mesons in ultrarelativistic heavy ion collisions," *Phys. Lett.* **B595** (2004) 202–208, arXiv:nucl-th/0312100 [nucl-th].

[105] A. Festanti, *Measurement of the* $\rm D^0$ *meson production in Pb-Pb and p-Pb collisions with the ALICE experiment at the LHC*. PhD thesis, Padua U., Feb, 2015. https://cds.cern.ch/record/2057663.

[106] M. Bedjidian *et al.*, "Hard probes in heavy ion collisions at the LHC: Heavy flavor physics," 2004. arXiv:hep-ph/0311048 [hep-ph]. http://doc.cern.ch/cernrep/2004/2004-009/2004-009.html.

[107] E. Norrbin and T. Sjostrand, "Production and hadronization of heavy quarks," *Eur. Phys. J.* **C17** (2000) 137–161, arXiv:hep-ph/0005110 [hep-ph].

[108] M. L. Mangano, P. Nason, and G. Ridolfi, "Heavy quark correlations in hadron collisions at next-to-leading order," *Nucl. Phys.* **B373** (1992) 295–345.

[109] F. Colamaria and G. E. Bruno, *Measurements of D-hadron azimuthal correlations with ALICE at the LHC*. PhD thesis, U. Bari (main), 2014. https://cds.cern.ch/record/1702282. Presented 16 May 2014.

[110] M. Nahrgang, J. Aichelin, P. B. Gossiaux, and K. Werner, "Heavy-flavor azimuthal correlations of D mesons," *J. Phys. Conf. Ser.* **509** (2014) 012047, arXiv:1310.2218 [hep-ph].

[111] T. Renk, "Charm-energy loss and D - D correlations from a parton shower approach," *Phys. Rev.* **C89** no. 5, (2014) 054906, arXiv:1310.5458 [hep-ph].

[112] A. Mischke, "A New correlation method to identify and separate charm and bottom production processes at RHIC," *Phys. Lett.* **B671** (2009) 361–365, arXiv:0807.1309 [hep-ph].

[113] **ALICE** Collaboration, J. Adam *et al.*, "Measurement of azimuthal correlations of D mesons and charged particles in pp collisions at $\sqrt{s} = 7$ TeV and p-Pb collisions at $\sqrt{s_{\rm NN}} = 5.02$ TeV," arXiv:1605.06963 [nucl-ex].

[114] **ALICE** Collaboration, F. Colamaria, "Heavy-flavour production in pp collisions and correlations in pp and p-Pb collisions measured with ALICE at the LHC," 2016. arXiv:1609.08309 [hep-ex]. https://inspirehep.net/record/1488277/files/arXiv:1609.08309.pdf.

[115] **STAR** Collaboration, M. M. Aggarwal *et al.*, "Measurement of the Bottom contribution to non-photonic electron production in $p + p$ collisions at $\sqrt{s}$=200 GeV," *Phys. Rev. Lett.* **105** (2010) 202301, arXiv:1007.1200 [nucl-ex].

[116] **ALICE** Collaboration, B. B. Abelev *et al.*, "Beauty production in pp collisions at $\sqrt{s}$ = 2.76 TeV measured via semi-electronic decays," *Phys. Lett.* **B738** (2014) 97–108, arXiv:1405.4144 [nucl-ex].

[117] X.-y. Lin, "Charm fragmentation function and electron spectra for D and B meson semi-leptonic decays using PYTHIA calculations of p+p collisions," arXiv:hep-ph/0602067 [hep-ph].

[118] S. Altinpinar, *Electron-D0 Correlations With ALICE In pp Collisions At LHC Energy*. PhD thesis, Technische Universität, Darmstadt, 2012. http://tuprints.ulb.tu-darmstadt.de/3140/.

[119] **STAR** Collaboration, A. Mischke, "Heavy-flavor correlation measurements via electron azimuthal correlations with open charm mesons," *J. Phys.* **G35** (2008) 044022, arXiv:0710.2599 [nucl-ex].

[120] O. S. Bruning, P. Collier, P. Lebrun, S. Myers, R. Ostojic, J. Poole, and P. Proudlock, "LHC Design Report Vol.1: The LHC Main Ring,".

[121] L. Evans and P. Bryant, "LHC Machine," *JINST* **3** (2008) S08001.

[122] V. Frigo, "LHC map in 3D. Schéma du LHC en 3D". AC Collection. Legacy of AC. Pictures from 1992 to 2002, Mar, 1997. https://cds.cern.ch/record/842700.

[123] **ATLAS** Collaboration, G. Aad *et al.*, "Observation of a new particle in the search for the Standard Model Higgs boson with the ATLAS detector at the LHC," *Phys. Lett.* **B716** (2012) 1–29, arXiv:1207.7214 [hep-ex].

[124] **CMS** Collaboration, S. Chatrchyan *et al.*, "Observation of a new boson at a mass of 125 GeV with the CMS experiment at the LHC," *Phys. Lett.* **B716** (2012) 30–61, arXiv:1207.7235 [hep-ex].

[125] **ALICE** Collaboration, K. Aamodt *et al.*, "The ALICE experiment at the CERN LHC," *JINST* **3** (2008) S08002.

[126] **ALICE** Collaboration, B. Abelev *et al.*, "Performance of the ALICE Experiment at the CERN LHC," *Int. J. Mod. Phys.* **A29** (2014) 1430044, arXiv:1402.4476 [nucl-ex].

[127] **ALICE** Collaboration, K. Aamodt *et al.*, "Alignment of the ALICE Inner Tracking System with cosmic-ray tracks," *JINST* **5** (2010) P03003, arXiv:1001.0502 [physics.ins-det].

[128] **ALICE** Collaboration, C. Lippmann, "Upgrade of the ALICE Time Projection Chamber,".

[129] J. Alme *et al.*, "The ALICE TPC, a large 3-dimensional tracking device with fast readout for ultra-high multiplicity events," *Nucl. Instrum. Meth.* **A622** (2010) 316–367, arXiv:1001.1950 [physics.ins-det].

[130] **ALICE** Collaboration, P. Cortese *et al.*, "ALICE: Physics performance report, volume I," *J. Phys.* **G30** (2004) 1517–1763.

[131] **ALICE** Collaboration, J. Klein, "The ALICE Transition Radiation Detector: status and perspectives for Run II," arXiv:1601.00493 [physics.ins-det].

[132] **ALICE** Collaboration, J. Klein, "Triggering with the ALICE TRD," *Nucl. Instrum. Meth.* **A706** (2013) 23–28, arXiv:1112.5110 [nucl-ex].

[133] A. Akindinov *et al.*, "Performance of the ALICE Time-Of-Flight detector at the LHC," *Eur. Phys. J. Plus* **128** (2013) 44.

[134] **ALICE EMCal** Collaboration, J. Allen *et al.*, "Performance of prototypes for the ALICE electromagnetic calorimeter," *Nucl. Instrum. Meth.* **A615** (2010) 6–13, arXiv:0912.2005 [physics.ins-det].

[135] J. Allen *et al.*, "ALICE DCal: An Addendum to the EMCal Technical Design Report Di-Jet and Hadron-Jet correlation measurements in ALICE," Tech. Rep. CERN-LHCC-2010-011. ALICE-TDR-14-add-1, Jun, 2010. https://cds.cern.ch/record/1272952.

[136] **ALICE** Collaboration, E. Abbas *et al.*, "Performance of the ALICE VZERO system," *JINST* **8** (2013) P10016, arXiv:1306.3130 [nucl-ex].

[137] C. Lippmann, "Particle identification," *Nucl. Instrum. Meth.* **A666** (2012) 148–172, arXiv:1101.3276 [hep-ex].

[138] W. Blum, W. Riegler, and L. Rolandi, *Particle detection with drift chambers; 2nd ed.* Springer, Berlin, 2008. http://dx.doi.org/10.1007/978-3-540-76684-1.

[139] **ALICE** Collaboration, A. Alici, "Particle identification with the ALICE Time-Of-Flight detector at the LHC," *Nuclear Instruments and Methods in Physics Research A* **766** (2014) 288–291.

[140] **ALICE** Collaboration, J. Adam *et al.*, "Measurement of electrons from heavy-flavour hadron decays in p-Pb collisions at $\sqrt{s_{\rm NN}} = 5.02$ TeV," *Phys. Lett.* **B754** (2016) 81–93, arXiv:1509.07491 [nucl-ex].

[141] **ALICE** Collaboration, B. B. Abelev *et al.*, "Measurement of prompt D-meson production in $p - Pb$ collisions at $\sqrt{s_{NN}}$ = 5.02 TeV," *Phys. Rev. Lett.* **113** no. 23, (2014) 232301, arXiv:1405.3452 [nucl-ex].

[142] **ALICE** Collaboration, B. B. Abelev *et al.*, "Measurement of visible cross sections in proton-lead collisions at $\sqrt{s_{\rm NN}}$ = 5.02 TeV in van der Meer scans with the ALICE detector," *JINST* **9** no. 11, (2014) P11003, arXiv:1405.1849 [nucl-ex].

[143] **ALICE** Collaboration, B. Abelev *et al.*, "Measurement of charm production at central rapidity in proton-proton collisions at $\sqrt{s} = 7$ TeV," *JHEP* **01** (2012) 128, arXiv:1111.1553 [hep-ex].

[144] **ALICE** Collaboration, J. Adam *et al.*, "D-meson production in p-Pb collisions at $\sqrt{s_{\rm NN}} = 5.02$ TeV and in pp collisions at $\sqrt{s} = 7$ TeV," arXiv:1605.07569 [nucl-ex].

[145] **STAR** Collaboration, B. I. Abelev *et al.*, "Transverse momentum and centrality dependence of high-p_T non-photonic electron suppression in Au+Au collisions at $\sqrt{s_{NN}} = 200\,\text{GeV}$," *Phys. Rev. Lett.* **98** (2007) 192301, arXiv:nucl-ex/0607012. [Erratum: Phys. Rev. Lett.106,159902(2011)].

[146] **ALICE** Collaboration, D. Thomas, "Azimuthal angular correlations between heavy-flavour decay electrons and charged hadrons in pp collisions at $\sqrt{s} = 2.76$ TeV in ALICE," *Nucl. Phys.* **A910-911** (2013) 205–206, arXiv:1208.1181 [hep-ex].

[147] *LHC long term schedule*. https://lhc-commissioning.web.cern.ch/lhc-commissioning/schedule/LHC-long-term.htm. Accessed: 10.05.2016.

[148] **ALICE** Collaboration, B. Abelev *et al.*, "Upgrade of the ALICE Experiment: Letter Of Intent," *J. Phys.* **G41** (2014) 087001.

[149] **ALICE** Collaboration, R. Tieulent, "ALICE Upgrades: Plans and Potentials," in *3rd Large Hadron Collider Physics Conference (LHCP 2015) St. Petersburg, Russia,*

August 31-September 5, 2015. 2015. arXiv:1512.02253 [nucl-ex]. https://inspirehep.net/record/1408783/files/arXiv:1512.02253.pdf.

[150] **ALICE** Collaboration, P. Riedler, "Upgrade of the ALICE Inner Tracking System," *Nucl. Phys.* **A956** (2016) 866–869.

[151] **ALICE** Collaboration, B. Abelev *et al.*, "Technical Design Report for the Upgrade of the ALICE Inner Tracking System," *J. Phys.* **G41** (2014) 087002.

[152] **ALICE** Collaboration, P.-I. Lonne, *Analysis of D-h and D-e angular correlations with ALICE, and perspectives for the upgrade*, 2014. https://indico.cern.ch/event/219436/contributions/1523474/.

[153] M. Gyulassy and X.-N. Wang, "HIJING 1.0: A Monte Carlo program for parton and particle production in high-energy hadronic and nuclear collisions," *Comput. Phys. Commun.* **83** (1994) 307, arXiv:nucl-th/9502021 [nucl-th].

[154] T. Sjostrand, S. Mrenna, and P. Z. Skands, "PYTHIA 6.4 Physics and Manual," *JHEP* **05** (2006) 026, arXiv:hep-ph/0603175 [hep-ph].

[155] *ALICE Offline Pages*. http://aliceinfo.cern.ch/Offline/. Accessed: 28.11.2016.

[156] *About CERN*. https://home.cern/about. Accessed: 03.07.2016.

[157] *Wit Busza Interivew - Special Topic of Hadron Colliders*. http://archive.sciencewatch.com/ana/st/hadron/11aprSThadBNL/. Accessed: 12.09.2016.

[158] *What does ROOT stand for?* https://root.cern.ch/root/roottalk/roottalk98/0718.html. Accessed: 12.09.2016.

[159] P. Z. Skands, "Tuning Monte Carlo Generators: The Perugia Tunes," *Phys. Rev.* **D82** (2010) 074018, arXiv:1005.3457 [hep-ph].

[160] R. Brun, F. Bruyant, F. Carminati, S. Giani, M. Maire, A. McPherson, G. Patrick, and L. Urban, *GEANT: Detector Description and Simulation Tool; Oct 1994*. CERN

Program Library. CERN, Geneva, 1993.
http://cds.cern.ch/record/1082634. Long Writeup W5013.

[161] R. Brun and F. Rademakers, "ROOT: An object oriented data analysis framework," *Nucl. Instrum. Meth.* **A389** (1997) 81–86.

[162] *AliPhysics: Main Page*. http://alidoc.cern.ch/AliPhysics/master/. Accessed: 28.11.2016.

Glossary

ACORDE ALICE COsmic Ray DEtector. Detector of ALICE.

ALEPH Apparatus for LEP PHysics at CERN.

ALICE A Large Ion Collider Experiment. Dedicated heavy-ion experiment at LHC.

AliPhysics AliPhysics contains the analysis-specific code for various analyses of ALICE, using ALICE Off-line as its core.

AliRoot AliRoot is the ALICE Offline framework, used for simulation, analysis and reconstruction. The framework uses ROOT as a foundation, on which the framework and all applications are built [155].

ATLAS A Toroidal LHC ApparatuS. General purpose experiment at LHC.

BNL Brookhaven National Laboratory.

BR Branching Ratio. The fraction of particles that decay via a specific decay mode, with respect to the total number decays.

BRAHMS Broad RAnge Hadron Magnetic Spectrometers. Experiment at RHIC.

CERN The European Organization for Nuclear Research. The name CERN is derived from the acronym for the French "Conseil Européen pour la Recherche Nucléaire", or European Council for Nuclear Research, a provisional body founded in 1952 with the mandate of establishing a world-class fundamental physics research organization in Europe [156].

CMS Compact Muon Solenoid. General purpose experiment at LHC.

CNM Cold Nuclear Matter effects, i.e., effects caused by the structure of the initial state of a particle collision, e.g., the additional effects of a lead nucleus in a p–Pb collision, compared to a pp collision.

CP Charge Parity.

CPV Charged-Particle Veto detector. Part of the PHOS detector of ALICE.

DCA The Distance of Closest Approach (DCA) between two tracks is the length of a segment minimizing the distance between two track trajectories. Two tracks with a common vertex should have dca = 0. The measured dca is determined by the resolution on the track position. Definition from [105].

DCal Di-jet Calorimeter. Detector of ALICE, installed during the Long Shutdown (LS1) between LHC Run 1 and Run 2.

EMCal ElectroMagnetic Calorimeter. Detector of ALICE.

FMD Forward Multiplicity Detector. Detector of ALICE.

FONLL Fixed Order with Next-to-Leading-Log Resummation FONLL.

GEANT GEometry ANd Tracking. Software used for propagating particles through matter, e.g., a simulated detector.

GEM Gas Electron Multiplier.

GM-VFNS General-Mass Variable-Flavor-Number.

HFE Heavy Flavor Electrons (HFE) are electrons originating from Heavy-Flavor hadron decays, e.g., the decay of a D^0 meson.

HIJING Heavy Ion Jet INteraction Generator. Monte Carlo model.

HMPID High Momentum Particle Identification. Detector of ALICE.

IP Interaction Point.

ITS Inner Tracking System. Detector of ALICE.

kFirst A track selection cut which requires a hit in the first layer of the SPD.

LHC Large Hadron Collider.

LHCb Large Hadron Collider beauty. Experiment at LHC.

LQCD Lattice Quantum Chromo Dynamics LQCD).

LS Like-sign pairs are pairs of electrons with the same charge, i.e., e^-e^- or e^+e^+.

LS1 Long Shutdown 1, the period between LHC Run 1 and Run 2.

MAPS Monolithic Active Pixel Sensor.

MC Monte Carlo, a method for simulating particle collision events.

MNR Mangano, Nason and Ridolfi – pQCD predictions at NLO precision.

MRPC Multigap Resistive Plate Chamber.

MWPC Multi Wire Proportional Chamber.

ndf Number of Degrees of Freedom.

NLO Next-to-Leading Order.

PHENIX Pioneering High Energy Nuclear Interaction eXperiment. Experiment at RHIC.

PHOBOS Experiment at RHIC. Named after the Phobos moon of Mars, after the originally planned Modular Array for RHIC Spectra (MARS) was considered too expensive, and the reduced version (PHOBOS) was built instead [157].

PHOS PHOton Spectrometer. Detector of ALICE.

PID Particle Identification.

PMD Photon Multiplicity Detector. Detector of ALICE.

pQCD Pertubative Quantum Chromo Dynamics.

PWG-HF-HFCJ HFCJ is a Physics Analysis Group (PAG) dedicated to Heavy Flavour Correlations and Jets, and is a subgroup of the Heavy Flavour (HF) Physics Working Group (PWG), PWG-HF, at ALICE.

PYTHIA Program for generating high-energy physics events.

QCD Quantum Chromo Dynamics (QCD) describes the strong interaction, and is the SU(3) component of the SU(3)xSU(2)xSU(1) Standard Model of Physics.

QED Quantum Electro Dynamics.

QGP Quark Gluon Plasma (QGP) is a state of deconfined strongly interacting matter, believed to be constituting the Universe about 1 μs after the Big Bang.

RHIC Relativistic Heavy Ion Collider. Heavy ion collider located at BNL.

ROOT While not having an official acronym, Rene Brun has mentioned that "A possible acronym for the system could be "Rapid Object-Oriented Technology"" [158]. The framework provides the "roots" for end-user applications.

SDD Silicon Drift Detector. Detector of ALICE. Two middle layers of the ITS.

SPD The Silicon Pixel Detector (SPD) is the innermost detector of alice. The SPD constitutes the two first layers of the ITS. Detector of ALICE.

SPS Super Proton Synchrotron. Final acceleration stage before particles enter the LHC at CERN, accelerating protons up to 450 GeV/c.

SSD Silicon Strip Detector. Detector of ALICE. Two outermost layers of the ITS.

STAR Solenoidal Tracker At RHIC. Experiment at RHIC.

T0 Time-Zero (T0, TZERO). Detector of ALICE, determines the start time (T0) of collisions.

TOF Time of Flight detector. Detector of ALICE.

TPC Time Projection Chamber. Detector of ALICE.

TRD Transition Radiation Detector. Detector of ALICE.

ULS Unlike-sign pairs are pairs of electrons with opposite charge, i.e., $\mathrm{e}^{+}\mathrm{e}^{-}$.

V0 Veto (V0, VZERO). Detector of ALICE.

WLCG Worldwide LHC Computing Grid. Distributed computing. Global collaboration of computing centers.

ZDC Zero Degree Calorimeter. Detector of ALICE.

Appendix A

Data Sets

The data sets used to create the results in this thesis are presented briefly in this appendix. These results are marked as "Results of this thesis" throughout the thesis, and contain labels indicating if the results are from data or simulations, i.e.,:

- p–Pb $\sqrt{s_{\mathrm{NN}}} = 5.02\,\mathrm{TeV}$ (Data).
- p–Pb $\sqrt{s_{\mathrm{NN}}} = 5.02\,\mathrm{TeV}$ (Simulation).

The details of the dataset containing recorded events (Data), and that containing simulated events (Simulation), will be summarized in the following.

A.1 p–Pb $\sqrt{\mathrm{s_{NN}}} = 5.02\,\mathrm{TeV}$ (Data)

The data analysed in this thesis was taken during the 2013 p–Pb run, and consists of two run periods, labeled *LHC13b* and *LHC13c* by ALICE. A summary of the run periods with their run numbers, number of events and production information is seen in Table A.1. Due to the different reconstruction passes for LHC13b and LHC13c, electron selection efficiency maps were calculated and applied individually for the two run periods, before combining the corrected samples.

Table A.1: Overview of the LHC13b and LHC13c data samples. The number of events is extracted from the analysis over the given run numbers.

Type	Production	Run numbers	Events
Data	LHC13b pass3/AOD154	195483, 195482, 195481, 195480, 195479, 195478, 195391, 195390, 195389, 195351, 195346, 195344	29M
Data	LHC13b pass2/AOD154	195677, 195676, 195675, 195673, 195644, 195635, 195633, 195596, 195593, 195592, 195568, 195567, 195566, 195532, 195531, 195529	86M

A.2 p–Pb $\sqrt{s_{NN}} = 5.02\,\mathrm{TeV}$ (Simulation)

The Monte Carlo simulation used in this thesis is labeled *LHC13d3* by ALICE. The simulation consists of an underlying sample of p–Pb collisions generated with HIJING v1.36 [153], enhanced with one $c\bar{c}$ or $b\bar{b}$ pair decaying semileptonically per event, using the PYTHIA v6.4.21 [154] generator with the Perugia-0 tune [159] [140]. The generated particles were propagated through the apparatus using GEANT3 [160] and a realistic detector response was applied to reproduce the performance of the detector system during the 2013 p–Pb data taking period. An overview of the run numbers used can be seen in Table A.2, indicating which reconstruction pass is used, which run period from the 2013 data taking the simulation is anchored to, and the total number of events contained in these samples. The LHC13d3 sample can be used as a Minimum Bias (MB) sample if only the HIJING component is considered.

Table A.2: Overview of the LHC13d3 Monte Carlo sample. The number of events is extracted from the analysis over the given run numbers.

Type	Production	Anchor	Run numbers	Events
Monte-Carlo	LHC13d3 AOD159	LHC13b pass3	195483, 195482, 195481, 195480, 195479, 195478, 195391, 195389	9.5M
Monte-Carlo	LHC13d3 AOD159	LHC13c pass2	195677, 195675, 195673, 195644, 195635, 195633, 195596, 195593, 195592, 195568, 195567, 195566, 195531, 195529	29.4M

Appendix B

Detector subsystems in ALICE

Table B.1: The ALICE detectors. The transverse (for HMPID, radial) and longitudinal coordinates r, z are measured with respect to the ALICE interaction point (IP2). The z axis points along the anticlockwise LHC beam. The detectors marked with an asterisk (*) are used for triggering. As of 2013, 13/18 of the TRD modules and 3/5 of the PHOS modules have been installed, while 18/18 and 4/5 modules were installed during LHC Run 2. The DCal detector was installed during the long shutdown between Run 1 and Run 2. The ZDCs were moved from $|z| \simeq 114.0$ m to $|z| \simeq 112.5$ m during the winter shutdown 2011/2012. The η and φ ranges specified for the proton ZDC are purely geometrical and do not take into account how charged particles are transported through the magnetic elements of the beam line. Modified table and caption from [126].

Detector	Acceptance		Position	Technology	Main purpose
	Polar	Azimuthal			
SPD*	$\|\eta\| < 2.0$	full	r = 3.9 cm	Si pixel	tracking, vertex
	$\|\eta\| < 1.4$	full	r = 7.6 cm	Si pixel	tracking, vertex
SDD	$\|\eta\| < 0.9$	full	r = 15.0 cm	Si drift	tracking, PID
	$\|\eta\| < 0.9$	full	r = 23.9 cm	Si drift	tracking, PID
SSD	$\|\eta\| < 1.0$	full	r = 38.0 cm	Si strip	tracking, PID
	$\|\eta\| < 1.0$	full	r = 43.0 cm	Si strip	tracking, PID
TPC	$\|\eta\| < 0.9$	full	$85 < r/\text{cm} < 247$	Ne drift+MWPC	tracking, PID
TRD*	$\|\eta\| < 0.8$	full	$290 < r/\text{cm} < 368$	TR+Xe drift+MWPC	tracking, $e^{\pm}$ id
TOF*	$\|\eta\| < 0.9$	full	$370 < r/\text{cm} < 399$	MRPC	PID
PHOS*	$\|\eta\| < 0.12$	$220^o < \varphi < 320^o$	$460 < r/\text{cm} < 478$	$PbWO_4$	photons
EMCal*	$\|\eta\| < 0.7$	$80^o < \varphi < 187^o$	$430 < r/\text{cm} < 455$	Pb+scint.	photons and jets
DCal*	$0.15 < \|\eta\| < 0.7$	$260^o < \varphi < 327^o$	$430 < r/\text{cm} < 455$	Pb+scint.	photons and jets
HMPID	$\|\eta\| < 0.6$	$1^o < \varphi < 59^o$	r = 490 cm	C_6F_{14} RICH+MWPC	PID
ACORDE*	$\|\eta\| < 1.3$	$30^o < \varphi < 150^o$	r = 850 cm	scint.	cosmics
PMD	$2.3 < \eta < 3.9$	full	z = 367 cm	Pb+PC	photons
FMD	$3.6 < \eta < 5.0$	full	z = 320 cm	Si strip	charged particles
	$1.7 < \eta < 3.7$	full	z = 80 cm	Si strip	charged particles
	$-3.4 < \eta < -1.7$	full	z = -70 cm	Si strip	charged particles
V0*	$2.8 < \eta < 5.1$	full	z = 329 cm	scint.	charged particles
	$-3.7 < \eta < -1.7$	full	z = -88 cm	scint.	charged particles
T0*	$4.6 < \eta < 4.9$	full	z = 370 cm	quartz	time, vertex
	$-3.3 < \eta < -3.0$	full	z = -70 cm	quartz	time, vertex
ZDC*	$\|\eta\| > 8.8$	full	$z = \pm 113$ m	W+quartz	forward neutrons
	$6.5 < \|\eta\| < 7.5$	$\|\varphi\| < 10^o$	$z = \pm 113$ m	brass+quartz	forward protons
	$4.8 < \|\eta\| < 5.7$	$\|2\varphi\| < 32^o$	z = 7.3 m	Pb+quartz	photons
MCH	$-4.0 < \eta < -2.5$	full	$-14.2 < z/\text{m} < -5.4$	MWPC	muon tracking
MTR*	$-4.0 < \eta < -2.5$	full	$-17.1 < z/\text{m} < -16.1$	RPC	muon trigger

Appendix C

Analysis Framework – Versions

In order to be able to reproduce the results presented in this thesis, the specific versions of the analysis framework is provided. The analysis was performed using the AliRoot [155] framework, which uses the ROOT [161] system as a foundation on which the framework and applications are built [155]. AliRoot is divided into the core part of the framework, AliRoot, and the physics analysis code, AliPhysics [162], which is continuously developed and updated by the analysers. The following versions of the analysis framework was used:

Table C.1: List of the versions of the analysis framework used for the analysis presented in this thesis.

Framework	Version
ROOT	v5-34-30-alice5-2
AliRoot	v5-08-17-1
AliPhysics	vAN-20160930

Errata

Page xi	"4 < $p_{\mathrm{T}}^{\mathrm{D}^0}$ < 16 GeV/c" – Corrected to "3 < $p_{\mathrm{T}}^{\mathrm{D}^0}$ < 16 GeV/c"
Page xi	"9 < $p_{\mathrm{T}}^{\mathrm{D}^0}$ < 16 GeV/c" – Corrected to "8 < $p_{\mathrm{T}}^{\mathrm{D}^0}$ < 16 GeV/c"
Page xi	"3 < $p_{\mathrm{T}}^{\mathrm{D}^0}$ < 16 GeV/c" – Corrected to "2 < $p_{\mathrm{T}}^{\mathrm{D}^0}$ < 16 GeV/c"
Page 6	"$\Delta r \Delta p \geq 2\hbar$" – Corrected to $\Delta r \Delta p \geq \frac{\hbar}{2}$
Page 11	"for $p_{\mathrm{T}} \lesssim$ 3-4 GeV indicates" – Corrected to "for $p_{\mathrm{T}} \lesssim$ 3-4 GeV/c indicates"
Page 11	"centralities of ∼100 %" – Corrected to "centralities of ∼0%"
Page 13	"a result, the the differential" – Corrected to "a result, the differential"
Page 14	"central Pb–Pbcollisions" – Corrected to "central Pb–Pb collisions"
Page 16	"measured at LHC RHIC and is" – Corrected to "measured at LHC and RHIC is"
Page 19	"azimuthal angle, φ and" – Corrected to "azimuthal angle, φ, and"
Page 22	"Figures modified caption" – Corrected to "Figures and modified caption"
Page 25	"disappears at when" – Corrected to "disappears when"
Page 26	"transversing" – Corrected to "traversing"
Page 29	"$\mathrm{D}^{*+} \rightarrow \mathrm{D}^0\pi^+ \rightarrow \mathrm{K}^-\pi^+$" – Corrected to "$\mathrm{D}^{*+} \rightarrow \mathrm{D}^0\pi^+ \rightarrow \mathrm{K}^-\pi^+\pi^+$"
Page 33	"pion R_{AA} at < p_{T} < 20 GeV/c" – Corrected to "pion R_{AA} at p_{T} < 20 GeV/c"
Page 41	"$p_{\mathrm{T}}(\mathrm{c\bar{c}})$ (left) and $\Delta\varphi(\mathrm{c\bar{c}})$" – Corrected to "$p_{\mathrm{T}}$ (left) and $\Delta\varphi$"
Page 42	"in detail in Section 5" – Corrected to "in detail in Chapter 5"
Page 45	Figure aligned to top of page
Page 60	"signals and others detectors" – Corrected to "signals and other detectors"
Page 61	"multiplicity information information" – Corrected to "multiplicity information"
Page 63	"in the momentum, to the momentum" – Corrected to "to the momentum"
Page 70	Figure 4.3: Z-axis label added: "Efficiency"
Page 82	" ±3 nσ and -1 < nσ < 3" – Corrected to " ±3 $n_{\sigma}^{\mathrm{TPC}}$ and -1 < $n_{\sigma}^{\mathrm{TPC}}$ < 3"
Page 84	"simulation. [126]" – Corrected to "simulation. Figure and caption from [126]."
Page 89	Changed order of point 2 and 3 in list, according to subsection order
Page 91	"trigger and particle candidates" – Corrected to "trigger and associated particle candidates"
Page 95	"[1,8], [2,7], [3,6], [4,5]" – Corrected to [4,5], [3,6], [2,7], [1,8]"
Page 97	"Zvtx" – Corrected to "Zvertex" (2 occurrences)
Page 97	"$p_{\mathrm{T,\,D^0}}$" – Corrected to "$p_{\mathrm{T}}^{\mathrm{D}^0}$" (2 occurrences)
Page 99	"is" – Corrected to "was" (3 occurrences)"
Page 109	"an interval og" – Corrected to "an interval of"
Page 115	"a full achieved" – Corrected to "a full coverage was achieved"
Page 116	"D0 selection" – Corrected to "D^0 Selection"
Page 117	"TRD, TOF, TRD" – "TPC, TOF, TRD"
Page 121	"statistics estimate show" – Corrected to "statistics estimate shows"
Page 135	"[FIXME][show url]" – Corrected to "https://cds.cern.ch/record/842700"